Technische Universität München
TUM School of Computation, Information and Technology

Low-collisionality extension of fluid models for plasma edge simulations

Christoph Pitzal

Vollständiger Abdruck der von der TUM School of Computation, Information and Technology der Technischen Universität München zur Erlangung eines

Doktors der Naturwissenschaften

(Dr. rer. nat.)

genehmigten Dissertation.

Vorsitz: Prof. Dr. Eric Sonnendrücker

Prüfende der Dissertation:

1. Hon.-Prof. Dr. Frank Jenko
2. Prof. Dr. Ulrich Stroth
3. Prof. Dr. Hans-Joachim Bungartz

Die Dissertation wurde am 17.06.2024 bei der Technischen Universität München eingereicht und durch die TUM School of Computation, Information and Technology am 16.10.2024 angenommen.

Abstract

The performance of present-day fusion experiments and future fusion reactors is nearly always limited by turbulence. Predicting turbulence in the edge region of fusion experiments with the help of numerical simulations is especially challenging due to e.g. complex geometries, steep temperature and density gradients and neutral gas physics. Plasma fluid codes, like GRILLIX, are currently the workhorse for edge turbulence simulations. For fusion devices and scenarios, that come closer to reactor-relevant conditions low values of collisionality can be present even in the edge region. This raises challenges for plasma fluid models since they are derived for high collisionality and lose their validity if the collisionality becomes too low.

Within this thesis, the commonly used Braginskii closure for parallel heat fluxes is replaced by the Landau fluid closure, which can be understood as a low collisionality extension of the Braginskii closure. With this extension, the region of validity of the whole fluid model is expanded toward low collisionality, as the closure for the parallel heat fluxes is the most fragile part of the model in terms of collisionality.

The fluid closures are derived and a theoretical background is provided. The different closures are implemented into a one-dimensional toy model and their behaviour is demonstrated and examined in this simple geometry. Here we observe non-local heat fluxes predicted by the Landau fluid closure. The implementation into the edge turbulence fluid code GRILLIX, built on the flux-coordinate independent approach, is explained in detail as well as the verification of the implementation. Turbulence simulations in the geometry of the ASDEX Upgrade tokamak are presented, performed in L-mode conditions. Herein the Landau fluid closure is investigated in detail and compared to the Braginskii closure with flux limiters applied to it. Non-local heat fluxes are examined within the turbulence simulations for the Landau fluid closure and a global temperature asymmetry is observed for the case with the Braginskii closure and strong flux limiters.

Finally, attempts for simulations in the improved confinement mode (I-mode) regime are presented. The I-mode is a reactor-relevant operational regime, characterised by low collisionality in the edge region. Therefore this regime is rather challenging for fluid models and at the same time an excellent test case for the low collisionality extension due to the Landau-fluid closure. Although no stationary I-mode could be simulated, features of experimental I-modes were reproduced including pedestal relaxation events. A major finding is the identification of the underlying microinstability of pedestal relaxation events to be a micro-tearing mode.

Overall we demonstrate the importance of the employed fluid closure for performing predictive edge turbulence simulations of reactor-relevant operational regimes.

Kurzfassung

Die Leistungsfähigkeit heutiger Fusionsexperimente und zukünftiger Fusionsreaktoren wird fast immer durch Turbulenz begrenzt. Die Vorhersage von Turbulenzen im Randbereich von Fusionsexperimenten mit Hilfe numerischer Simulationen ist eine besondere Herausforderung, z.B. aufgrund komplexer Geometrien, steiler Temperatur- und Dichtegradienten und der Neutralgasphysik. Plasma-Fluid-Codes, wie GRILLIX, sind derzeit das "Arbeitspferd" für Randturbulenzsimulationen. Für Fusionsanlagen und -szenarien, die näher an reaktorrelevante Bedingungen heranreichen, können niedrige Kollisionalitätswerte bereits im Randbereich auftreten. Dies stellt eine Herausforderung für Plasma-Fluid-Modelle dar, da sie für hohe Kollisionalität hergeleitet werden und ihre Gültigkeit verlieren, sobald die Kollisionalität zu niedrig wird.

In dieser Arbeit wird der üblicherweise verwendete Braginskii-Schluss für parallele Wärmeströme durch den Landau-Fluid-Schluss ersetzt, der als eine Erweiterung für den Braginskii-Schluss in Richtung geringer Kollisionalität verstanden werden kann. Mit dieser Erweiterung wird der Gültigkeitsbereich des gesamten Fluidmodells in Richtung niedriger Kollisionalität ausgedehnt, da der Fluid-Schluss für parallele Wärmeströme der anfälligste Teil des Modells in Bezug auf Kollisionalität ist.

Die Fluid-Schlüsse werden hergeleitet und der theoretische Hintergrund wird erläutert. Die verschiedenen Schlüsse werden in ein eindimensionales Spielzeugmodell implementiert und ihr Verhalten wird in dieser einfachen Geometrie demonstriert und untersucht. Hier beobachten wir nichtlokale Wärmeströme, die durch den Landau-Fluid-Schluss vorhergesagt werden. Die Implementierung in den Randturbulenz-Fluidcode GRILLIX, der auf dem "flux-coordinate independent approach" aufbaut, wird im Detail erläutert, ebenso die Verifizierung der Implementierung. Es werden Turbulenzsimulationen in der Geometrie des ASDEX Upgrade Tokamaks vorgestellt, die unter L-Mode-Bedingungen durchgeführt werden. Dabei wird der Landau-Fluid-Schluss im Detail untersucht und mit dem Braginskii-Schluss verglichen, auf den "flux-limiter" angewendet werden. Nichtlokale Wärmeströme werden in den Turbulenzsimulationen mit dem Landau-Fluid-Schluss untersucht und es wird eine globale Temperaturasymmetrie für den Fall des Braginskii-Schlusses und starker "flux-limiter" beobachtet.

Schließlich werden Versuche für Simulationen im I-Mode-Regime vorgestellt. Die I-Mode ist ein reaktorrelevanter Betriebszustand, der sich durch geringe Kollisionen im Randbereich auszeichnet. Daher ist dieses Regime eine Herausforderung für Fluidmodelle und gleichzeitig ein hervorragender Testfall für die Erweiterung für geringe Kollisionalität durch den Landau-Fluid-Schluss. Obwohl keine stationäre I-Mode simuliert werden konnte, werden Merkmale experimenteller I-Moden reproduziert, einschließlich der "pedestal-relaxation events". Ein wichtiges Ergebnis ist die Identifizierung der zugrundeliegenden Mikroinstabilität von "pedestal-relaxation events" als "micro-tearing modes".

Insgesamt legen wir dar, wie groß die Bedeutung des verwendeten Fluid-Schlusses für die Durchführung von vorhersagekräftigen Randturbulenzsimulationen in reaktorrelevanten Betriebsszenarien ist.

Table of Contents

1 Introduction

1.1 The idea of fusion

Salimmo sù, el primo e io secondo,
tanto ch'i' vidi de le cose belle
che porta 'l ciel, per un pertugio tondo.
E quindi uscimmo a riveder le stelle.

We mounted up, he first and I the second,
Till I beheld through a round aperture
Some of the beauteous things that Heaven doth bear;
Thence we came forth to rebehold the stars.

Dante Alighieri
Divina Commedia - Inferno
Canto 34

1.1.1 Real stars

Stars have mesmerised humans for aeons. Therefore, it is no surprise that astronomy is one of the oldest disciplines in science, which shows e.g. the famous Nebra sky disc, dated back to ca. 1600 BC [1]. Despite the long history of astronomy, the question of why stars glow and how they produce such tremendous amounts of energy came up fairly late. A real discussion started mid of the 19th century.

Johannes Kepler postulated his three laws of planetary motion between 1609 and 1619 and since Henry Cavendish measured the gravitational constant in 1798, people have been able to calculate the mass of the sun. Today we know the mass of the sun to be about $1.998 \times 10^{30}\,\mathrm{kg}$, which is ca. 99.8 % of the mass of the whole solar system. The power released by the sun can be estimated using the solar constant, which states that the sun deposits approximately $1.3\,\mathrm{kW/m^2}$ [2] at a distance of one astronomical unit. With this value, we can deduce the total power of the sun over a complete sphere with a radius of one astronomical unit to be ca. $3.7 \times 10^{26}\,\mathrm{W}$.

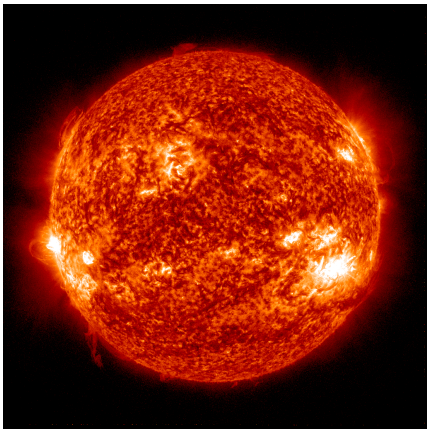

Figure 1: The sun on the day I handed in my thesis, 7th of June 2024, taken from [3]

Let us assume for a moment the sun would consist completely out of coal with a typical energy density of 2.4×10^6 J/kg. In a small back-of-the-envelope calculation, we can estimate that ca. 1.54×10^{20} kg of coal must be burned per second to generate the required output power. The entire mass of the sun would be consumed in ca. 410 years to sustain this reaction. This sun out of coal was never a serious theory to explain, how the sun generates its energy, unlike the following one. The theory of *gravitational contraction* was proposed by Hermann von Helmholtz (1821-1894) and Lord Kelvin (1824-1907). It stated that the sun is slowly contracting due to its own gravity, increasing the pressure and therefore generating heat in the core while contracting. With this theory, the lifetime of the sun was estimated to be 20 to 50 million years, which was still far too short to explain the timescales proposed by derivations of Darwin's theory of evolution by that time.

The first scientist who proposed nuclear fusion as a possible energy source for stars was Jean Perrin in 1919, accounting for a lifetime of billions of years for our sun. The first in-depth analysis was done by Hans Bethe in 1939 [4], explaining in detail the proton-proton chain, which is the dominant reaction in our sun.

The reason why energy is released during fusion reactions becomes clear when investigating the reactants and products, which are hydrogen and helium in the sun. One helium atom is slightly lighter than 4 hydrogen atoms by about 0.7%. This difference in mass is released during a fusion reaction in the form of electromagnetic radiation and thermal energy of the products. 0.7% does not sound much, to set this into context, we show the binding energy per nucleon over the mass number in fig. 2. The difference in binding energy between hydrogen isotopes (deuterium and tritium) and helium states how much energy is released in a fusion reaction. For fission reactions, the maximum available energy is indicated by the difference between uranium and iron, the element with the highest binding energy per nucleon. This comparison between fusion and fission reactions shows the vast potential that lies in fusion energy.

Due to fusion processes, the sun is losing ca. 4×10^9 kg of mass per second (roughly the weight of the great pyramid of Giza). Comparing this to the 1.54×10^{20} kg of coal needed per second for producing the same power, shows even more impressively the difference between energy released in chemical reactions and energy released in nuclear processes.

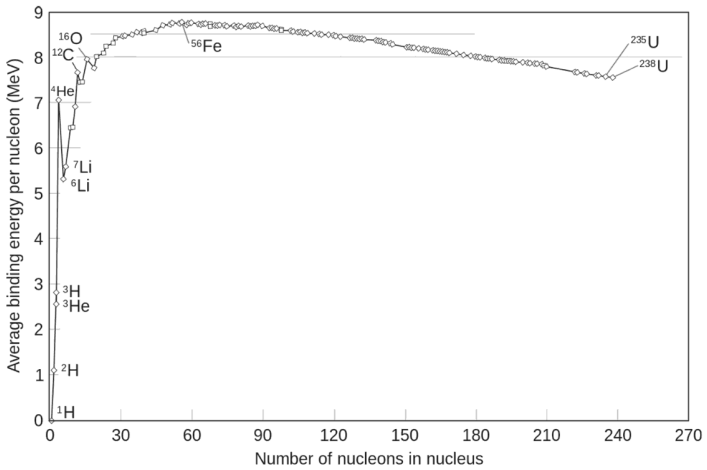

Figure 2: Binding energy per nucleon taken from [5]

1.1.2 Terrestrial stars - fusion on earth

Rafael Grossi, Director General of the International Atomic Energy Agency (IAEA), opened the 29th Fusion Energy Conference 2023 with the words

> *People may say that fusion will always be the energy of the distant future, but new scientific milestones suggest otherwise. [...] Clean and abundant energy means that the generations to come could have true sustainable prosperity.*

Exactly this is the mission of fusion researchers, making fusion energy accessible to humanity. But how should one be able to recreate the conditions present in the core of the sun? Luckily this is not necessary, since the reaction that is running there, the proton-proton chain, is not attractive to use in a power plant anyway. This reaction is running quite slowly, which has the positive effect of granting the sun a lifetime of several billion years but is not so handy for producing energy in a compact power plant. Therefore, different isotopes of hydrogen are used for terrestrial fusion, namely deuterium (^{2}H) and tritium (^{3}H). Their reaction reads

$$^2\mathrm{H} + {}^3\mathrm{H} \longrightarrow {}^4\mathrm{He}\,(3.5\,\mathrm{MeV}) + n\,(14.1\,\mathrm{MeV}). \tag{1}$$

The reason why deuterium and tritium are the most attractive candidates is seen in the fusion reaction rates $\langle \sigma v \rangle$ for different fuel components as plotted in fig. 3. For the temperatures fusion devices aim for, which are between $100 - 150 \times 10^6\,\mathrm{K}$, the fusion reaction rate of deuterium and tritium is more than two orders of magnitude higher than the next highest, which is deuterium and deuterium.

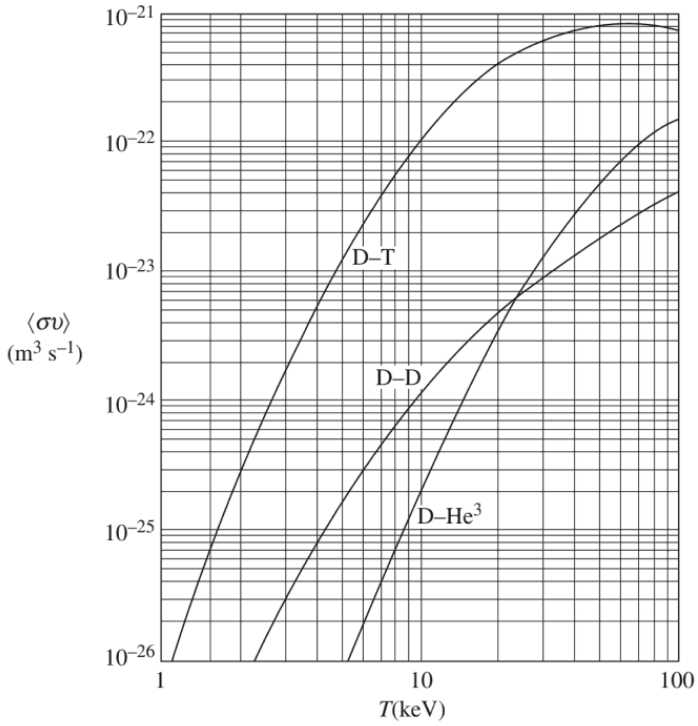

Figure 3: Fusion reaction rates $\langle \sigma v \rangle$ for different fuels, taken from [6]

How do we have to imagine the state of matter when it reaches temperatures like 100×10^6 K? Matter when heated up to such temperatures (and also for much smaller temperatures) forms an ionised gas, which is made up mainly of negatively charged electrons and positively charged ions. If a few formal definitions are fulfilled, this state of matter is called plasma. In the following we list three criteria that define plasma, following [7, 8]. For the definition of a plasma, we need to define a quantity which is essential in plasma physics, the Debye length

$$\lambda_D = \left(\frac{\varepsilon_0 T}{n_e e^2} \right)^{1/2}, \tag{2}$$

with ε_0 the vacuum permittivity, T the temperature of the plasma in eV, n_e the density of electrons and e the elementary charge. The Debye length defines the distance over which the influence of an individual charge is felt by other particles of the plasma. Or alternatively, if any charged object is inserted into a plasma, the Debye length defines the length scale over which plasma particles arrange themselves to shield the additional charge. The first criterion is that all relevant length scales L are much greater than the Debye length

$$L \gg \lambda_D. \tag{3}$$

From this criterion, we can conclude that there are no macroscopic charge separations present on distances larger than the Debye length, which implies macroscopic neutrality within a plasma, i.e.

$$n_e \approx \sum_i Z_i n_i. \tag{4}$$

Since the shielding process is a collective process of many particles, the second criterion is that the number of particles inside a sphere with the radius of a Debye length, a so-called Debye sphere is large

$$n_e \lambda_D^3 \gg 1. \tag{5}$$

The first criterion defines length scales on which the plasma can preserve charge neutrality. Analogously the third criterion defines timescales which ensure charge neutrality within a plasma. The plasma frequency

$$\omega_{\mathrm{pe}} = \sqrt{\frac{n_e e^2}{m_e \varepsilon_0}} \tag{6}$$

defines the frequency of electrons oscillating against a stationary ion background of equivalent charge. These oscillations define a natural time scale of the plasma. The third criterion states that all frequencies of interest ω have to be much smaller than the plasma frequency

$$\omega \ll \omega_{\mathrm{pe}}. \tag{7}$$

A more elegant definition of plasma is given in [9]: *A gas of charged particles is a plasma when the number of particles involved in any interaction of interest is large*

enough that they act collectively, rather than simply as individuals. This definition sums up the three stated criteria and provides a more intuitive picture.

Since a plasma consists of charged particles, it can be manipulated via electric and magnetic fields. Therefore, it is possible to build a magnetic cage to confine and prevent the hot plasma from touching the wall, which would cool it down immediately. This is the fundamental idea of magnetic confinement fusion. The two most promising concepts for magnetic confinement fusion are the tokamak and the stellarator shown in fig. 4.

For the confinement of both toroidal fusion devices it is necessary to provide helical magnetic field lines [6] (twisting the field lines as the go around the torus). There are many differences between tokamaks and stellarators, but the most fundamental one is how the helical magnetic field is generated. In a tokamak, the toroidal magnetic field (around the long direction of the torus) is produced by magnetic field coils located around the plasma, while the poloidal magnetic field (around the short direction of the torus) is generated by a toroidal current, which flows in the plasma and is induced via the so-called central solenoid, a large magnet placed in the centre of the torus. In a stellarator on the other hand both components of the magnetic field, the toroidal and poloidal one, are created via external coils, which have therefore a (slightly) more complicated shape.

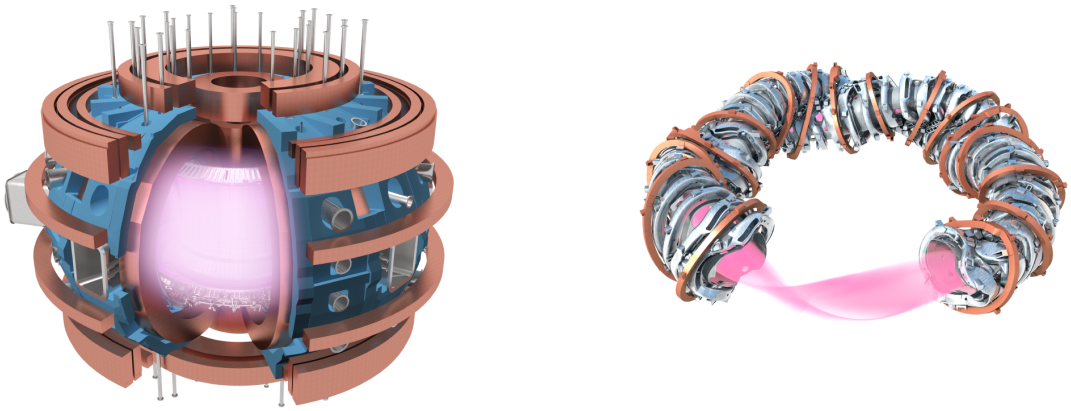

(a) The tokamak concept @IPP (b) The stellarator concept @IPP

Figure 4: The two main concepts for magnetic confinement fusion

1.1.3 Reaching ignition

A valuable figure of merit for any fusion experiment is the so-called triple product $nT\tau_E$ of the density n, temperature T and energy confinement time τ_E. The energy confinement time can be defined via $\tau_E = W/P_{\text{loss}}$, with the loss power P_{loss}. $W = 3nT$ is the stored energy, with $nT/2$ for each degree of freedom, times 2 for an equal number of electrons and ions, which is true for singly charged deuterium and tritium ions. The heating provided by deuterium-tritium fusion reactions reads $P_\alpha = fE_\alpha$ with $E_\alpha = 3.5\,\text{MeV}$ the energy of a α-particle (helium nucleus) and $f = n_D n_T \langle\sigma v\rangle = n^2 \langle\sigma v\rangle /4$ the rate of fusion reactions with deuterium and tritium mixed to equal parts $n = n_D/2 = n_T/2$. We can now define the Lawson criterion [10], which states

$$\begin{aligned} P_\alpha &\geq P_{\text{loss}} \\ \frac{1}{4} n^2 \langle \sigma v \rangle E_\alpha &\geq \frac{3nT}{\tau_E} \\ nT\tau_E &\geq \frac{12}{E_\alpha} \frac{T^2}{\langle \sigma v \rangle}. \end{aligned} \tag{8}$$

The function $T^2/\langle \sigma v \rangle$ has a minimum at $T \approx 14\,\text{keV}$, which means that the ideal temperature to gain as much fusion power as possible is not where the fusion reaction rate $\langle \sigma v \rangle$ peaks in fig. 3, but luckily lower temperatures of $T \approx 14\,\text{keV} \approx 160 \times 10^6\text{K}$. The Lawson criterion states the point of ignition, i.e. the point where the plasma can sustain its temperature solely through fusion reactions, without external heating. This is not necessary and due to limited plasma control, since the heating power would be lost as a control parameter, not desirable for a fusion power plant. The minimum requirement for a future fusion reactor is to produce more power via fusion reactions $P_{\text{fus}} = f E_{\text{fus}}$ with $E_{\text{fus}} = 17.6\,\text{MeV}$ the total energy released by a fusion process than is required for heating the plasma P_{heat}, so

$$Q = P_{\text{fus}}/P_{\text{heat}} > 1, \tag{9}$$

i.e. the point of break-even. So far, no magnetic confinement fusion device has reached this magic number. However, since the heating systems have an efficiency of less than 100 % and additional power is required for cooling systems and providing the magnetic field, a value of Q significantly greater than 1 would be needed to generate more power than is used for the operation of the device. This is precisely why ITER, the International Thermonuclear Experimental Reactor, aims for $Q > 10$ [11].

A lot of momentum was gained in the fusion landscape over the past few years, as Rafael Grossi stated at the 2023 Fusion Energy Conference. In comparison to the decades before when fusion devices were nearly exclusively built in national or international projects, more and more start-ups and companies joined this endeavour, of which some have physically reasonable concepts. Companies like Commonwealth Fusion Systems (CFS) [12], TAE Technologies [13] or Type One Energy [14] have interesting concepts and solid physical basis, although they still take high risks. The entry of the private sector shows most clearly that fusion research has made a lot of progress and the first fusion power plant comes within reach. Or to come back to the opening quote from Dante, the first artificial terrestrial stars are already glimmering on the horizon.

1.2 The challenges of fusion

Since the first tokamaks were built in the 1950s, a lot of progress has been made in reaching higher and higher values in $nT\tau_E$ as illustrated in fig. 5. The Joint European Torus (JET) in Culham in the United Kingdom has reached the highest values so far. Since JET had its first records in fusion power in 1997 no new dots were added to the chart that are closer to the region marked with *power plant*. What slowed down the progress, that is visible in this chart?

The optimum value in temperature is already fixed to 14 keV as we saw in the last section and is also visible in fig. 5. The density is limited indirectly by the Troyon

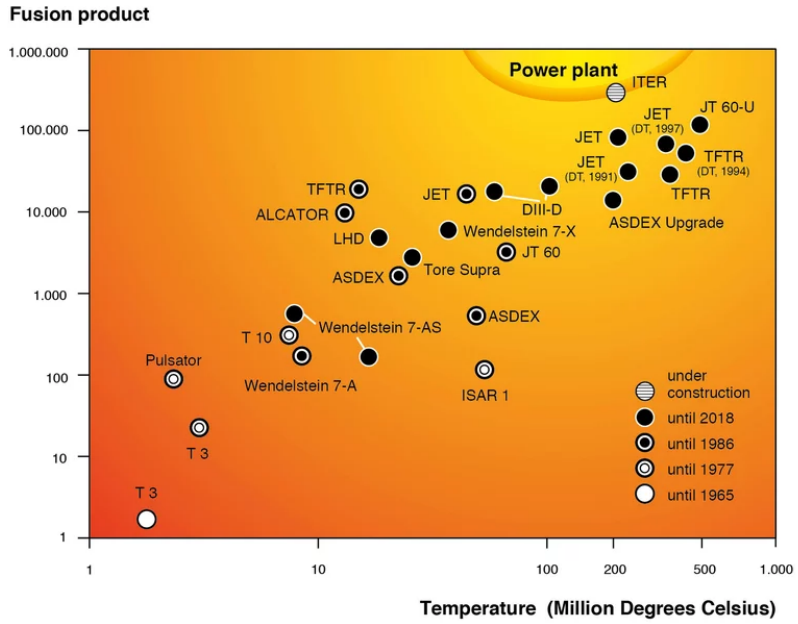

Figure 5: Triple product over core temperature for different experiments @IPP

beta-limit [15], which is a limit for the plasma pressure, and directly by the Greenwald density-limit [16]. Despite both limits taking higher values with increasing toroidal and poloidal magnetic fields, they remain limits also for machines like ITER with 5.3 T on axis [17] or the SPARC tokamak of CFS with high-temperature superconductors used for the toroidal field coils [18] achieving 12.2 T on axis [19]. The only parameter left to increase the value of the triple product is the energy confinement time τ_E. The idea for ITER is to raise τ_E by increasing the volume of the plasma and therefore the stored energy. One could also think intuitively of the plasma travelling a longer radial path since the minor radius is larger, therefore increasing the time it remains in the confined region. But let us take one step back and ask what is physically limiting the values of τ_E in magnetic confinement fusion experiments.

1.2.1 Turbulence in fusion experiments

In magnetic fusion devices, there are different kinds of radial transport present, which are the underlying physical mechanisms, that set the confinement time τ_E. For most tokamaks and optimised stellarators, the dominant radial transport mechanism is anomalous transport, or in other words turbulence. To get an intuition of how to think of turbulence in a fusion device, we can examine fig. 6, which shows a snapshot of the ion temperature from a plasma edge turbulence simulation, performed with the code GRILLIX [20].

The turbulent structures that are visible in fig. 6 transport hot plasma from the inner parts outwards, therefore they decrease the confinement time. Before we go on, we take a moment and use fig. 6 to define some terminology. The white dashed line is the separatrix because it separates the inner closed-field-line region from the outer open-field-line region. Of course, the magnetic field lines are not really open, since this would require magnetic monopoles, but they intersect the wall and leave the domain of the fusion device. The

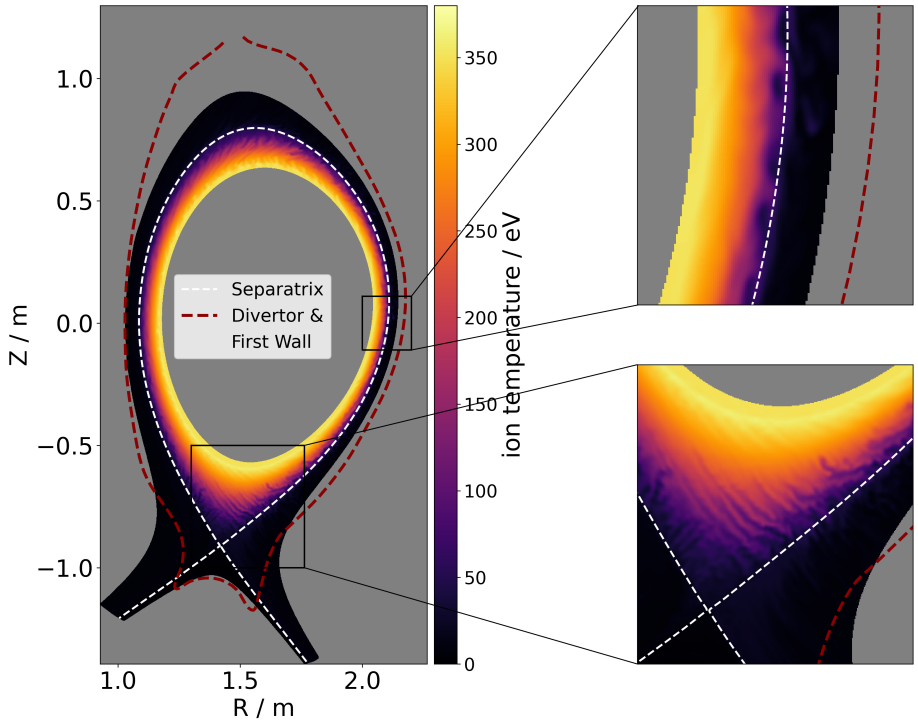

Figure 6: Turbulent structures in a GRILLIX simulation

point where the separatrix intersects itself is called X-point for obvious reasons. The region outside the separatrix is called the scrape-off-layer (SOL), as plasma is transported very fast along the field lines towards the divertor. The divertor is a special section of the first wall of the device where plasma hits the wall directly after it is diverted by the magnetic geometry. This divertor geometry is necessary to manage particle and heat exhaust while achieving good core confinement [21]. In fig. 6 this corresponds to the region, where the red line intersects the simulation domain. The divertor has to withstand high heat loads of up to $10\,\mathrm{MW/m^2}$ for ITER [22] and is therefore built from robust tungsten monoblocks for this device. As there is no strict definition of the *plasma edge* we consider the complete simulation domain, shown in fig. 6 as plasma edge within this thesis. In contrast to the plasma edge, the core region is omitted in this simulation.

1.2.2 Turbulence in the plasma edge

Turbulence in the plasma edge has gained more and more importance over the last years. Improved confinement regimes like the High-confinement-mode [23] (H-mode), the Improved-mode (I-mode) [24], the Quasi-Continuous-Exhaust regime (QCE) [25] or the X-Point Radiator (XPR) [26], have in common, that the most relevant physics, is happening near the separatrix. After the discovery of the H-mode, the standard operational regime was called Low-confinement-mode (L-mode) for clear separation. The mechanism that leads to the H-mode [27] is most interesting. The plasma forms a self-organised

internal transport barrier near the separatrix. In the region where this transport barrier is active, turbulent structures are torn apart and turbulent transport is therefore strongly reduced. Transport barriers are strongly linked to zonal flows and the $E \times B$ shear due to the radial electric field. Zonal flows themselves are driven by turbulence via the Reynolds stress. Details of this intricate interplay are discussed until today [28]. For modelling such phenomena accurately, the radial electric field is a quantity of major interest. The contrast of pressure profiles in L-mode and H-mode is shown in fig. 7.

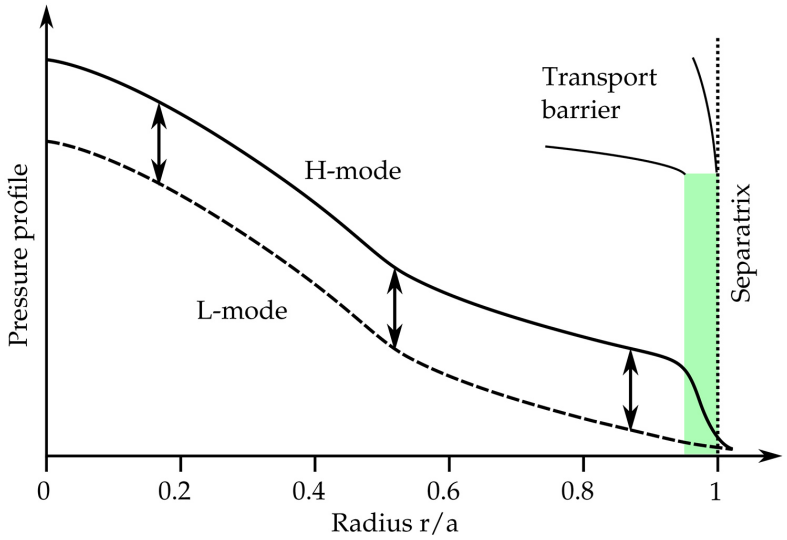

Figure 7: Pressure profile for L-mode and H-mode @IPP

Because the transport barrier is close to the separatrix, the whole profile towards the centre is raised, as if placed on top of a pedestal. The region where the transport barrier is active is therefore also called pedestal. With this pedestal the stored energy of the plasma W increases significantly in contrast to P_{loss}, therefore $\tau_E = W/P_{\text{loss}}$ is increased.

The occurrence of Edge Localised Modes (ELMs)[29] in H-mode makes the utilisation of this regime in a future power plant problematic. ELMs expel a significant fraction of the plasma stored energy periodically in short pulses. Such periodic bursts exceed the maximum heat loads that can be handled by the divertor dramatically. For using the improved performance of the H-mode, while keeping the conditions for plasma-facing components bearable, so-called ELM-free regimes are developed and investigated, which include I-mode, QCE and the XPR. To understand these regimes in greater detail, simulations of the edge region are necessary.

Here we encounter a problem, since turbulence simulations of the edge region are rather challenging due to multiple reasons, which include high fluctuation amplitudes, steep gradients, physics of neutral particles which become important, challenging geometries with one or several X-points and open magnetic field lines. Due to this challenging environment, there are not many codes that can perform simulations in this region and even fewer, which can do predictions for machines like ITER. At the same time, conclusions that can be drawn from such simulations can have a significant impact on the whole fusion community. One recent example of such a case is a debate about the scrape-off-layer fall-off-length λ_q. This important quantity defines the width on which heat loads arriving on the divertor are spread, so the larger λ_q the larger the wetted area and there-

fore the lower the peak heat loads. An experimental multi-machine scaling was published already in 2013 [30], which revealed that λ_q only depends on the poloidal magnetic field B_{pol}. So there are no further control parameters to increase λ_q. An extrapolation of this multi-machine scaling for ITER resulted in $\lambda_q \approx 1\,\text{mm}$. In contrast to this result, the gyrokinetic particle-in-cell (PIC) code XGC1 predicted with a value of $\lambda_q \approx 6\,\text{mm}$ [31], while matching the experimentally measured values for multiple machines included in the scaling in [30]. If λ_q will be 1 or 6 mm has tremendous implications for the performance of ITER and future experiments. Although this paper [31] was already published in 2017, until now this unexpected result was neither confirmed nor contradicted by a second code.

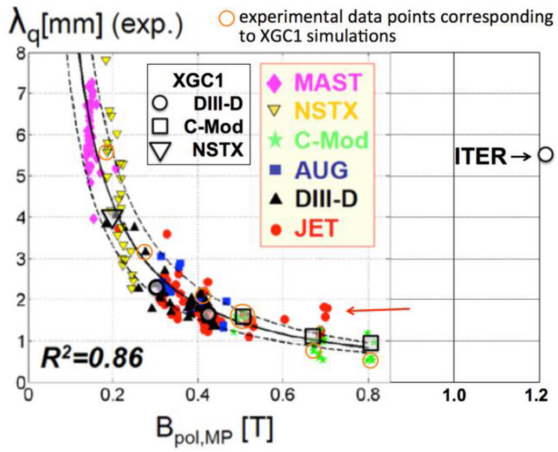

Figure 8: SOL fall of length experimentally measured for different machines and simulated values by the XGC1 code, figure taken from [31]

Developing simulation tools that are able to make predictions for such regimes is a task of major importance and has the potential to lead towards a big step in the direction of the first fusion power plants. The thesis you are currently reading aims to contribute to this task.

1.3 The contribution of this thesis

As we have seen in the last section, gyrokinetic turbulence simulations of the plasma edge are already feasible [31]. However, fluid models are still the workhorse of plasma edge simulations. Codes such as BOUT++ [32], GDB [33], GBS [34], SOLEDGE3X [35], FELTOR [36] or GRILLIX [37] are designed to solve fluid equations or gyro-fluid equations in the case of FELTOR in the edge and SOL of magnetic confinement fusion experiments. There are several arguments in favour of fluid models. Up to now, fluid models are significantly less computationally intensive than gyrokinetic models, which is already a selling point by itself. The more important implication is, however, that due to savings in compute time fluid models are able to scan parameters and investigate dependencies. Furthermore, fluid models are more easily accessible in comparison to kinetic models and it is easier to gain physical intuition, as one can deduce from the fluid equations e.g. how temperature and density influence each other and by what mechanisms. Gyrokinetic simulations on the other hand can be understood as numerical experiments due to the complexity of these five-dimensional models, which is suggested by the full name

of the gyrokinetic code GENE [38] (Gyrokinetic Electromagnetic Numerical Experiment). Nevertheless, gyrokinetic codes are a very powerful prediction tool and are currently considered the gold standard in plasma turbulence simulations, as they solve the model of highest fidelity accessible. A further argument in favour of fluid models is the simulation time span. While gyrokinetic edge simulations cover time spans of 100 μs [31] to 1 ms [39], it is desirable to perform simulations on the time scale of the energy confinement time of the simulation domain, which is for the edge region shorter than for the whole device but still of the order of tens of milliseconds. Several milliseconds are already regularly simulated in fluid simulations [40, 41].

Kinetic effects, like trapped particle or finite Larmor radius effects, are missing in conventional fluid models, although there are attempts to capture these effects with gyro-fluid models [36] or with the so-called arbitrary-moment approach [42]. However, fluid models are facing further challenges. The common Braginskii closure [43], which is used to close the set of fluid equations, is rigorously valid in the short-mean-free-path regime, i.e. in highly collisional plasmas. The edge region of a magnetic fusion device shows considerably lower temperatures than the core region and therefore also higher collisionalities. Nevertheless, conditions which violate the short-mean-free-path assumption of the Braginskii closure are already present in the edge of present-day experiments, where high-performance scenarios with high temperatures near the separatrix are investigated.

In order to apply fluid models to conditions, which will be present in the plasma edge of ITER, it is necessary to extend the employed fluid closure towards lower collisionality. In this thesis, the focus lies on the closure term for the parallel conductive heat flux $q_\parallel$. This term is most sensible to violations of the short-mean-free-path assumption, as it represents the highest fluid moment provided by the Braginskii closure. An elaborate approach for a fluid closure which is valid for lower collisionality is the so-called Landau-fluid closure [44]. The collisionless limit of the Landau-fluid closure is based on a closure proposed by Hammett and Perkins [45], which approximates the kinetic effect of linear Landau damping in fluid models.

This Landau-fluid closure is derived, discussed in detail and compared to the Braginskii closure as well as to the closure proposed by Hammett and Perkins. It is tested numerically in a simple one-dimensional geometry to study its behaviour and compare it to previous work [46], here we reproduce the non-local form of the heat fluxes for low collisional setups.

The closure is implemented into the edge plasma turbulence code GRILLIX [37], which employs the Flux-Coordinate-Independent (FCI) approach [47, 48]. Within the FCI approach, perpendicular dynamics are treated on dense unstructured grids, while for the much faster parallel dynamics, a sparse resolution is used. For parallel operators, the magnetic field lines are traced and interpolated once in between two poloidal planes. This information is stored in matrices, i.e. the application of a parallel operator corresponds to a matrix-vector multiplication. To calculate the heat fluxes predicted by the Landau-fluid closure, a set of decoupled elliptic equations has to be solved along magnetic field lines. In globally field-aligned approaches this problem remains one-dimensional along the parallel direction and can be solved efficiently, as e.g. shown with BOUT++[49]. In the framework of the FCI approach, this problem becomes a fully three-dimensional one due to interpolation between neighbouring planes and is therefore computationally more demanding.

Non-linear turbulence simulations employing the Landau-fluid closure in the setup of an L-mode discharge of the ASDEX Upgrade tokamak are presented and compared with simulations using the Braginskii closure. The pure Braginskii closure is corrected via heat-flux limiters, which are a relatively simple ad-hoc correction for low-collisionality. Three simulations are investigated in detail, one with the Landau-fluid closure and two employing the Braginskii closure with different values for the heat-flux limiters. All of the simulations incorporate recently implemented magnetic flutter effects [50] and neoclassical ion viscosity [51]. The density and electron temperature profiles do not deviate much between the three simulations as expected for an L-mode discharge with moderate collisionality, the ion temperature profile on the other hand deviates strongly for the Braginskii closure with strong heat-flux limiters due to an up-down asymmetry evolving in the ion temperature caused by the heat-flux limiter. Furthermore, we find for the radial electric field profile, that with the Landau-fluid closure, it is improved significantly towards values measured in the experiment. Also, the non-locality of heat fluxes predicted by the Landau-fluid closure is investigated for the non-linear turbulence simulations.

Lastly, a simulation of an I-mode discharge in ASDEX Upgrade is performed with the Landau-fluid closure. A key feature of the I-mode is high temperatures and low densities [52], therefore it shows very low collisionality in the edge region compared to other operational regimes. This makes an I-mode discharge the perfect candidate for testing the low-collisionality extension by the Landau-fluid closure. The simulations show intermittent behaviour, which can be linked to pedestal relaxation events [53]. For comparison, a simulation with the Braginskii closure and heat-flux limiters is performed but no such features were present and the observed profiles suggest a strongly heated L-mode. In those simulations, we see a strong difference between the two heat-flux closures.

In the last chapter, a step towards simulations of reactor-relevant scenarios was taken, which is the most important point of this thesis. We do not want to lose sight of the bigger picture, which is making fusion energy accessible to humans. Hopefully, with this thesis, the first terrestrial stars are already glimmering a little brighter.

2 Theoretical Background

This chapter has the purpose of introducing the necessary theoretical background and concepts, upon which the following chapters will be built.
The starting point in the description of plasma forms the Boltzmann equation and the concept of kinetic theory. Fluid moments are defined via velocity-space integrals over the distribution function and equations that describe their temporal evolution, namely the continuity, momentum and energy equation, are found by taking velocity-space integrals over the Boltzmann equation. We investigate why fluid models need closure approximations and how such a closure is constructed.
The focus of this work lies on the closure for the parallel conductive heat flux $q_\parallel$. Different closures including the Braginskii, Hammett-Perkins and Landau-fluid closure are presented. The Braginskii closure is motivated intuitively by random-walk estimations and the exact closure is derived for a Lorentz plasma, which is the approximation of ions with infinitely high charge number ($Z_i \to \infty$). An explanation of why the Braginskii closure for $q_\parallel$ breaks for low collisionality is given and extensions and more elaborate closures are investigated. The fluid closure by Hammett and Perkins for collisionless plasmas is introduced and derived, furthermore, it is explained how this fluid closure introduces the kinetic effect of linear Landau-damping into a fluid model. The argument involves the response function of the system, which describes, how the density responds to a driving electrostatic potential. The linear response function of a kinetic system is derived and compared to the response functions of fluid models, incorporating different closure approximations. We explain how the Hammett-Perkins closure is translated from a δf-model into a full-f model. The Landau-fluid closure is presented and it is demonstrated that it reproduces the Braginskii closure in the limit of high collisionality and the Hammett-Perkins closure in the limit of low collisionality. It is shown how this model translates into configuration space and the limitations of the model are highlighted.
Lastly, we discuss the drift reduction of fluid equations including the closure approximations, which are necessary to eliminate fast time scales and to employ the resulting equations in plasma fluid turbulence codes. The closure approximations stay essentially unchanged by this procedure.

2.1 Plasma fluid equations

The derivation in this section follows partly the derivation in [43, 7, 9]. Furthermore, we want to emphasise that all calculations contained in this thesis, employ the SI units system, with the small exception of temperatures being expressed as an energy in the unit of electron volts ($1\,\mathrm{eV} = 1.602 \times 10^{-19}\,\mathrm{J}$). So whenever T appears, it is implicitly assumed to be $k\tilde{T}$, with $[\tilde{T}] = \mathrm{K}$ and $k = (11605\,\mathrm{K/eV})^{-1}$.

2.1.1 The kinetic equation

The most rigorous approach to predict plasma turbulence would be to solve for each particle its equation of motion, or equivalently describe the system in a phase space with dimension six times the number of particles. For relevant systems this is not feasible as the number of particles is usually of the order of 10^{21} and all particles are coupled via electric and magnetic fields.

However, as we discussed in the introduction part, an elegant definition of a plasma is, that its particles act collectively, rather than simply as individuals [9]. So following each single particle is not necessary. With a large number of particles in a relatively small volume as a fusion device, a statistical approach is close at hand. We consider a distribution function $f_\alpha(\boldsymbol{x}, \boldsymbol{v}, t)$ which is defined as the probability density of particles of a species α per unit volume in a six-dimensional phase space, three dimensions in $\boldsymbol{x}$ and three dimensions in $\boldsymbol{v}$.

The Boltzmann equation describes the temporal evolution of this distribution function

$$\frac{\partial}{\partial t} f_\alpha + \boldsymbol{v} \cdot \nabla f_\alpha + \frac{q_\alpha}{m_\alpha} \left(\boldsymbol{E} + \boldsymbol{v} \times \boldsymbol{B}\right) \cdot \nabla_v f_\alpha = C_\alpha \left(f_\alpha\right), \tag{10}$$

with ∇ the spatial gradient and ∇_v the gradient in velocity space, q_α the charge and m_α the mass of particles, $\boldsymbol{E}$ the macroscopic electric and $\boldsymbol{B}$ macroscopic magnetic field. All microscopic dynamics are encapsulated in the right-hand side with the collision operator $C_\alpha \left(f_\alpha\right) = \left(\partial f_\alpha / \partial t\right)$. The collision operator consists of

$$C_\alpha \left(f_\alpha\right) = \sum_\beta C_{\alpha,\beta} \left(f_\alpha, f_\beta\right), \tag{11}$$

where $C_{\alpha,\beta}$ denotes changes of the distribution function of species α due to collisions with particles of species β per unit time. In the following we consider elastic collisions, in which the particles do not change their species, so inelastic collisions are neglected and we assume that e.g. fusion reactions or ionisation processes are modelled in a different way, not via collisions. Although we have not considered a special form of the collision operator yet, a few properties have to be fulfilled by any collision operator that models elastic collisions, i.e.

$$\begin{aligned} &\int C_{\alpha\beta}(f_{\alpha,\beta}) \, \mathrm{d}^3 v = 0, \\ &\int m_\alpha \boldsymbol{v} \, C_{\alpha\alpha}(f_{\alpha,\alpha}) \, \mathrm{d}^3 v = 0, \\ &\int \frac{m_\alpha}{2} v^2 \, C_{\alpha\alpha}(f_{\alpha,\alpha}) \, \mathrm{d}^3 v = 0, \end{aligned} \tag{12}$$

where the first equation states particle conservation due to collisions and the second and third one momentum and energy conservation for collisions within one species. This can be extended for collisions between different species, where the collision operator has to fulfil

$$\begin{aligned} &\int m_\alpha \boldsymbol{v} \, C_{\alpha\beta}(f_{\alpha,\beta}) \, \mathrm{d}^3 v + \int m_\beta \boldsymbol{v} \, C_{\beta\alpha}(f_{\beta,\alpha}) \, \mathrm{d}^3 v = 0, \\ &\int \frac{m_\alpha}{2} v^2 \, C_{\alpha\beta}(f_{\alpha,\beta}) \, \mathrm{d}^3 v + \frac{m_\beta}{2} v^2 \, C_{\beta\alpha}(f_{\beta,\alpha}) \, \mathrm{d}^3 v = 0, \end{aligned} \tag{13}$$

which states total momentum and energy conservation also due to collisions between species. Many different collision operators with different assumptions have been proposed over the years. Collision operators are a vast topic on their own. To mention a just few

important ones, there is the Bhatnagar–Gross–Krook operator [54] which is probably the simplest one and describes an exponential relaxation towards a thermal equilibrium. Furthermore, there is a Lorentz collision operator [55], which describes collisions of electrons with infinitely heavy ions and will be used later in this chapter. The Landau collision operator [43] is an accurate description of elastic collision between charged particles and is used for derivation of the Braginskii closure.

Although attempts to solve the Boltzmann equation (eq. (10)) and retain a full kinetic model are present [56], the method is computationally still far too expensive to perform simulations of a full scale fusion device. An established method to reduce the computational effort is the gyrokinetic theory [57], where the fast gyromotion of particles around magnetic field lines is averaged out and the phase space is therefore reduced to five dimensions. With gyrokinetics simulations on the scale of a full fusion device are already possible [58, 59], and they are considered currently as gold standard of turbulence simulations in fusion plasmas. Global gyrokinetic simulations are possible yet still quite expensive. Another way to reduce the computational effort even more is to change from a kinetic to a fluid description of a plasma. This way we eliminate the velocity space completely and arrive at a three-dimensional problem. This procedure is sketched in the following chapter.

2.1.2 Deriving fluid moments

Moments in the fluid description of a plasma are defined via velocity space integrals over the distribution function, we obtain the first four moments by

$$\begin{aligned}
n_\alpha(\boldsymbol{x},t) &= \int f_\alpha(\boldsymbol{x},\boldsymbol{v},t)\,\mathrm{d}^3v,\\
\boldsymbol{u}_\alpha(\boldsymbol{x},t) &= \frac{1}{n_\alpha(\boldsymbol{x},t)}\int \boldsymbol{v} f_\alpha(\boldsymbol{x},\boldsymbol{v},t)\,\mathrm{d}^3v,\\
T_\alpha(\boldsymbol{x},t) &= \frac{1}{n_\alpha(\boldsymbol{x},t)}\int \frac{m_\alpha}{3}\left(\boldsymbol{v}-\boldsymbol{u}(\boldsymbol{x},t)\right)^2 f_\alpha(\boldsymbol{x},\boldsymbol{v},t)\,\mathrm{d}^3v,\\
\boldsymbol{q}_\alpha(\boldsymbol{x},t) &= \int \frac{m_\alpha}{2}\left(\boldsymbol{v}-\boldsymbol{u}(\boldsymbol{x},t)\right)^2\left(\boldsymbol{v}-\boldsymbol{u}(\boldsymbol{x},t)\right) f_\alpha(\boldsymbol{x},\boldsymbol{v},t)\,\mathrm{d}^3v,
\end{aligned} \tag{14}$$

where the four moments represent the density $n(\boldsymbol{x},t)$, mean velocity $\boldsymbol{u}(\boldsymbol{x},t)$, temperature $T(\boldsymbol{x},t)$ and heat flux $\boldsymbol{q}(\boldsymbol{x},t)$ of the plasma. We can derive equations that describe the temporal evolution of these fluid moments by taking velocity space integrals over the Boltzmann equation eq. (10) times 1, $m_\alpha\boldsymbol{v}$ and $m_\alpha v^2/2$

$$\frac{\partial}{\partial t}n_\alpha + \nabla\cdot(n_\alpha\boldsymbol{u}_\alpha) = 0, \tag{15}$$

$$m_\alpha n_\alpha\left(\frac{\partial}{\partial t}\boldsymbol{u}_\alpha + \boldsymbol{u}_\alpha\cdot\nabla\boldsymbol{u}_\alpha\right) = -\nabla p_\alpha - \nabla\boldsymbol{\Pi}_\alpha + q_\alpha n_\alpha\left(\boldsymbol{E}+\boldsymbol{u}_\alpha\times\boldsymbol{B}\right) + \boldsymbol{R}_\alpha, \tag{16}$$

$$\frac{3}{2}n_\alpha\left(\frac{\partial}{\partial t}T_\alpha + \boldsymbol{u}_\alpha\cdot\nabla T_\alpha\right) = -p_\alpha\nabla\cdot\boldsymbol{u}_\alpha - \nabla\cdot\boldsymbol{q}_\alpha - \boldsymbol{\Pi}_\alpha\otimes\nabla\boldsymbol{u}_\alpha + Q_\alpha, \tag{17}$$

with the scalar pressure p_α, the stress tensor $\boldsymbol{\Pi}_\alpha$, the frictional momentum transfer $\boldsymbol{R}_\alpha$, the heat flux $\boldsymbol{q}_\alpha$ and the heat transfer term Q_α. The electric and magnetic field $\boldsymbol{E}$ and $\boldsymbol{B}$ are defined via the Maxwell equations

$$\nabla \cdot \boldsymbol{E} = \frac{\rho_{\mathrm{ch}}}{\varepsilon_0}, \tag{18}$$

$$\nabla \cdot \boldsymbol{B} = 0, \tag{19}$$

$$\nabla \times \boldsymbol{E} = -\frac{\partial}{\partial t}\boldsymbol{B}, \tag{20}$$

$$\nabla \times \boldsymbol{B} = \mu_0 \boldsymbol{J} + \mu_0 \varepsilon_0 \frac{\partial}{\partial t}\boldsymbol{E}, \tag{21}$$

which are coupled back to the plasma again via the charge density $\rho_{\mathrm{ch}} = \sum_\alpha q_\alpha n_\alpha$, the current $\boldsymbol{J} = \sum_\alpha q_\alpha n_\alpha \boldsymbol{u}_\alpha$. μ_0 is the vacuum permeability and ε_0 the vacuum permittivity. We could proceed like this and evolve an infinite set of fluid equations, wherein the full information of the initial kinetic system is still preserved. In the case of highly collisional plasmas, however, this is not necessary, since contributions of higher moments decrease very fast. The assumption of a highly collisional plasma states that thermodynamic equilibrium is reached faster than the relaxation of macroscopic gradients due to transport happens. With this assumption the method of Chapman and Enskog [60] is applicable with a few changes compared to the original work for neutral fluids. The first one who did this tedious calculation to derive closure approximations for a highly collisional plasma was Braginskii [43]. In this work, he keeps the three time-dependent moment equations as we wrote them down in eq. (15), eq. (16) and eq. (17) and derives closure terms for all higher order moments that still arise in these equations, which are $\boldsymbol{q}_\alpha$, $\boldsymbol{\Pi}_\alpha$, $\boldsymbol{R}_\alpha$ and Q_α. We will focus mainly on the closure for the heat flux $\boldsymbol{q}_\alpha$ since this is the starting point for the more elaborate heat flux closures that will be discussed in this thesis.

2.1.3 Quasineutrality

Quasineutrality is a key concept of plasma physics and simplifies eq. (15) to eq. (21). It states that in the non-relativistic limit

$$\omega \ll ck, \tag{22}$$

with ω the frequency of interest, $k = |\boldsymbol{k}|$ the magnitude of the wave vector and c the speed of light, and for frequencies lower than the plasma frequency and length scales L larger than the Debye length

$$\omega \ll \omega_{\mathrm{pe}} \qquad \text{and} \qquad L \gg \lambda_D \tag{23}$$

the charge separation is negligibly small. In the non-relativistic limit, we find the displacement current in eq. (21) to be small and it can be neglected. Therefore we find by taking the divergence of eq. (21) that

$$\nabla \cdot \boldsymbol{J} = 0, \tag{24}$$

the current is divergence-free. With this approximation, we also eliminate electromagnetic light waves in our model. As mentioned in the first chapter the plasma frequency ω_{pe} defines the frequency at which a cloud of electrons oscillates around a static background of equivalent positive charge. Therefore, for any frequency much lower than the ω_{pe}, there is no macroscopic charge separation present in the plasma. Regarding the spatial restriction, we can think of the Debye length as the length scale, where the thermal energy of the particles, which tends to disturb electric neutrality, becomes comparable to the electrostatic energy, which tends to restore electric neutrality. Therefore, if the length scale of interest becomes smaller than the Debye length, the assumption of quasineutrality is not valid. For time and length scales that satisfy eq. (23) the macroscopic charge separation is small, which implies

$$\rho_{ch} = e\left(Zn_i - n_e\right) \ll en_\alpha \quad \Rightarrow \quad n_e \approx Zn_i \quad \Rightarrow \quad \nabla\frac{\varepsilon_0}{en_\alpha}\cdot\boldsymbol{E} \ll 1 \neq 0, \tag{25}$$

with e the elementary charge. Therefore, one continuity equation for the density $n = n_e \approx Zn_i$, which represents electrons and ions simultaneously, is sufficient. This situation is called quasineutral since the plasma is neutral enough that the total current is divergence-free, but not enough that the electric field has to be divergence-free.

2.2 Fluid closures

2.2.1 Intuitive motivation of the Braginksii closure

In a small Gedankenexperiment, using random walks, we can estimate the dependency of the parallel conductive heat flux $q_\parallel$ on the other fluid moments We think of a one-dimensional case. Suppose we have a flat density distribution

$$n(x) = n = \text{const.}, \tag{26}$$

so there is no particle flux. During the typical collision time τ, which is small in our consideration, every particle makes one small random step with the step width Δx. The temperature distribution does not vary strongly on length scales of one step Δx, therefore we can linearize the temperature distribution

$$T(x) = T(x_0) + \left.\frac{\partial T}{\partial x}\right|_{x_0}(x - x_0). \tag{27}$$

Since we are in a one-dimensional case, half of the particles in the right domain from x_0 to $x_0 + \Delta x$ (see fig. 9) make a step to the left and end up in the left domain from $x_0 - \Delta x$ to x_0 and half of the particles make a step to the right. For the left domain, the situation is vice versa. We calculate now the two unidirectional heat fluxes q_+ and q_- that are crossing the plane at x_0

$$q_+ = \frac{1}{2}\int_{x_0-\Delta x}^{x_0}\frac{1}{\tau}nT(x)dx = \frac{n}{2\tau}\left[T(x_0)\Delta x - \frac{(\Delta x)^2}{2}\left.\frac{\partial T}{\partial x}\right|_{x_0}\right], \tag{28}$$

$$q_- = \frac{1}{2}\int_{x_0}^{x_0+\Delta x}\frac{1}{\tau}nT(x)dx = \frac{n}{2\tau}\left[T(x_0)\Delta x + \frac{(\Delta x)^2}{2}\left.\frac{\partial T}{\partial x}\right|_{x_0}\right]. \tag{29}$$

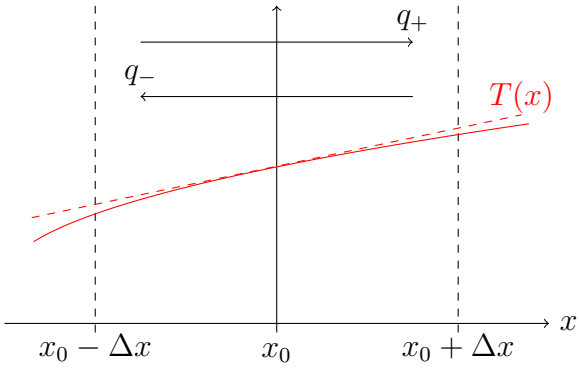

Figure 9: Temperature distribution along the dimension x with the exact (solid line) and the linearized temperature (dashed) $T(x)$. The two arrows indicate the unidirectional heat fluxes from the left domain ($x_0 - \Delta x$ to x_0) into the right domain (x_0 to $x_0 + \Delta x$) and vice versa, denoted as q_+ and as q_-.

The complete heat flux is obtained by taking the difference between q_+ and q_-. Therefore we obtain

$$q = q_+ - q_- = -n\frac{(\Delta x)^2}{2\tau}\left.\frac{\partial T}{\partial x}\right|_{x_0}. \tag{30}$$

Therefore we find that the heat conduction κ in our plasma, which is per definition the parameter, that connects the heat flux to a negative temperature gradient, has the form

$$\kappa = n\frac{(\Delta x)^2}{2\tau}. \tag{31}$$

With this form for the heat conductivity κ we can find the dependencies of the parallel and the perpendicular heat conductivity. For the parallel direction $(\Delta x)_\parallel \sim v_{\mathrm{th}}\tau$. So we find for the parallel heat conductivity

$$\kappa_\parallel \sim n\frac{(v_{\mathrm{th}}\tau)^2}{\tau} \sim \frac{nT\tau}{m}. \tag{32}$$

Similarly, we can find the corresponding step size for the perpendicular dynamics. Since particles in a strong magnetic field gyrate around the magnetic field lines, the step size of a perpendicular step is the gyro radius of the corresponding species $(\Delta x)_\perp \sim r \sim v_{\mathrm{th}}/\omega_c$, with ω_c the cyclotron frequency. Therefore the heat conductivity in perpendicular direction is

$$\kappa_\perp \sim \frac{n}{\tau}\left(\frac{v_{\mathrm{th}}}{\omega_c}\right)^2. \tag{33}$$

Two interesting conclusions, that we can derive from the two heat conductivities for parallel and perpendicular dynamics are found. By comparing the expressions for electrons and ions

$$\frac{\kappa_\parallel^e}{\kappa_\parallel^i} \sim \left(\frac{M_i}{m_e}\right)^{1/2} \quad \text{and} \quad \frac{\kappa_\perp^e}{\kappa_\perp^i} \sim \left(\frac{m_e}{M_i}\right)^{1/2}, \tag{34}$$

we find that the parallel electron heat conductivity is about a factor square root of mass ratio larger than the parallel ion heat conductivity, since the thermal velocity of electrons is larger by this factor. For the perpendicular direction, it is vice versa, since the ion Larmor radius is larger by a factor $(m_e/M_i)^{1/2}$. We have to emphasise here, that our small Gedankenexperiment covers just classical transport. In a toroidal fusion device, the perpendicular transport is nearly always dominated by either neoclassical transport or turbulence. Therefore the perpendicular classical transport is often negligible.

2.2.2 Derivation of the Braginskii coefficients for the Lorentz approximation

This section is dedicated to the derivation of the closure coefficients which are an essential part of the applicability of the Braginskii closure in quantitative calculations. This section follows the derivation which is done in [43] and [55]. The starting point of our derivation is the kinetic equation for electrons

$$\frac{\partial}{\partial t} f_e + \boldsymbol{v} \cdot \nabla f_e - \frac{e}{m} \boldsymbol{E} + \omega_{ce} \left(\boldsymbol{b} \times \boldsymbol{v} \right) \cdot \nabla_v f_e = C_e \left(f_e \right), \tag{35}$$

with $\omega_{ce} = eB/m_e$ the electron cyclotron frequency. To find closure approximations is necessary to make a fluid model applicable, but not generally possible without further assumptions. The Braginkii closure uses the assumption of high collisionality, i.e.

$$\frac{L_{\text{ref}}}{\lambda_{\text{mfp}}} \gg 1, \tag{36}$$

with the mean free path $\lambda_{\text{mfp}} = v_{\text{th},\alpha} \tau_\alpha$, defined by the thermal velocity $v_{\text{th},\alpha} = (T_\alpha/m_\alpha)^{1/2}$ and the collision time

$$\tau_e = \frac{12}{\sqrt{2}} \pi^{3/2} \frac{\sqrt{m_e} T_e^{3/2} \varepsilon_0^2}{n_i Z^2 e^4 \lambda} \quad \text{and} \quad \tau_i = 12 \pi^{3/2} \frac{\sqrt{M_i} T_i^{3/2} \varepsilon_0^2}{n_i Z^4 e^4 \lambda} \tag{37}$$

or in more practical units

$$\tau_e = 3.44 \cdot 10^{11} \text{ s} \, \frac{1\,\text{m}^{-3}}{n_e} \left(\frac{T_e}{1\,\text{eV}} \right)^{3/2} \frac{1}{Z\lambda}, \tag{38}$$

with Z the charge number of the ions under consideration and λ the coulomb logarithm

$$\lambda = \begin{cases} 23 - 0.5 \log_{10} \left(n_e / 1\,\text{m}^{-3} \right) + 1.5 \log_{10} \left(T_e / 1\,\text{eV} \right) & \text{for } \text{T}_\text{e} < 10\,\text{eV}, \\ 24 - 0.5 \log_{10} \left(n_e / 1\,\text{m}^{-3} \right) + 1.0 \log_{10} \left(T_e / 1\,\text{eV} \right) & \text{for } \text{T}_\text{e} > 10\,\text{eV}. \end{cases} \tag{39}$$

as defined in [61]. Note that there is no $2^{-1/2}$ missing in the definition of τ_i in eq. (37), instead the definition was chosen to stay consistent to Braginskii [43]. To avoid confusion, we want to mention here that different definitions of collisionality are common depending on the choice of L_{ref}. In neoclassical theory for example the parallel distance around a flux surface is chosen $L_{\text{ref}} = qR$, with the safety factor q and the major radius R. For our purpose the reference length L_{ref} represents the length scale on which macroscopic quantities, e.g. the electron temperature, changes. We use the inverse collisionality to define a small parameter

$$\varepsilon = \frac{\lambda^e_{\mathrm{mfp}}}{L_{\mathrm{ref}}} \ll 1, \tag{40}$$

which corresponds to the Knudsen number in fluid dynamics of neutral fluids. With the parameter ε we can expand the distribution function as a series

$$f_e = f_{e0} + \varepsilon f_{e1} + \varepsilon^2 f_{e2} + ..., \tag{41}$$

which converges fast in the limit of high collisionality, as $\varepsilon \to 0$. This method is known as the Chapman-Enskog procedure and can be found in great detail e.g. in [60]. The lowest order f_{e0} is a Maxwellian with the explicit form

$$f_{e0}(v) = n_e \left(\frac{m_e}{2\pi T_e}\right)^{3/2} \exp\left(-\frac{m_e v^2}{2T_e}\right) \tag{42}$$

in the rest frame, which means we have no mean velocity $\boldsymbol{u}$. To derive the original closure from Braginskii we have to retain the contributions of order zero and one, which means a Maxwellian plus a small perturbation. In the kinetic equation, the magnetic term and the collisional term are the dominant ones according to the ordering scheme. Those two terms vanish for a Maxwellian

$$\omega_{ce} \left(\boldsymbol{b} \times \boldsymbol{v}\right) \cdot \nabla_v f_{e0} = C_e \left(f_{e0}\right) = 0, \tag{43}$$

which means that for the whole kinetic equation, we have to use f_{e1} in the magnetic term and the collisional one, for the other terms of the kinetic equation we use the lowest order f_{e0}. Therefore we find the equation

$$\frac{\partial}{\partial t} f_{e0} + \boldsymbol{v} \cdot \nabla f_{e0} - \frac{e}{m} \boldsymbol{E}\, \nabla_v f_{e0} + \omega_{ce} \left(\boldsymbol{b} \times \boldsymbol{v}\right) \cdot \nabla_v f_{e1} = C_e \left(f_{e1}\right), \tag{44}$$

which we have to solve in order to find a solution for f_{e1}. The time derivative vanishes $\partial f_{e0}/\partial t = 0$ since we are in steady state conditions and the Maxwellian does not depend on time. We evaluate the terms which act on f_{e0} and we can express those in terms of fluid moments

$$
\begin{aligned}
\boldsymbol{v}\cdot\boldsymbol{Q}(v) &= \boldsymbol{v}\cdot\nabla f_{e0} - \frac{e}{m_e}\boldsymbol{E}\cdot\nabla_v f_{e0} \\
&= \boldsymbol{v}\cdot\left(\frac{1}{n}f_{e0}\nabla n - \frac{3}{2T_e}f_{e0}\nabla T_e - \left(-\frac{m_e v^2}{2T_e^2}\right)f_{e0}\nabla T_e\right) - \frac{e}{m_e}\boldsymbol{E}\cdot\left(-\frac{m_e\boldsymbol{v}}{T_e}f_{e0}\right) \\
&= \boldsymbol{v}\cdot\left(\frac{\nabla n}{n} - \frac{3}{2}\frac{\nabla T_e}{T_e} + \frac{m_e v^2}{2T_e}\frac{\nabla T_e}{T_e}\right)f_{e0} + \frac{e}{T_e}\boldsymbol{E}\cdot\boldsymbol{v}f_{e0} \\
&= \boldsymbol{v}\cdot\left(\frac{T_e\nabla n}{nT_e} + \frac{n\nabla T_e}{nT_e} - \frac{5}{2}\frac{\nabla T_e}{T_e} + \frac{m_e v^2}{2T_e}\frac{\nabla T_e}{T_e}\right)f_{e0} + \frac{e}{T_e}\boldsymbol{E}\cdot\boldsymbol{v}f_{e0} \\
&= \boldsymbol{v}\cdot\left(\frac{\nabla p_e}{p_E} - \frac{5}{2}\frac{\nabla T_e}{T_e} + \frac{m_e v^2}{2T_e}\frac{\nabla T_e}{T_e}\right)f_{e0} + \frac{e}{T_e}\boldsymbol{E}\cdot\boldsymbol{v}f_{e0} \\
&= \boldsymbol{v}\cdot\left(\nabla\ln p_e + \frac{e}{T_e}\boldsymbol{E} + \left(\frac{m_e v^2}{2T_e} - \frac{5}{2}\right)\nabla\ln T_e\right)f_{e0} \\
&= \boldsymbol{v}\cdot\left(\boldsymbol{A}_1 + \left(\frac{m_e v^2}{2T_e} - \frac{5}{2}\right)\boldsymbol{A}_2\right)f_{e0},
\end{aligned}
\tag{45}
$$

where $\boldsymbol{A}_1$ and $\boldsymbol{A}_2$ are the *thermodynamic forces*. Now we deviate from the derivation that was done by Braginskii [43]. He used the approximation of a Landau collision operator in his work to derive a closure for arbitrary values for the charge number of the ions Z. The full derivation is quite cumbersome and would require much more space of this thesis than I can provide. Therefore we use a special case in which the derivation becomes much simpler, but the process still provides valuable insights. We use the approximation of the Lorentz collision operator instead, which describes how electrons collide with infinitely heavy ions. We will see that therefore it is enough to solve for the perturbed electron distribution function f_{e1} and we do not need to calculate the perturbed ion distribution function, in contrast to Braginskii. The Lorentz collision operator reads

$$
C_e\left(f_{e1}\right) = \nu_{ei}(v)\mathcal{L}\left(f_{e1}\right), \tag{46}
$$

with $\nu_e = (3\sqrt{\pi}/4)\tau_e^{-1}\left(v_{\mathrm{th},e}^3/v^3\right)$ a velocity-dependent collision frequency, which consists of a numerical prefactor, τ_e^{-1} as expected for a collision frequency and a velocity correction proportional to v^{-3}, which originates in the nature of coulomb collisions. $\mathcal{L}(f)$ is defined as

$$
\mathcal{L}\left(f\right) = \frac{1}{2}\left(\frac{1}{\sin\theta}\frac{\partial}{\partial\theta}\left(\sin\theta\frac{\partial f}{\partial\theta}\right) + \frac{1}{\sin^2\theta}\frac{\partial^2 f}{\partial\varphi^2}\right), \tag{47}
$$

with the azimuthal angle φ and the polar angle θ in spherical coordinates. It is interesting to note, that since the ions are infinitely heavy, the velocity of electrons is conserved, therefore no derivatives in v appear in this collision operator. For the Lorentz collision operator applied to the velocity vector, we find $\mathcal{L}(\boldsymbol{v}) = -\boldsymbol{v}$. Therefore the Ansatz $f_{e1}(\boldsymbol{v}) = \boldsymbol{v}\cdot\boldsymbol{F}(v)$ is chosen and we find the equation

$$
-\nu_{ei}\left(v\right)\boldsymbol{v}\cdot\boldsymbol{F}(v) - \omega_{ce}\left(\boldsymbol{b}\times\boldsymbol{v}\right)\cdot\boldsymbol{F}(v) = \boldsymbol{v}\cdot\boldsymbol{Q}(v), \tag{48}
$$

which has to be true for any choice of $\boldsymbol{v}$ and therefore becomes

$$\nu_{ei}(v)\boldsymbol{F}(v) + \omega_{ce}\boldsymbol{b} \times \boldsymbol{F}(v) = -\boldsymbol{Q}(v). \tag{49}$$

From this equation, we can already see the parallel part $F_\parallel = -Q_\parallel(v)/v_{ei}(v)$, which is the part we are mainly interested in for the closure expression of the parallel heat flux. The perpendicular components we can determine by taking the cross-product of the equation and solving this system of equations. The final result we get is

$$f_{e1}(\boldsymbol{v}) = -\left(\frac{\boldsymbol{v}_\parallel}{\nu_{ei}(v)} + \frac{\nu_{ei}(v)\boldsymbol{v}_\perp + \omega_{ce}\boldsymbol{b} \times \boldsymbol{v}}{\nu_{ei}^2(v) + \omega_{ce}^2}\right) \cdot \boldsymbol{Q}(v). \tag{50}$$

By using the ordering parameter $\Delta = \nu_{ei}(v)/\omega_{ce} = \rho_e/\lambda_{\text{mfp}} \ll 1$ we can rewrite the solution to f_{e1} as

$$f_{e1}(\boldsymbol{v}) = -\left(\frac{\boldsymbol{v}_\parallel}{\nu_{ei}(v)} + \frac{\boldsymbol{b} \times \boldsymbol{v}}{\omega_{ce}} + \frac{\nu_{ei}(v)\boldsymbol{v}_\perp}{\omega_{ce}^2}\right) \cdot \boldsymbol{Q}(v) = f_{e1\parallel} + f_{e1\wedge} + f_{e1\perp} \tag{51}$$

and since we know now the form of the perturbed distribution function f_{e1} we can find now the closure expression by taking moments over it. For $\boldsymbol{u}$ we get

$$n\boldsymbol{u} = \int f_{e1}\boldsymbol{v}\ \mathrm{d}^3v = n\left(\boldsymbol{u}_\parallel + \boldsymbol{u}_\wedge + \boldsymbol{u}_\perp\right), \tag{52}$$

where we do not need a closure expression formally, but we will need this expression to identify the conductive and the convective part of the parallel heat flux. This equation is not our main interest, therefore we do not perform here a major calculation to derive it. The solution for the parallel mean velocity is

$$nu_\parallel = -\frac{32}{3\pi}\frac{\tau_{ei}}{m_e}\left(\nabla_\parallel p_e + neE_\parallel + \frac{3}{2}n\nabla_\parallel T_e\right). \tag{53}$$

The heat flux we can calculate according to

$$\boldsymbol{q} = \int f_{e1}\left(\frac{m_e v^2}{2} - \frac{5T_e}{2}\right)\boldsymbol{v}\ \mathrm{d}^3v = n\left(\boldsymbol{q}_\parallel + \boldsymbol{q}_\wedge + \boldsymbol{q}_\perp\right), \tag{54}$$

where this unusual form of the heat flux connects to the standard definition by

$$\begin{aligned}
\boldsymbol{q} &= \int \frac{m_e}{2} f_{e1}\left(v-u\right)^2\left(\boldsymbol{v}-\boldsymbol{u}\right)\mathrm{d}^3v \\
&= \int \frac{m_e}{2} f_{e1}v^2\boldsymbol{v}\ \mathrm{d}^3v - m_e\boldsymbol{u}\cdot\boldsymbol{P}_e - \frac{3m_e}{2}\boldsymbol{u}p_e + \frac{1}{2}m_e n u^2\boldsymbol{u} \\
&\approx \int \frac{m_e}{2} f_{e1}v^2\boldsymbol{v}\ \mathrm{d}^3v - \frac{5m_e}{2}\boldsymbol{u}p_e \\
&= \int f_{e1}\left(\frac{m_e v^2}{2} - \frac{5T_e}{2}\right)\boldsymbol{v}\ \mathrm{d}^3v,
\end{aligned} \tag{55}$$

where we considered the mean velocity u to be small compared to the thermal velocity v_{th}, therefore, the term $m_e n u^2\boldsymbol{u}/2$ is considered small and vanishes from line 2 to line 3. Furthermore, we assume that the pressure is isotropic, which means that $\boldsymbol{P}_e = \boldsymbol{I}p_e$ with

$\boldsymbol{I}$ the unity matrix. The last part that is left to do is calculating the parallel heat flux that follows from the distribution function $f_{e1\parallel}$ explicitly. Therefore we calculate

$$\begin{aligned}\boldsymbol{q}_\parallel &= \int f_{e1\parallel}\left(\frac{m_e v^2}{2}-\frac{5T_e}{2}\right)\boldsymbol{v}\,\mathrm{d}^3v \\ &= \int -\frac{\boldsymbol{v}_\parallel}{\nu_{ei}(v)}\cdot\left(\boldsymbol{A}_1+\left(\frac{m_e v^2}{2T_e}-\frac{5}{2}\right)\boldsymbol{A}_2\right) f_{e0}\left(\frac{m_e v^2}{2}-\frac{5T_e}{2}\right)\boldsymbol{v}\,\mathrm{d}^3v \\ &= -\frac{4\tau_{ei}T_e}{3\sqrt{\pi}v_{\mathrm{th},e}^3}\int v^3 v_\parallel\left(\left(\frac{m_e v^2}{2T_e}-\frac{5}{2}\right)A_{1\parallel}+\left(\frac{m_e v^2}{2T_e}-\frac{5}{2}\right)^2 A_{2\parallel}\right) f_{e0}\boldsymbol{v}\,\mathrm{d}^3v,\end{aligned} \tag{56}$$

with $A_{1\parallel}=\nabla_\parallel \ln p_e+(e/T_e)E_\parallel$ and $A_{2\parallel}=\nabla_\parallel \ln T_e$. To perform the integration we have to make a coordinate transformation into spherical coordinates with the parallel direction along the z-axis, so $\theta=\pi$. In spherical coordinates, all components but the parallel one vanish due to the integration over φ due to the vector $\boldsymbol{v}$. Therefore we can write our equation as a scalar equation for simplicity

$$q_\parallel = -\frac{4\tau_{ei}T_e}{3\sqrt{\pi}v_{\mathrm{th},e}^3}\int v^3 v_\parallel\left(\left(\frac{m_e v^2}{2T_e}-\frac{5}{2}\right)A_{1\parallel}+\left(\frac{m_e v^2}{2T_e}-\frac{5}{2}\right)^2 A_{2\parallel}\right) f_{e0}v_\parallel\,\mathrm{d}^3v, \tag{57}$$

where we replaced $\boldsymbol{v}$ with $v_\parallel$. For the calculation, we use the following integral identities

$$\begin{aligned}\int_0^\infty x^7\exp(-ax^2)\,\mathrm{d}x &= 3a^{-4},\\ \int_0^\infty x^9\exp(-ax^2)\,\mathrm{d}x &= 12a^{-5},\\ \int_0^\infty x^{11}\exp(-ax^2)\,\mathrm{d}x &= 60a^{-6},\end{aligned} \tag{58}$$

which we need for the integral in v. Further we use the identity $\int_0^\pi \cos^2\theta\sin\theta\,\mathrm{d}\theta=2/3$, which can be easily verified by substituting $u=\cos\theta$. The detailed calculation is written here:

$$
\begin{aligned}
q_\parallel &= -\frac{4\tau_{ei}T_e}{3\sqrt{\pi}v_{\mathrm{th},e}^3}\int v^3 v_\parallel \left(\left(\frac{m_e v^2}{2T_e}-\frac{5}{2}\right)A_{1\parallel}+\left(\frac{m_e v^2}{2T_e}-\frac{5}{2}\right)^2 A_{2\parallel}\right) f_{e0} v_\parallel \,\mathrm{d}^3v \\
&= -\frac{4\tau_{ei}T_e}{3\sqrt{\pi}v_{\mathrm{th},e}^3}\int_0^\infty\int_0^\pi\int_0^{2\pi} v^3 v\cos\theta \left(\left(\frac{m_e v^2}{2T_e}-\frac{5}{2}\right)A_{1\parallel}+\left(\frac{m_e v^2}{2T_e}-\frac{5}{2}\right)^2 A_{2\parallel}\right) f_{e0} \\
&\qquad\qquad \times v\cos\theta\, v^2\sin\theta \,\mathrm{d}\varphi\,\mathrm{d}\theta\,\mathrm{d}v \\
&= -\frac{4\tau_{ei}T_e}{3\sqrt{\pi}v_{\mathrm{th},e}^3}2\pi\int_0^\infty\int_0^\pi v^4 \left(\left(\frac{m_e v^2}{2T_e}-\frac{5}{2}\right)A_{1\parallel}+\left(\frac{m_e v^2}{2T_e}-\frac{5}{2}\right)^2 A_{2\parallel}\right) f_{e0} \\
&\qquad\qquad \times v^3\cos^2\theta\sin\theta\,\mathrm{d}\theta\,\mathrm{d}v \\
&= -\frac{4\tau_{ei}T_e}{3\sqrt{\pi}v_{\mathrm{th},e}^3}\frac{4\pi}{3}\int_0^\infty v^7\left(\left(\frac{m_e v^2}{2T_e}-\frac{5}{2}\right)A_{1\parallel}+\left(\frac{m_e^2 v^4}{4T_e^2}-\frac{5m_e v^2}{2T_e}+\frac{25}{4}\right)A_{2\parallel}\right) f_{e0}\,\mathrm{d}v \\
&= -\frac{4\tau_{ei}T_e}{3\sqrt{\pi}v_{\mathrm{th},e}^3}\frac{4\pi}{3}\int_0^\infty \left(\left(\frac{m_e}{2T_e}v^9-\frac{5}{2}v^7\right)A_{1\parallel}+\left(\frac{m_e^2}{4T_e^2}v^{11}-\frac{5m_e}{2T_e}v^9+\frac{25}{4}v^7\right)A_{2\parallel}\right) \\
&\qquad\qquad \times \frac{n m_e^{3/2}}{(2\pi T_e)^{3/2}}\exp\left(-\frac{m_e v^2}{2T_e}\right)\mathrm{d}v \\
&= -\frac{4\tau_{ei}T_e m_e^{3/2}}{3\sqrt{\pi}(2T_e)^{3/2}}\frac{4\pi}{3}\frac{n m_e^{3/2}}{(2\pi T_e)^{3/2}}\Bigg[\left(\frac{m_e}{2T_e}\frac{12(2T_e)^5}{m_e^5}-\frac{5}{2}\frac{3(2T_e)^4}{m_e^4}\right)A_{1\parallel} \\
&\qquad\qquad + \left(\frac{m_e^2}{4T_e^2}\frac{60(2T_e)^6}{m_e^6}-\frac{5m_e}{2T_e}\frac{12(2T_e)^5}{m_e^5}+\frac{25}{4}\frac{3(2T_e)^4}{m_e^4}\right)A_{2\parallel}\Bigg] \\
&= -\frac{2\tau_{ei}n m_e^3}{9\pi T_e^2}\left[\frac{T_e^4}{m_e^4}(192-120)A_{1\parallel}+\frac{T_e^4}{m_e^4}(960-960+300)A_{2\parallel}\right] \\
&= -\frac{2\tau_{ei}n m_e^3}{9\pi T_e^2}\frac{T_e^4}{m_e^4}\left[72\left(\nabla_\parallel\ln p_e+\frac{e}{T_e}E_\parallel\right)+300\nabla_\parallel\ln T_e\right] \\
&= -\frac{2\tau_{ei}nT_e^2}{9\pi m_e}\left[72\left(\frac{\nabla_\parallel p_e}{nT_e}+\frac{e}{T_e}E_\parallel\right)+300\frac{\nabla_\parallel\ln T_e}{T_e}\right] \\
&= -\frac{3}{2}nT_e\frac{32}{3\pi}\left(\frac{1}{n}\nabla_\parallel p_e+eE_\parallel+\frac{3}{2}\nabla_\parallel T_e\right)-\frac{2\tau_{ei}nT_e}{9\pi m_e}(300-108)\nabla_\parallel T_e \\
&= -\frac{3}{2}nT_e\,u_\parallel-\frac{128}{3\pi}\frac{nT_e\tau_{ei}}{m_e}\nabla_\parallel T_e
\end{aligned}
\tag{59}
$$

In the second last line, we have rearranged the terms to identify the expression for $u_\parallel$. This is the exact closure term proposed by Braginskii [43] for the case of $Z \gg 1$.

2.2.3 Braginskii closure for Hydrogen ($Z = 1$)

The main difference to the derivation in the last chapter is the assumptions on the collision operator. We used the approximation of a Lorentz collision operator, which simplified the analytical derivation in the last chapter, but limited the result to the limit of $Z \to \infty$. To derive an applicable fluid closure for hydrogen and deuterium plasmas we have to use

the Landau collision operator, as Braginskii did. This makes the whole calculation a lot more difficult and cumbersome since we have to solve not only for the perturbed electron distribution function but also for the perturbed ion distribution function. The interested reader is referred to the original publication [43], where the procedure is sketched. We will just state the results that he found. The closure for the parallel heat flux takes the form

$$q_{\parallel\alpha}^{\mathrm{BR}} = -\kappa_{\parallel\alpha}^{\mathrm{BR}} \nabla_{\parallel} T_\alpha \quad \text{with} \quad \kappa_{\parallel\alpha}^{\mathrm{BR}} = \begin{cases} 3.16\, n\, v_{\mathrm{th},e}^2\, \tau_e & \alpha = e, \\ 3.9\, n\, v_{\mathrm{th},i}^2\, \tau_i & \alpha = i. \end{cases} \tag{60}$$

In the full Braginskii model eq. (60) this is just the diffusion term of the parallel conductive heat flux, additionally there is the thermal force and diamagnetic heat conduction that also contribute to the total parallel heat flux. Just the first part will be changed by the different closures introduced in the following sections. The Braginskii closure is robustly valid for highly collisional magnetised plasmas. For decreasing collisionality, however, the closure loses its validity. In regimes of high collisionality collisions can drive the plasma distribution function back to a Maxwellian very efficiently, but this mechanism weakens as the plasma becomes less collisional. Specifically, the issue that arises for parallel heat conductivity $\kappa_{\parallel\alpha}^{\mathrm{BR}} \propto T_\alpha^{5/2}$. Only a very collisional plasma obeys this temperature dependence, however, for low collisional plasmas, the heat conductivity is dramatically overestimated due to the strong temperature dependence.

2.2.4 Why is the Braginskii closure for $q_\parallel$ so fragile?

With the knowledge we have gained in the last sections, we are able to answer the question of why the collisional closure for the parallel conductive heat flux $q_\parallel$ is the most fragile quantity in terms of collisionality. First, we have to keep in mind that the derivation of the Braginskii closure relies on the assumption of high collision, i.e. $L_{\mathrm{ref}}/\lambda_{\mathrm{mfp}} \gg 1$. While this is usually true in fusion devices for the perpendicular direction since here not λ_{mfp} is the distance the particles travel but the gyroradius, it does not hold along the magnetic field [62]. The second point is that the lower fluid moments n, $\boldsymbol{u}$, T and p are all mainly defined by the Maxwellian part f_0 in Braginskiis derivation, while the parallel heat flux $q_\parallel$ and the stress tensor $\boldsymbol{\Pi}$ are purely defined via f_1. Furthermore, $q_\parallel$ is even more fragile than $\boldsymbol{\Pi}$ since it corresponds to a higher moment. Therefore it is reasonable that $q_\parallel$ becomes unreasonable most quickly, as the assumption of the expansion parameter being small $\varepsilon \ll 1$ breaks for low collisionality. This is the reason so much effort is put into the task of finding a better approximation for $q_\parallel$ in this thesis, since then the range of validity of the whole fluid model would be extended, by making the most fragile part more robust.

2.2.5 Flux limiters

A common method to make the fluid description of plasmas also applicable to lower collisional cases is the introduction of heat-flux limiters as proposed e.g. in Stangeby [63], chapter 26. Since the Braginskii closure is derived in the limit of high collisionality, we should not trust its predictions for cases outside its validity. It feels natural to introduce an upper limit, since

$$\kappa_{\parallel}^{\mathrm{BR}} \xrightarrow[(L_{\mathrm{ref}}/\lambda_{\mathrm{mfp}}) \to 0]{} \infty \tag{61}$$

in the extreme case of a collisionless system. But how is heat transported in a collisionless plasma? Without collisions, particles move freely along field lines and carry their heat with them. Those freely moving particles translate into the fluid picture as a flow of heat in parallel direction with the thermal velocity $nv_{\mathrm{th},\alpha}T_\alpha$. By casting this free-streaming heat flux in the form of a heat conductivity times a parallel temperature gradient we arrive at the free-streaming heat flux

$$q_{\parallel\alpha}^{\mathrm{FS}} = -\kappa_{\parallel\alpha}^{\mathrm{FS}} \nabla_{\parallel} T_\alpha \quad \text{with} \quad \kappa_{\parallel\alpha}^{\mathrm{FS}} = n\, v_{\mathrm{th},\alpha}\, q_{95} R_0, \tag{62}$$

with q_{95} the safety factor at $\rho = 0.95$ and R_0 the major radius of the tokamak. Here we have already approximated the gradient scale length to the parallel connection length in the tokamak edge $T_\alpha/|\nabla_{\parallel} T_\alpha| = q_{95}R_0$ and we use q_{95} instead of the local safety factor to avoid a divergence at the separatrix. This free-streaming heat flux is used as an upper limit. The Braginskii and the free-streaming heat flux are combined via a harmonic average to form the flux-limited heat flux

$$q_{\parallel\alpha}^{\mathrm{FL}} = \left(\frac{1}{q_{\parallel\alpha}^{\mathrm{BR}}} + \frac{1}{\alpha q_{\parallel\alpha}^{\mathrm{FS}}} \right)^{-1}, \tag{63}$$

with $\alpha \in [0.03, 3]$ the flux-limiting parameter for tuning the upper limit. This parameter α is adjusted according to kinetic simulations and experimental data. To find a single parameter α that is well suited for all regimes seems unlikely due to the ad hoc nature of this closure. A fundamental collection of values for α according to various kinetic studies is presented e.g. in Fundamenski et al. [64]. This approach is also used in turbulence simulations where a strong dependence of the radial heat transport on α is observed [40, 65]. Performing simulations of experiments and machines that have not been conducted or built yet and predicting divertor heat fluxes and edge profiles is not feasible with flux-limited heat fluxes, which is the major drawback of this approach.

2.2.6 Hammett-Perkins closure

A more elaborate approach to predict heat fluxes within a fluid model for collisionless plasmas was proposed by Hammett and Perkins [45]. This fluid closure was developed with the intention of including the kinetic effect of linear Landau damping [66] into fluid models, in particular from phase mixing due to free streaming along the magnetic field. How should we think of linear Landau damping? We consider just ions to stay close to the derivation in [45] and omit the index of species for all quantities in this chapter. For electrons the derivation is analogous. To approach this question we consider the one-dimensional Vlasov equation

$$\frac{\partial}{\partial t} f(x,v,t) + v \frac{\partial}{\partial x} f(x,v,t) + \frac{e}{m} E \frac{\partial}{\partial v} f(x,v,t) = 0, \tag{64}$$

which describes a one-dimensional collisionless system, with the spatial coordinate x along the magnetic field. We want to investigate, how the system responds to a small driving electric field $E = -\partial\tilde{\phi}/\partial x$. Since the drive is small, we can linearize the kinetic

equation by splitting $f(x,v,t) = f_0(v) + \varepsilon\tilde{f}(x,v,t)$ and neglect quadratic terms in $\tilde{f}$, the expansion parameter is here $\varepsilon = e\tilde{\phi}/T_0 \ll 1$, which holds true as long as $L \gg \lambda_D$. Since $f_0(v)$ has neither a spatial nor temporal dependence, those derivatives vanish when applied to f_0. In the velocity derivative, we keep just f_0, since $\tilde{f}$ is an order ε smaller. The linearized equation reads

$$\frac{\partial}{\partial t}\tilde{f} + v\frac{\partial}{\partial x}\tilde{f} - \frac{e}{m}\frac{\partial\tilde{\phi}}{\partial x}\frac{\partial}{\partial v}f_0 = 0, \tag{65}$$

which is Fourier-transformed, wherein perturbed quantities vary as $\exp(ikx - i\omega t))$, to

$$-i\omega\tilde{f} + vik\tilde{f} - \frac{e}{m}ik\tilde{\phi}\frac{\partial f_0}{\partial v} = 0 \tag{66}$$

and after rearranging the terms and performing a velocity space integral we arrive at

$$\tilde{n} = \int \tilde{f}\,\mathrm{d}v = \frac{e\tilde{\phi}}{T_0}kv_{\mathrm{th0}}^2\int\frac{\partial f_0/\partial v}{vk-\omega}\,\mathrm{d}v, \tag{67}$$

where we can see in the denominator of the integrand that we are dealing with a resonance phenomenon. This integral has to be treated with care and was already subject to a dispute between Vlasov and Landau [66]. However, the treatment of Landau is the correct one, wherein ω is a complex quantity and special attention has to be paid to the pole of the complex function at $v = \omega/k$. If $\mathfrak{Im}(\omega) > 0$, we can perform the integral along the real axis. However, for $\mathfrak{Im}(\omega) < 0$ the integration path has to be deformed around the pole as shown in fig. 10.

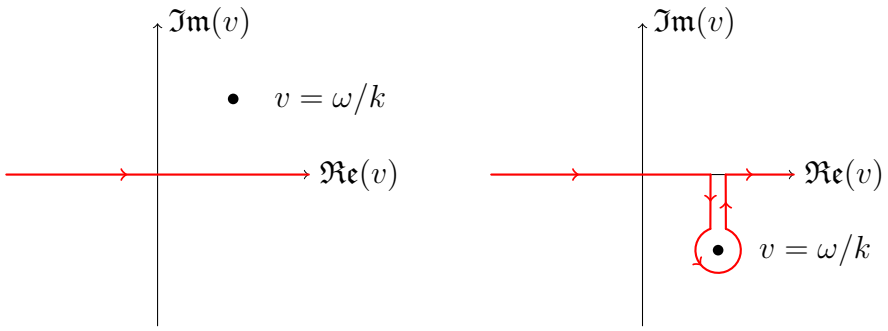

Figure 10: Contour integral in the complex plane of velocity space, if $\mathfrak{Im}(\omega) > 0$ the integral can be performed along the real axis, if $\mathfrak{Im}(\omega) < 0$ the contour has to be deformed around the pole

We may define the linear response function $R(\Omega)$ by

$$\tilde{n} = -\frac{e\tilde{\phi}}{T_0}n_0R(\Omega) = \frac{e\tilde{\phi}}{T_0}kv_{\mathrm{th0}}^2\int\frac{\partial f_0/\partial v}{vk-\omega}\,\mathrm{d}v, \tag{68}$$

with $\Omega = \omega/(2^{1/2}v_{\mathrm{th0}}|k|)$. Ω can be thought of as the ratio between the phase velocity $v_{\mathrm{ph}} = \omega/|k|$ of the electrostatic wave and the thermal velocity of the plasma $\Omega = 2^{-1/2}v_{\mathrm{ph}}/v_{\mathrm{th0}}$. This linear kinetic response function can also be expressed in terms of the plasma dispersion function

$$Z(\Omega) = \frac{1}{\sqrt{\pi}} \int \frac{\exp\left(-t^2\right)}{t - \Omega} \, \mathrm{d}t \tag{69}$$

in a clear form

$$R(\Omega) = 1 + \Omega Z(\Omega). \tag{70}$$

To get an intuitive feeling of how $R(\Omega)$ looks like, we evaluate the integral equation numerically for different real values of Ω ($\mathfrak{Im}(\Omega) = 0$) and plot the real and imaginary part of the $R(\Omega)$ in fig. 11. We observe two interesting aspects. Firstly, for $\Omega = 0$ we find $\mathfrak{Re}(R(\Omega = 0)) = 1$ and $\mathfrak{Im}(R(\Omega = 0)) = 0$, so the perturbed density follows instantaneously the driving electrostatic potential $\tilde{\phi}$, this behaviour is usually known as adiabatic response. Secondly, we notice that for increasing Ω the imaginary part of $R(\Omega)$ is growing, which means physically a damping of the driving wave. This collisionless damping of the driving wave is the representation of linear Landau damping in this linearized model. We note also, that the maximum of $\mathfrak{Im}(R(\Omega))$ is at $\Omega = 2^{-1/2}$ which means $v_{\mathrm{ph}} = v_{\mathrm{th0}}$.

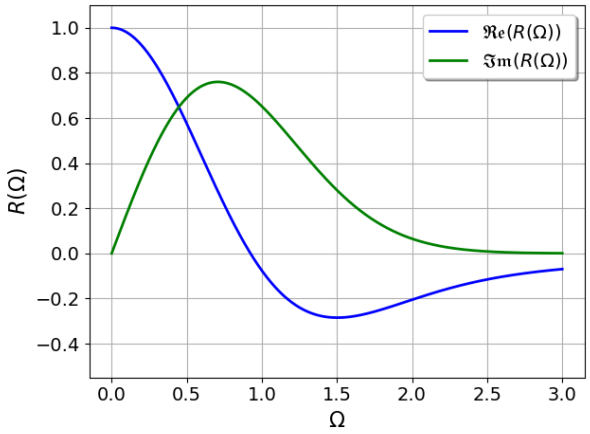

Figure 11: Real and imaginary part of the linear kinetic response function $R(\Omega)$

In their paper [45] Hammett and Perkins propose a fluid closure that is able to approximate this form of the linear response function within a fluid model. This closure takes the form

$$\tilde{q}_k^{\mathrm{HP}} = -A \frac{ik}{|k|} \tilde{T}_k, \tag{71}$$

with $A = n_0 v_{\mathrm{th0}} \sqrt{8/\pi}$, i the imaginary unit, k the wave vector (here one-dimensional) and the index k indicating the formulation in wave number space. Henceforth we will refer to eq. (71) as Hammett-Perkins closure. To understand how this closure reproduces the linear response function we investigate a one-dimensional fluid model

$$\frac{\partial}{\partial t} n + \frac{\partial}{\partial x} (un) = 0, \tag{72}$$

$$\frac{\partial}{\partial t} (mnu) + \frac{\partial}{\partial x} (unmu) = -\frac{\partial}{\partial x} p + enE, \tag{73}$$

$$\frac{\partial}{\partial t}p + \frac{\partial}{\partial x}(up) = -2p\frac{\partial}{\partial x}u - \frac{\partial}{\partial x}q, \tag{74}$$

which we obtain by taking moments over eq. (64). We linearize the fluid quantities by splitting all quantities into a background f_0 and a fluctuating quantity $\tilde{f}$, similar to the calculation of the linear kinetic response eq. (68). The background quantities have no spatial and temporal dependencies, therefore these derivatives vanish. Furthermore, we note that even moments in v, so u and q have no background quantity in an unshifted Maxwellian, therefore $u_0 = q_0 = 0$ vanish. Quadratic fluctuation terms are ignored again. We find the linearized set equations

$$\frac{\partial}{\partial t}\tilde{n} + \frac{\partial}{\partial x}(\tilde{u}n_0) = 0, \tag{75}$$

$$\frac{\partial}{\partial t}(mn_0\tilde{u}) = -\frac{\partial}{\partial x}\tilde{p} - en_0\frac{\partial}{\partial x}\tilde{\phi}, \tag{76}$$

$$\frac{\partial}{\partial t}\tilde{p} + \frac{\partial}{\partial x}(\tilde{u}p_0) = -2p_0\frac{\partial}{\partial x}\tilde{u} - \frac{\partial}{\partial x}\tilde{q}, \tag{77}$$

where the definition of the electric field was inserted. Note that the second term on the left-hand side in the second equation vanished since just terms of higher order appear. We take again a Fourier transform of all three equations where fluctuating quantities vary as $\exp(ikx - i\omega t)$. We find for the first equation how to express the fluctuating velocity $\tilde{u} = \omega/(n_0 k)\tilde{n}$ in terms of the fluctuating density. For the second equation, we find equivalently an expression for the fluctuating pressure $\tilde{p} = (\omega/k)mn_0\tilde{u} - en_0\tilde{\phi}$.

Response function for closure $\tilde{q} = 0$

With this set of equations, we can now take different closures for $\tilde{q}$ and calculate the response function of the fluid system. We start with the simplest possible closure $\tilde{q} = 0$. This closure we insert into eq. (77), then substitute $\tilde{p}$ and $\tilde{u}$ afterwards. We are left with an algebraic equation, where we substitute finally Ω for ω and find the response function

$$R_0(\Omega) = \frac{1}{3 - 2\Omega^2}, \tag{78}$$

where we observe that this response function has no imaginary part. So there is no approximation of any kind of damping in this model. We see the strong deviation also by comparing the two response functions in fig. 12. $R_0(\Omega)$ does not even match $\mathfrak{Re}(R(\Omega))$ the limit $\Omega \to 0$, between $\Omega = 1.0$ and $\Omega = 1.5$ we see an undamped resonance, where $R_0(\Omega) \to \infty$, as expected for an oscillator without damping. The limit of high Ω corresponds with the linear kinetic response.

Response function for the Hammett-Perkins closure

For the Hammett-Perkins closure eq. (88) we find after a more involved calculation a response function of the form

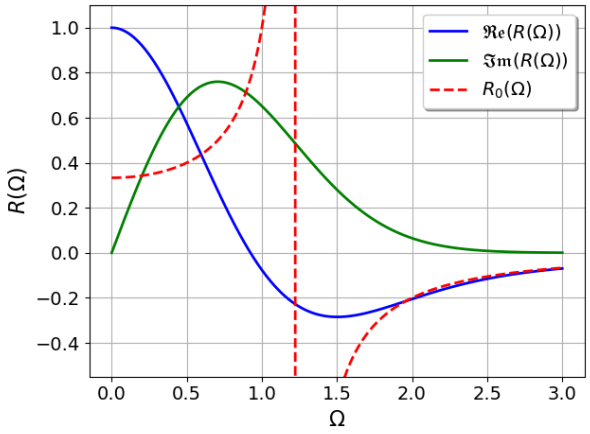

Figure 12: Response function of the fluid system with closure $\tilde{q} = 0$ in comparison to the kinetic response function

$$R_3(\Omega) = \frac{\chi - i\Omega}{2i\Omega^3 - 2\chi\Omega^2 - 3i\Omega + \chi}, \tag{79}$$

with $\chi = 2/\sqrt{\pi}$. This response function has now a real and an imaginary part. We compare the two closures in fig. 13 and observe this closure approximates the kinetic response fairly well over the whole domain and matches the limits exactly. Which is no surprise, since the closure was designed in this way.

We can extend the proposed three-moment fluid model by adding a dynamical equation for the heat flux, which is calculated by multiplying eq. (64) with v^3 and taking the integral over velocity space. The heat flux equation reads

$$\frac{\partial}{\partial t}q + \frac{\partial}{\partial x}(uq) = -3q\frac{\partial}{\partial x}u + 3\frac{p}{mn}\frac{\partial}{\partial x}p - \frac{\partial}{\partial x}r, \tag{80}$$

with $r \equiv m\int(v-u)^4 f \, \mathrm{d}v \equiv 3p^2/(mn) + \delta r$ the next higher fluid moment after q. Hammett and Perkins have also proposed a closure term for the four-moment model

$$\delta\tilde{r} = -D\frac{\sqrt{2}v_{\mathrm{th}0}}{|k|}ik\tilde{q}_k + \beta n_0 2v_{\mathrm{th}0}^2\tilde{T}_k, \tag{81}$$

with $D = 2\sqrt{\pi}/(3\pi - 8)$ and $\beta = (32 - 9\pi)/(6\pi - 16)$. We can repeat the calculation we did for the three-moment model also for the four-moment model, which is a bit more tedious, but otherwise very similar. The response function

$$R_4(\Omega) = \frac{3 + 2\beta - 2iD\Omega - 2\Omega^2}{3 + 2\beta - 6iD\Omega - (12 + 4\beta)\Omega^2 + 4iD\Omega^3 + 4\Omega^4} \tag{82}$$

has a more complex form than in the three-moment case. By comparing the response of the four-moment model to the kinetic response in fig. 13 we find that this closure is an excellent approximation of its kinetic counterpart.

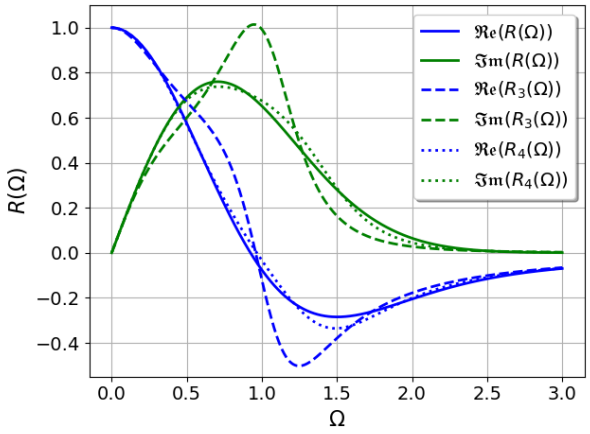

Figure 13: Response function of the fluid system with the four-moment Hammett-Perkins closure in comparison to the kinetic response function and one of the three-moment Hammett-Perkins closure

Response function for the Braginskii closure

We can do the same exercise for the Braginskii closure eq. (60), where we find in the end a response function that can be written in the same form as the response function of the Hammett-Perkins closure eq. (79), but the parameter χ takes a different form

$$\chi = 3.16 v_{\mathrm{th}0} \tau_{i0} |k| / \sqrt{2} \tag{83}$$

and is dependent on k and the background temperature, therefore every scale k behaves differently. By accident, for one single k the Braginskii closure can even match the response of the Hammett-Perkins closure if $\chi = 2/\sqrt{\pi}$. We plot the response function of the Braginskii model in fig. 14 for $T_0 = 100\,\mathrm{eV}$, $n_0 = 10^{20}\,\mathrm{m}^{-3}$ and with $k = 1/(qR_0) = 1/(6.6\,\mathrm{m})$. Here the Braginskii closure is not off by orders of magnitude, which is the case for different temperatures and values of k.

2.2.7 Remark on the form of the Hammett-Perkins closure

The form of the Hammett-Perkins closure with its dependency on $ik/|k|$ seems a bit puzzling at first. With the help of the previous chapters, we can find an explanation now, why this form of the closure is necessary. We saw that the important parameter for the kinetic response function is $\Omega = \omega/(2^{1/2} v_{\mathrm{th}0}|k|) = 2^{-1/2} v_{\mathrm{ph}}/v_{\mathrm{th}0}$. In the derivation of the response function of the Braginskii closure with its dependency on ik we saw that in the response function a dependency on $|k|$ remained. This implies that the only way of designing a fluid closure, which is independent of k, as the exact kinetic response function, is by choosing a closure of the form $ik/|k|$.

2.2.8 Non-locality of the Hammett-Perkins closure

We want to see what form the Hammett-Perkins closure takes in configuration space. Therefore we have to transform it from k-space into configuration space via an inverse

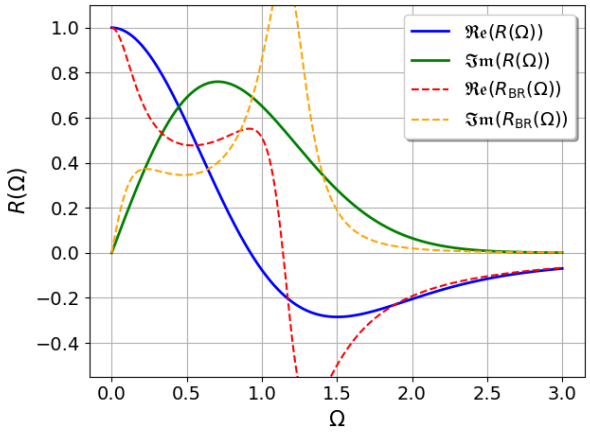

Figure 14: Response function of the fluid system with the Braginskii closure in comparison to the kinetic response function

Fourier transformation. We use the definition of the Fourier transform and apply it to the eq. (88) to calculate

$$\begin{aligned}\tilde{q}(x) = \mathscr{F}^{-1}\left(\tilde{q}(k)\right) &= \frac{1}{\sqrt{2\pi}}\int_{-\infty}^{\infty}\exp(ikx)\tilde{q}_k\,\mathrm{d}k \\ &= \frac{1}{\sqrt{2\pi}}\int_{-\infty}^{\infty}\exp(ikx)\left(-n_0 v_{\mathrm{th}0,j}\sqrt{8/\pi}\frac{ik}{|k|}\tilde{T}_k\right)\,\mathrm{d}k \\ &= -\frac{n_0 v_{\mathrm{th}0}\sqrt{8/\pi}}{\sqrt{\pi}}\int_{-\infty}^{\infty}\exp(ikx)\frac{ik}{|k|}\tilde{T}_k\,\mathrm{d}k,\end{aligned} \tag{84}$$

wherein we define the two functions $F_k(k) = ik/|k|$ and $G_k(k) = \tilde{T}_k$. The Fourier transforms of the functions $F_k(k)$ and $G_k(k)$ are

$$F(x) = \mathscr{F}^{-1}\left(F_k(k)\right) = \frac{1}{\sqrt{2\pi}}\int_{-\infty}^{\infty}\exp(ikx)\frac{ik}{|k|}\,\mathrm{d}k = -\sqrt{\frac{2}{\pi}}\frac{1}{x}, \tag{85}$$

$$G(x) = \mathscr{F}^{-1}\left(G_k(k)\right) = \frac{1}{\sqrt{2\pi}}\int_{-\infty}^{\infty}\exp(ikx)\tilde{T}_k\,\mathrm{d}k = \tilde{T}(x), \tag{86}$$

where we want to note that a small trick is needed to perform the Fourier transform of F_k, i.e. we have to add $\lim(\varepsilon \to 0)\exp(-|k|x)$ to make the boundaries at ∞ and $-\infty$ well defined. Employing the convolution theorem and the two Fourier transformed functions $F(x)$ and $G(x)$, we can transform the complete expression as

$$\begin{aligned}\tilde{q}(x) &= -\frac{2\sqrt{2}n_0 v_{\mathrm{th}0}}{\pi}\mathscr{F}\left[F_k(k)G_k(k)\right] \\ &= -\frac{2\sqrt{2}n_0 v_{\mathrm{th}0}}{\pi}\int_{-\infty}^{\infty} F(x')G(x-x')\mathrm{d}x' \\ &= -\frac{2\sqrt{2}n_0 v_{\mathrm{th}0}}{\pi}\int_{-\infty}^{\infty}\left(-\sqrt{\frac{2}{\pi}}\frac{1}{x'}\right)\tilde{T}(x-x')\mathrm{d}x' \\ &= -\frac{4n_0 v_{\mathrm{th}0}}{\pi^{3/2}}\int_0^{\infty}\frac{\tilde{T}(x+x')-\tilde{T}(x-x')}{x'}\mathrm{d}x',\end{aligned} \tag{87}$$

where we find that, unlike the Braginskii heat flux, which is driven by local temperature gradients, the Hammett-Perkins heat flux is driven by an average non-local temperature difference. This non-local behaviour is interesting and cumbersome at the same time since the implementation of this integral equation into a fluid turbulence code would hold many challenges. Luckily we do not want to implement exactly this equation but an extended version of it, which is introduced in the following.

2.2.9 The step from δf to full-f

During this section, all investigations were performed in a δf model, where we split all quantities in background quantities f_0 and perturbed quantities $\delta f = \tilde{f}$. In fluid turbulence simulations of the edge region of fusion devices fluctuation amplitudes can be quite large, therefore a δf-splitting is not possible and so-called full-f models are used, where the quantities are not divided in background plus perturbation. A fundamental question that arises is how to translate the Hammett-Perkins closure into a full-f picture and if this form of the closure is valid. The translation is done in a pragmatic and straightforward way

$$\tilde{q}^{\mathrm{HP}}_{\parallel\alpha,k} = -n_0 v_{\mathrm{th}0,\alpha}\frac{ik_\parallel}{|k_\parallel|}\tilde{T}_{\alpha,k} \quad \rightarrow \quad q^{\mathrm{HP}}_{\parallel\alpha,k} = -n v_{\mathrm{th},\alpha}\frac{ik_\parallel}{|k_\parallel|}T_{\alpha,k}, \tag{88}$$

where we exchange the background quantities with the full quantities $f_0 \approx f$ and for the perturbed temperature as well, since this term translates to a spatial derivative in real space, i.e. gives just a contribution for a non-constant (perturbed) temperature. This transformation is valid for the assumption of small fluctuation amplitudes. To address the question of validity we have to check the assumption of small fluctuations. In the following section, the Landau-fluid model is introduced, in which the Hammett-Perkins closure is the limiting case for low collisionality. In the inner edge region of a fusion device, where the Hammett-Perkins limit might be reached, fluctuation amplitudes are usually of the order of a few per cent [67, 68], therefore the assumption of small fluctuations is valid for usual operational regimes.

2.2.10 Landau-fluid closure

The Hammett-Perkins closure is derived for collisionless regimes. However, this is not the case in the edge region of a fusion device. There are still regions which are very

collisional. Therefore we would like to combine the two closures and use each one in the regime of its validity. This combination was done by Umansky et al. [44], who extended the Hammett-Perkins closure from collisionless to arbitrary collisionality as suggested by Snyder et al. [69] and Beer et al. [70]. This closure will be referred to as Landau-fluid closure and it takes the form

$$q_{\parallel\alpha,k}^{\mathrm{LF}} = -A\frac{ik_\parallel}{|k_\parallel| + \delta_\alpha/\lambda_{\mathrm{mfp}}} T_{\alpha,k}, \tag{89}$$

with the mean free path $\lambda_{\mathrm{mfp}} = v_{\mathrm{th},\alpha}\tau_\alpha$ and $\delta_e \approx 0.5$ and $\delta_i \approx 0.41$ as constants to reproduce the Braginskii closure for electrons and ions in the limit of high collisionality. To perform an analytical comparison between the different heat flux closures we rewrite them in terms of the parameter $\lambda_{\mathrm{mfp}}k_\parallel$. The comparison is performed for electrons and the index for species is again omitted. For the Braginskii closure, we find

$$\begin{aligned} q_{\parallel k}^{BR} &= -3.16 n v_{\mathrm{th}}^2 \tau i k_\parallel T_k = -3.16 n v_{\mathrm{th}} \lambda_{\mathrm{mfp}} i k_\parallel T_k \\ \frac{i q_{\parallel k}^{BR}}{n v_{\mathrm{th}} T_k} &= 3.16 \left(\lambda_{\mathrm{mfp}} k_\parallel\right), \end{aligned} \tag{90}$$

which is the Braginskii heat flux divided by the thermal free streaming heat flux times the imaginary unit. Note that the Braginskii closure scales linearly in $\lambda_{\mathrm{mfp}}k_\parallel$. For the Hammett-Perkins closure, we find

$$\begin{aligned} q_{\parallel k}^{HP} &= -n v_{\mathrm{th}} \sqrt{8/\pi} \frac{i k_\parallel}{|k_\parallel|} T_k \\ \frac{i q_{\parallel k}^{HP}}{n v_{\mathrm{th}} T_k} &= \sqrt{8/\pi} \frac{k_\parallel}{|k_\parallel|} = \sqrt{8/\pi} \quad (\text{for } k_\parallel > 0), \end{aligned} \tag{91}$$

which is independent of $\lambda_{\mathrm{mfp}}k$ for the same normalisation. For the Landau-fluid closure, we obtain

$$\begin{aligned} q_{\parallel k}^{LF} &= -n v_{\mathrm{th}} \sqrt{8/\pi} \frac{i k_\parallel}{|k_\parallel| + \delta/\lambda_{\mathrm{mfp}}} T_k \\ \frac{i q_{\parallel k}^{LF}}{n v_{\mathrm{th}} T_k} &= \sqrt{8/\pi} \frac{\left(\lambda_{mfp} k_\parallel\right)}{\left(\lambda_{mfp} k_\parallel\right) + 0.5} \quad (\text{for } k_\parallel > 0), \end{aligned} \tag{92}$$

wherein we find the two limiting cases with the Braginskii closure for $\lambda_{\mathrm{mfp}}k_\parallel \to 0$ and the Hammett-Perkins closure for $\lambda_{\mathrm{mfp}}k_\parallel \to \infty$. To visualise this behaviour in an example with practical relevance, we set $k_\parallel = (q_{95}R_0)^{-1}$ with typical values for the edge region of the ASDEX Upgrade tokamak with $q_{95} = 4$ and $R_0 = 1.65\,\mathrm{m}$. Therefore we can express

$$\lambda_{\mathrm{mfp}}k_\parallel = v_{\mathrm{th}}\tau_e \left(q_{95}R_0\right)^{-1} \approx 1.46 \cdot 10^{-4}\, T^2 \tag{93}$$

just in terms of the electron temperature. In fig. 15 we compare the heat fluxes proposed by the Braginskii, Hammett-Perkins and Landau-fluid closure, normalized to the

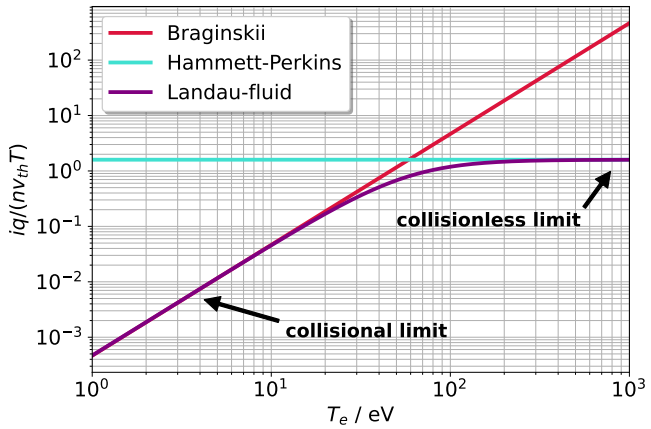

Figure 15: Magnitude of the heat-flux closures for electrons at fixed $k_\parallel = (q_{95}R_0)^{-1} = (6.6\,\mathrm{m})^{-1}$ which is a typical value for ASDEX Upgrade, $n = 10^{19}\,\mathrm{m}^{-3}$ and constant coulomb logarithm of $\lambda = 15$

thermal heat flux. We observe the magnitude of the Braginskii heat flux steadily growing with decreasing collisionality and the Hammett-Perkins heat flux being independent of collisionality. The latter is reasonable since the Hammett-Perkins closure was derived for a collisionless system. The Landau-fluid closure recovers for high collisionality the Braginskii closure and for low collisionality the Hammett-Perkins closure which can be seen in fig. 15 as well. The fact that the Landau-fluid closure predicts a lower magnitude heat flux in the intermediate collisional regime compared with the other two closures is also recovered with a more elaborate kinetic Landau-fluid closure [71]. The Landau-fluid model is probably valid for the collisional SOL, where it approaches the Braginskii limit. At the inner edge region, where the Hammett-Perkins limit is reached, the model should retain its validity due to small fluctuation amplitudes, as already mentioned in section 2.2.9. However, there might exist intermediate regions or conditions that are outside the region of validity of the Landau-fluid model.

2.2.11 Transformation into configuration space

The Landau-fluid closure is formulated in Fourier space, see eq. (89). Since most edge turbulence fluid codes act in configuration space due to the complex geometry of current fusion devices, we have to transform the Landau-fluid closure into configuration space. A direct Fourier transformation of this equation results in a non-local integral over the whole configuration space (see eq. (87)), which is computationally not feasible during a turbulence simulation. A significantly more efficient method to translate eq. (89) into configuration space was proposed by Dimits et al.[72]. With this fast non-Fourier method the original equation is approximated with a sum of Lorentzian functions

$$-A\frac{ik_\parallel}{|k_\parallel| + \frac{\delta_\alpha}{\lambda_{\mathrm{mfp}}}}T_{\alpha,k} \approx -A\frac{\delta_\alpha}{\lambda_{\mathrm{mfp}}}\sum_{n=1}^{N}\frac{\alpha_n}{k_\parallel^2 + \left(\frac{\delta_\alpha\,\beta_n}{\lambda_{\mathrm{mfp}}}\right)^2}ik_\parallel T_{\alpha,k}, \tag{94}$$

where α_n and β_n are fixed numerical constants that arise from the fit of the Lorentzian functions to the original equation and are visualised in fig. 16a. The transformation of the Hammett-Perkins closure can be done similarly and is shown in appendix B.

By plotting the single Lorentzians fig. 16b we find that with decreasing collisionality the higher-numbered Lorentzians become more important. The value of α_n and β_n are taken from Chen et al. [46] for the cases of $N \in \{3, 7, 12\}$, with N the number of Lorentzian functions. We use the same numbers for N later in the implementation of the model. The value of α_n and β_n are also shown in table 1. We performed the fit to obtain these parameters ourselves and compared them to the data in [46] in appendix C.

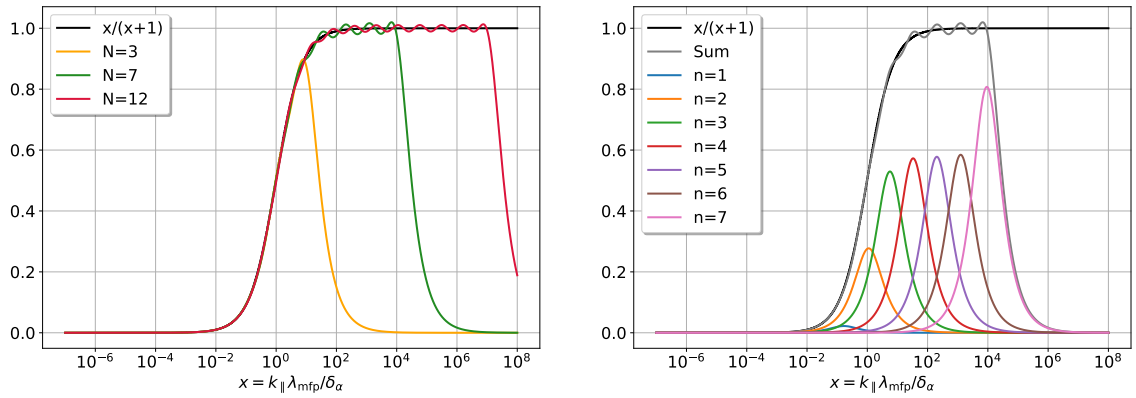

(a) Sum of Lorentz functions for $N \in \{3, 7, 12\}$ (b) Single Lorentz functions n for $N = 7$

Figure 16: Approximation of the Lorentzian functions to the function $f(x) = x/(x+1)$ with $x = k_\parallel \lambda_{\mathrm{mfp}}/\delta_\alpha$ which corresponds to eq. (94) (adapted from Zhu et al. [49])

	$N = 3$		$N = 7$		$N = 12$	
n	α_n	β_n	α_n	β_n	α_n	β_n
1	0.01315	0.2044	0.007438	0.1678	0.001424	0.09419
2	0.924	1.3587	0.6161	1.1106	0.20736	0.6741
3	14.1365	8.9643	5.9804	5.6457	2.5653	2.9628
4			37.9822	33.1536	14.927	14.43958
5			234.3654	202.738	79.305	75.1106
6			1466.4331	1254.2144	419.2399	395.8293
7			14981.4634	9275.3323	2215.7233	2090.8877
8					11709.7857	11049.1471
9					61885.2763	58392.0969
10					327392.6096	308695.7371
11					1773350.1566	1645460.1472
12					16903628.3745	10794779.4293

Table 1: Numerical values of α_n and β_n as found in Chen et al. [46]

A rough estimate for the minimum number of Lorentzians needed for a simulation can be done by calculating x from fig. 16a with provided values for $k_\parallel$ and λ_{mfp}. For electrons in our simulation of ASDEX Upgrade in a later chapter, we estimate $k_\parallel = (q_{95} R_0)^{-1} =$

$(6.6\,\mathrm{m})^{-1}$ via the inverse parallel connection length, $n(\rho_{\mathrm{pol}} = 0.91) = 2.0 \times 10^{-19}\,\mathrm{m}^{-3}$ and $T_e(\rho_{\mathrm{pol}} = 0.91) = 350\,\mathrm{eV}$ taken at the core boundary a value of $x \approx 18$, therefore we can conclude from fig. 16a that $N = 7$ should be sufficient. For ions, we find that 7 Lorentzians are fine as well. The single Lorentzian functions can be easily translated back into configuration space which leads to a set of decoupled elliptic equations

$$\left[-\nabla_\parallel^2 + \left(\frac{\delta_\alpha\,\beta_n}{\lambda_{\mathrm{mfp}}}\right)^2\right] q^{\mathrm{LF}}_{\parallel\alpha,n} = -A\frac{\delta_\alpha}{\lambda_{\mathrm{mfp}}}\alpha_n \nabla_\parallel T_\alpha, \tag{95}$$

that has to be solved along field lines for every n. The total heat flux is then the sum $q^{\mathrm{LF}}_{\parallel\alpha} = \sum_n q^{\mathrm{LF}}_{\parallel\alpha,n}$. The computational cost of the method is thus optimal at higher collisionality, where only a few Lorentzians are required.

2.3 Drift reduced fluid equations

This part is based on [73].

Until now no restrictions on the fluid equations have been imposed, which means dynamics of all timescales are still present, ranging from the electron cyclotron frequency $\omega_{ce} \approx 10^{11}\,1/\mathrm{s}$ (for $B \approx 1\,\mathrm{T}$) and ion cyclotron frequency $\omega_{ci} \approx 10^{8}\,1/\mathrm{s}$ over the typical time scale of turbulent fluctuations of the order of μs up to confinement time scales of the order of s. Since we are interested in the relatively slow turbulence of the order of μs it is important to eliminate the fast time scales. The ordering which is used for the drift reduction consists of three assumptions

$$\omega \sim \frac{\partial}{\partial t} \ll \omega_{ci}, \qquad k_\parallel \ll k_\perp, \qquad k_\perp \gg \frac{\nabla B}{B}, \tag{96}$$

where the first means the considered time scales ω are slow in comparison to the ion gyro frequency. The second assumption states that turbulent structures are elongated along field lines, this approximation is called 'flute-mode' approximation and is robustly valid in magnetised plasmas [9]. The flute-mode approximation implies that parallel and perpendicular dynamics are strongly separated. The third assumption says that the perpendicular turbulent scales are much smaller than the length scale over which the magnetic field changes. With this ordering we can derive 'drift-reduced' equations, starting from the fluid equations obtained by taking moments over the kinetic equation eqs. (15) to (17). They are called drift-reduced since effectively we are splitting the dynamics into the fast gyro-motion and the slow drifts, with the application of the ordering eq. (96) we eliminate the fast gyro-motion and we are left with the drift-velocities. As explained in [74], the electric field within the drift approximation is given by

$$\boldsymbol{E} = -\nabla\phi - \frac{\partial}{\partial t} A_\parallel, \tag{97}$$

which means the electric field is electrostatic in perpendicular and electromagnetic in parallel direction. We begin with the momentum equation eq. (16) and take the perpendicular component of it by applying $\boldsymbol{B}/B^2\times$ to the equation. We find for the perpendicular velocities

$$\begin{aligned}\boldsymbol{v}_{e\perp} &= \frac{\boldsymbol{B}\times\nabla\phi}{B^2} - \frac{\boldsymbol{B}\times\nabla p_e}{enB^2} - \frac{1}{\omega_{ce}}\boldsymbol{b}\times\frac{\mathrm{d}_e}{\mathrm{d}t}\boldsymbol{v}_e \\ &= \boldsymbol{v}_{ExB} + \boldsymbol{v}^e_{dia} + \mathcal{O}\left(\frac{\mathrm{d}_e/\mathrm{d}t}{\omega_{ce}}\right),\end{aligned} \tag{98}$$

$$\begin{aligned}\boldsymbol{v}_{i\perp} &= \frac{\boldsymbol{B}\times\nabla\phi}{B^2} + \frac{\boldsymbol{B}\times\nabla p_i}{enB^2} + \frac{1}{\omega_{ci}}\boldsymbol{b}\times\frac{\mathrm{d}_i}{\mathrm{d}t}\boldsymbol{v}_i + \frac{c}{enB^2}\boldsymbol{B}\times\nabla\cdot P_i \\ &= \boldsymbol{v}_{ExB} + \boldsymbol{v}^i_{dia} + \boldsymbol{u}_{pol} + \mathcal{O}\left(\frac{\mathrm{d}_i/\mathrm{d}t}{\omega_{ci}}\right)^2,\end{aligned} \tag{99}$$

with the polarisation velocity

$$\boldsymbol{u}_{pol} = -\frac{M_i}{eB^2}\left[\frac{\partial}{\partial t} + \left(u_\parallel\hat{\boldsymbol{b}} + \boldsymbol{v}_{ExB}\right)\cdot\nabla\right]\left(\nabla_\perp\phi + \frac{1}{en}\nabla_\perp p_i\right) + \frac{\hat{\boldsymbol{b}}}{enB}\times\nabla\cdot\tilde{\boldsymbol{\Pi}}_i, \tag{100}$$

which is one order $\mathcal{O}((\mathrm{d}_i/\mathrm{d}t)/\Omega_i)$ smaller than the other velocities, although its divergence is of the same order. Therefore the polarisation velocity is neglected, unless it appears under a divergence.

We will not do the full derivation of all drift-reduced equations necessary for our plasma model here, where we would obtain a continuity equation, quasineutrality equation, an equation for momentum balance and Ohm's law, an electron and ion temperature equation and an equation for Ampére's law. For this full derivation, we refer to [73]. However, as an example, we will derive the drift-reduced electron temperature equation from eq. (17). In the first step, we note that the electron stress tensor $\boldsymbol{\Pi}_e$ is about a factor $(m_e/m_i)^{1/2}$ smaller than the ion stress tensor, therefore it is neglected. We find

$$\begin{aligned}\frac{3}{2}n\left[\frac{\partial}{\partial t} + \boldsymbol{v}_e\cdot\nabla\right]T_e &= -p_e\nabla\cdot\boldsymbol{v}_e - \nabla\cdot\boldsymbol{q}_e - \boldsymbol{\Pi}_e\otimes\nabla\boldsymbol{v}_e + (Q_e - Q_\Delta) \\ \frac{3}{2}n\left[\frac{\partial}{\partial t} + \boldsymbol{v}_{ExB} + \boldsymbol{v}^e_{dia}\cdot\nabla + v_\parallel\nabla_\parallel\right]T_e &= -p_e\nabla\cdot\left(v_\parallel\hat{\boldsymbol{b}} + \boldsymbol{v}_{ExB} + \boldsymbol{v}^e_{dia}\right) - \nabla\cdot\boldsymbol{q}_e + (Q_e - Q_\Delta).\end{aligned} \tag{101}$$

We insert the full expression of the electron heat flux

$$\boldsymbol{q}_e = \boldsymbol{q}_\parallel - \frac{5}{2}\frac{p_e}{eB}\hat{\boldsymbol{b}}\times\nabla T_e - 0.71\frac{T_e}{e}j_\parallel\hat{\boldsymbol{b}} \tag{102}$$

and the terms for the frictional ohmic heating for electrons $Q_e = \eta_\parallel j_\parallel^2 - 0.71(j_\parallel/e)\nabla_\parallel T_e$ and the heat exchange $Q_\Delta = 3nm_e(T_e - T_i)/(M_i\tau_e)$. The diamagnetic velocity in the advective derivative cancels with the second term of the electron heat flux in eq. (102), which is known as diamagnetic cancellation. After inserting all the terms and a few lines of algebra we arrive at the drift-reduced electron temperature equation

$$\begin{aligned}\frac{3}{2}n\left[\frac{\partial}{\partial t}+\boldsymbol{u}_{ExB}\cdot\nabla+v_{\parallel}\nabla_{\parallel}\right]T_e=&-T_e\left(\nabla\times\frac{\hat{\boldsymbol{b}}}{B}\right)\cdot\nabla\phi-\frac{T_e}{n}\left(\nabla\times\frac{\hat{\boldsymbol{b}}}{B}\right)\cdot\nabla p_e\\&-T_e\nabla\cdot\left(v_{\parallel}\hat{\boldsymbol{b}}\right)+\frac{1}{n}\nabla\cdot\boldsymbol{q}_{\parallel}+\frac{5}{2}\frac{T_e}{e}\left(\nabla\times\frac{\hat{\boldsymbol{b}}}{B}\right)\cdot\nabla T_e\\&+0.71\frac{T_e}{en}\nabla\cdot j_{\parallel}\hat{\boldsymbol{b}}+\frac{1}{n}\eta_{\parallel}j_{\parallel}^2-\frac{3m_e}{M_i}\frac{(T_e-T_i)}{\tau_e}.\end{aligned}\tag{103}$$

The same procedure can be applied to all other equations to obtain their drift-reduced form. To obtain the ion temperature equation is a bit more intricate since one has to deal with the ion stress tensor, however, for an extended derivation we refer once more to [73]. The important message for this thesis is that the closure assumption on $\boldsymbol{q}_{\parallel}$ is not changed by the drift-reduction as we can see in eq. (103).

2.4 Chapter summary

Within this chapter, we derived plasma fluid equations and showed, why closure approximations are necessary for fluid models to become applicable. For the Braginskii closure, we derived its dependencies employing random walk estimates. Furthermore, we derived the exact closure for a plasma under the Lorentz approximation, i.e. infinitely heavy ions. The Braginskii closure for hydrogen was stated and an explanation, of why the closure for $q_{\parallel}$ is the most fragile part for low collisionality, was given. Flux limiters were introduced as a simple way to extend the validity into the direction of low collisionality. The Hammett-Perkins closure was introduced and the motivation for including linear Landau-damping into a fluid model via this closure was explained with the help of response functions. Response functions of different closures were calculated and compared. Finally, the Landau fluid was presented as a more sophisticated extension of the Braginskii closure for low collisionality. The Landau fluid closure corresponds for the limiting case of high collisionality to the Braginskii closure and for the limiting case of high collisionality to the Hammett-Perkins closure. Finally, it was shown how to transform the Landau fluid closure elegantly into configuration space and that it is unaffected by the drift reduction.

3 One-dimensional toy model

Parts of this chapter are reproduced from C. Pitzal, A. Stegmeir, W. Zholobenko, K. Zhang, and F. Jenko, "Landau-fluid simulations of edge-SOL turbulence with GRILLIX," Physics of Plasmas, vol. 30, no. 12, 2023., with the permission of AIP Publishing.

In this chapter, we want to investigate the behaviour of the presented fluid closures for the parallel conductive heat flux in a simple environment, yet one that offers new insights. Therefore we use a 1D toy model, that represents the parallel direction. In this toy model, we prescribe a temperature and optionally a density profile and calculate the heat fluxes predicted by the different closures. We will investigate the Braginskii, Hammett-Perkins and Landau-fluid closure with respect to collisionality, different boundary conditions, the contributions of the single Lorentz functions and an example with a more advanced analytical profile. For the whole chapter, we only consider electrons, since the only difference in their treatment is to change a numerical parameter, therefore the index for species is omitted.

3.1 Implementation

Since in real geometry, the parallel heat flux is the one-dimensional quantity, a one-dimensional toy model should be well suited to describe and explore the most fundamental properties of these heat flux models. To perform tests in a simple environment, a small FORTRAN code was written to calculate the heat fluxes predicted by different heat-flux closures. The code works in a 1D geometry, where various boundary conditions and different solvers were tested, both simple iterative and direct solvers. First, we derive the normalized versions of eq. (60), eq. (88) and eq. (95). For the normalisation of this 1D model, we need to define a reference temperature T_0, a reference density n_0 and a reference length $L_\parallel$. We want to keep this toy problem already close to the application, which will be a GRILLIX simulation of the edge region of the ASDEX Upgrade Tokamak. Therefore typical ASDEX Upgrade edge parameters are used for the normalisation, i.e. $T_0 = 100\,\mathrm{eV}$, $n_0 = 1.0 \times 10^{19}\,\mathrm{m}^{-3}$ and $L_\parallel = q_{95} R_0 = 4 \cdot 1.65\,\mathrm{m} = 6.6\,\mathrm{m}$ the parallel connection length. We also calculate here (partly out of curiosity) the normalisation of the thermal velocities in m/s for electrons, since ions are not considered in this chapter. We find

$$v_{\mathrm{th},0} = \sqrt{\frac{T_0}{m_e}} \approx 4.1938 \times 10^6\,\mathrm{m/s} = 4193.8\,\mathrm{km/s}. \tag{104}$$

However, for the normalisation of the heat flux, we use the thermal free streaming heat flux $q_0 = T_0 v_{\mathrm{th},0} n_0$ and for the heat conductivity follows $\kappa_0 = L_\parallel v_{\mathrm{th},0} n_0$. We investigate the following equations along the parallel direction denoted by the normalised parallel coordinate x. The different heat fluxes take a simpler form in normalised quantities, we start with the Braginskii heat flux (eq. (60))

$$\hat{q}^{BR} = -\frac{\kappa^{BR}}{n_0 T_0 v_{\mathrm{th},0}} \nabla_\parallel T = -\frac{3.16\, n v_{\mathrm{th}}^2 \tau}{n_0 T_0 v_{\mathrm{th},0}} \nabla_\parallel T = -\frac{3.16\, v_{\mathrm{th},0} \tau_0}{L_\parallel}\, \hat{T}^{5/2}\, \frac{\partial \hat{T}}{\partial x}, \tag{105}$$

where quantities with a hat $\hat{f}$ are normalised ones. The Hammett-Perkins heat flux (eq. (88)) takes the form

$$\begin{aligned} \left[-\nabla_\parallel^2 + (k_0\alpha^n)^2\right] q_\parallel^n &= -n v_{\text{th}} \sqrt{8/\pi} k_0 \alpha^n \beta \, \nabla_\parallel T \\ \Leftrightarrow \left[-\frac{\partial^2}{\partial x^2} + (L_\parallel k_0 \alpha^n)^2\right] \hat{q}_\parallel^n &= -L_\parallel \sqrt{8/\pi} k_0 \alpha^n \beta \, \hat{n} \hat{T}^{1/2} \frac{\partial \hat{T}}{\partial x} \end{aligned} \tag{106}$$

in normalised units. And finally, the Landau-fluid heat flux (eq. (95)) becomes

$$\begin{aligned} \left[-\nabla_\parallel^2 + \frac{\delta^2}{\lambda_{\text{mfp}}^2}\beta_n^2\right] q_\parallel^n &= -n v_{\text{th}} \sqrt{8/\pi} \alpha_n \frac{\delta}{\lambda_{\text{mfp}}} \nabla_\parallel T \\ \Leftrightarrow \left[-\frac{\partial^2}{\partial x^2} + (\frac{\delta}{\lambda_{\text{mfp}}} L_\parallel \beta_n)^2\right] \hat{q}_\parallel^n &= -L_\parallel \sqrt{8/\pi} \alpha_n \frac{\delta}{\lambda_{\text{mfp}}} \hat{n} \hat{T}^{1/2} \frac{\partial \hat{T}}{\partial x} \\ \Leftrightarrow \left[-\frac{\partial^2}{\partial x^2} + \left(\frac{L_\parallel \delta \beta_n}{v_{\text{th},0}\tau_0}\right)^2 \left(\frac{\hat{n}}{\hat{T}^2}\right)^2\right] \hat{q}_\parallel^n &= -\frac{\sqrt{8/\pi}\alpha_n \delta}{v_{\text{th},0}\tau_0 L_\parallel} \left(\frac{\hat{n}^2}{\hat{T}^{3/2}}\right) \frac{\partial \hat{T}}{\partial x}. \end{aligned} \tag{107}$$

For this simple model, we already use a canonical and dual grid, which has half indices. This is done to mimic the numerical setup of GRILLIX, which will be explained in the following chapter. An illustration of the dual and canonical grids can be seen in fig. 17.

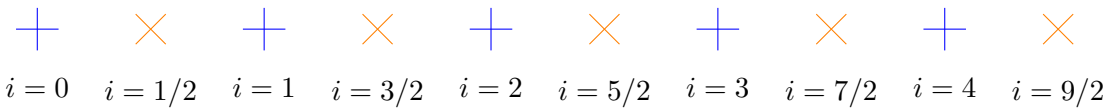

Figure 17: Canonical grid points in blue and dual ones in orange

Until further notice, we investigate a periodic system, which means in simple terms that the points $i = 9/2$ and $i = 0$ are connected in fig. 17 to close the loop. The blue points where the index is an integer belong to the canonical grid, while the orange points with half-integer indices form the dual grid. Within the discretisation, the temperature lives on the canonical grid, while the parallel heat flux lives on the dual grid. The discretisation of the first and second-order derivatives in eqs. (105) to (107) standard finite differences are used.

To solve the linear equation system of equations, that arises by discretising the elliptic equations for the Hammett-Perkins and the Landau-fluid heat flux, an iterative Jacobi and Gauss-Seidel algorithm [75] was implemented and additionally, a direct solver which employs the Thomas algorithm [76].

3.2 Dependency on collisionality

The very first point to investigate with our numerical tool is to calculate the Braginskii, Hammett-Perkins and Landau-fluid heat flux for a test case. The setup can be thought of as a temperature perturbation along a closed field line in the edge region of a fusion device. A temperature distribution of the form

$$\hat{T}(x) = 1 + 0.3 \exp(-x^2/\sigma) \tag{108}$$

is used, with $\sigma = 0.5\,\mathrm{m}/L_\parallel \approx 0.076$ and $T_0 \in \{3\,\mathrm{eV}, 30\,\mathrm{eV}, 300\,\mathrm{eV}\}$, which is shown in fig. 19a. Periodic boundary conditions are used here. For this investigation, we consider spatial distribution and magnitude of the heat fluxes separately, i.e. we normalise all heat fluxes to a peak value of 1 and plot their spatial distribution in fig. 19b, fig. 19c and fig. 19d. The magnitudes of the peak heat fluxes we used for the normalisation are visualised in fig. 18. The Landau-fluid closure behaves in this numerical one-dimensional experiment exactly as we would expect from theory. For low temperature $T_0 = 3\,\mathrm{eV}$, i.e. high collisionality, the Landau-fluid closure matches the Braginskii-closure in form (see fig. 19b) and in magnitude (see fig. 18). For high temperature $T_0 = 300\,\mathrm{eV}$, i.e. low collisionality, it matches the Hammett-Perkins-closure (see fig. 19d). For the case in between $T_0 = 30\,\mathrm{eV}$ the form of the Landau-fluid heat flux is in between the two other heat-flux closures and the magnitude is lower than the two other heat closures, which is in line with the theoretical behaviour in fig. 15.

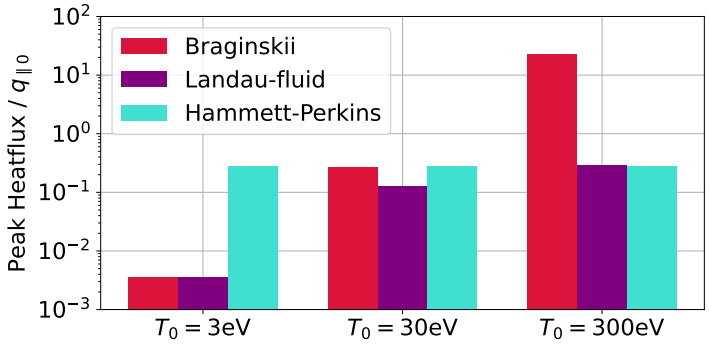

Figure 18: Magnitudes of the peak heat flux proposed by the Braginskii, Hammett-Perkins and Landau-fluid closure for three different values of T_0

Furthermore, we observe a non-locality in the Hammett-Perkins heat flux and the Landau-fluid one for low collisionality. By non-local we mean heat fluxes in regions where no local temperature gradient is present and a local heat flux model as the Braginskii closure would predict no heat flux, in fig. 19a this corresponds to $x > 0.3$. Here we confirm the observation of non-local behaviour as already reported in Chen et al. [46].

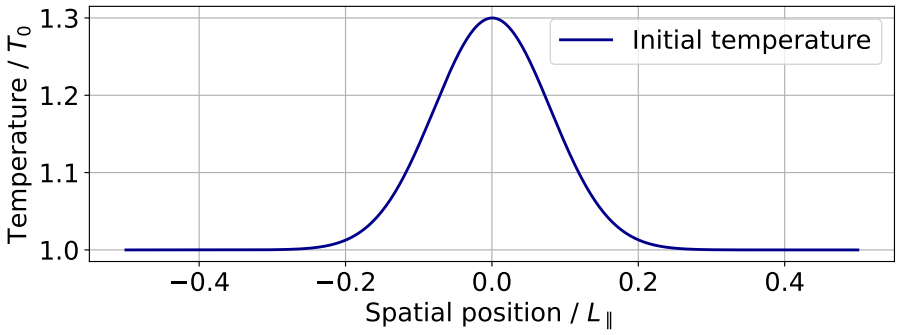

(a) Initial Gaussian temperature profile

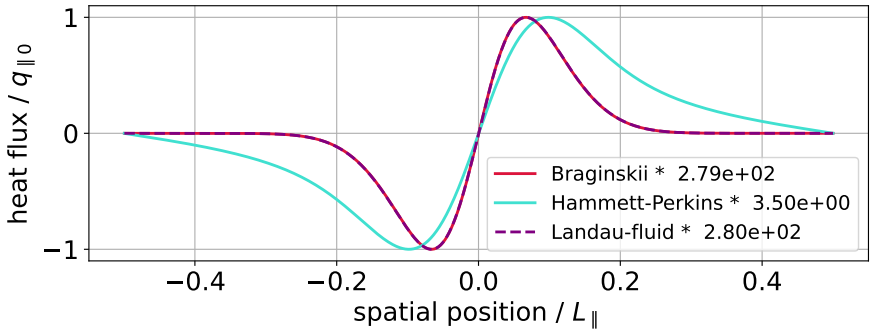

(b) Heat fluxes with $T_0 = 3\,\mathrm{eV}$

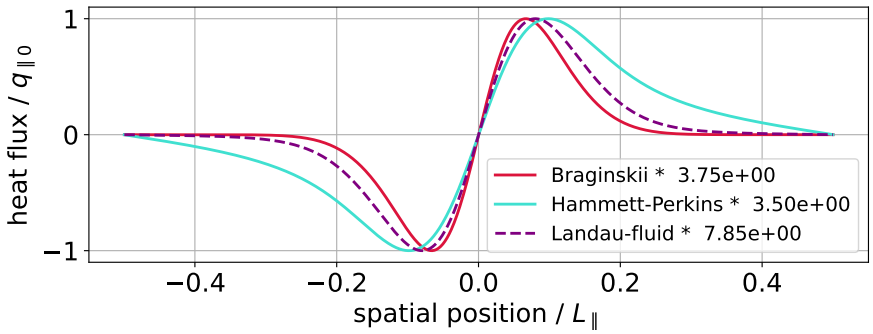

(c) Heat fluxes with $T_0 = 30\,\mathrm{eV}$

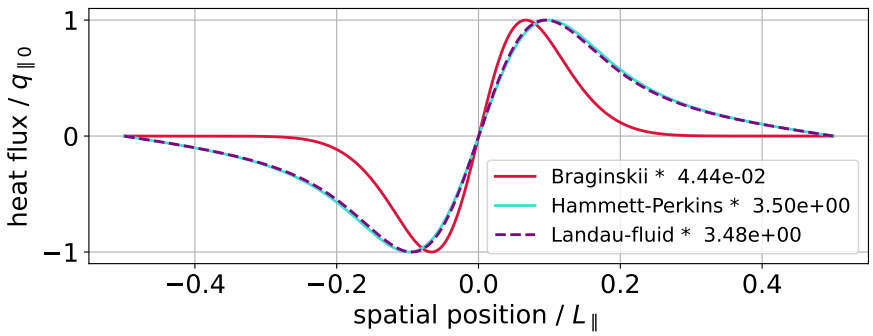

(d) Heat fluxes with $T_0 = 300\,\mathrm{eV}$

Figure 19: Initial temperature profile and normalised heat fluxes proposed by the Braginskii, Hammett-Perkins and Landau-fluid closure for different values T_0. Note the scaling of the heat fluxes in the legends, all are plotted with a maximum value of 1.0 to compare the spatial distribution

3.3 Boundary conditions

Different boundary conditions can be applied to the Landau-fluid heat flux within the system, namely periodic boundary conditions representing closed field lines in a fusion device and Dirichlet boundary conditions representing parallel boundary conditions at the intersection of open field lines with a limiter or divertor. Neumann boundary conditions would be possible, but since there is no physical motivation to apply them as parallel boundary conditions to the heat flux, they are not considered here.

How to set boundary conditions at the divertor targets is described in detail in [63]. There is no physical motivation for a boundary condition applied in the temperature directly. Due to considerations regarding the plasma sheath, there are so-called sheath boundary conditions. They can be applied to a fluid model and they contain an expression for the heat flux at the targets, which is

$$q^{\alpha}_{\parallel,\mathrm{bnd}} = \gamma_{\mathrm{sh},\alpha} n T_{\alpha} u_{\parallel}, \tag{109}$$

with $\gamma_{\mathrm{sh},\alpha}$ the sheath transmission coefficient and $u_{\parallel} = c_s$ reaches sound speed at the targets according to the Bohm criterion (see also [63]). The values of $\gamma_{\mathrm{sh},\alpha}$ are determined by the divertor material and its secondary electron emission coefficient. According to [63] and calculated for the ASDEX Upgrade tungsten divertor in [40], the relevant values are $\gamma_{\mathrm{sh},e} \approx 1.0$ and $\gamma_{\mathrm{sh},i} \approx 0$. To test Dirichlet boundary conditions with a finite value, corresponding to the boundary condition for the parallel electron heat flux, and with a value of zero, corresponding to the boundary condition for the parallel ion heat flux, we take the same setup as in section 3.2. Here we look just at the right half of the domain $x \in (0, 0.5)$. Two different temperatures are used $T_0 = 30\,\mathrm{eV}$ and $T_0 = 300\,\mathrm{eV}$. We investigate just the Landau-fluid closure since the Hammett-Perkins closure behaves nearly identically to the Landau-fluid case at $T_0 = 300\,\mathrm{eV}$. In fig. 20 the Landau-fluid heat fluxes are plotted with Dirichlet boundary conditions of $q_{\parallel,\mathrm{bnd}} = 0$ and $q_{\parallel,\mathrm{bnd}} = 0.1$ are plotted. The case with periodic boundary conditions matches the Dirichlet case $q_{\mathrm{bnd}} = 0$ exactly and is omitted therefore in fig. 20. Aside from the observation that the boundary value at $x = 0.5$ is approached smoothly by the model, we note that also the peak value of the heat flux around $x = 0.1$ is increased, which might play a role for heat fluxes in the scrape-off layer of a fusion device.

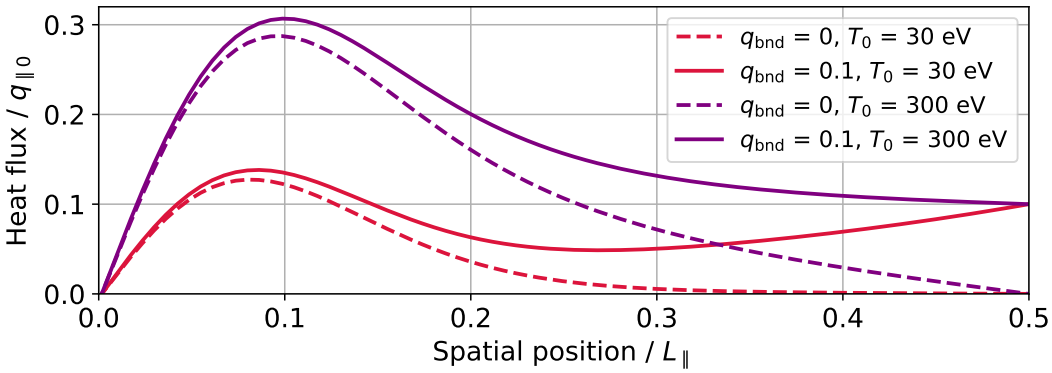

Figure 20: Dirichlet boundary conditions with different values q_{bnd} applied to the Landau-fluid closure for $T_0 = 30eV$ and $T_0 = 300eV$

Regarding the Braginskii closure, this sheath boundary condition has to be applied as a Neumann boundary condition on the temperature, since the heat flux is evaluated locally according to the gradient of temperature. Therefore strong parallel gradients in temperature have to build up near the targets to match the sheath boundary conditions. This is a major difference from the Landau-fluid closure, where temperature gradient and heat flux are decoupled. Neumann boundary conditions were not implemented into the 1D model, since they were not relevant for the Landau-fluid closure and this kind of boundary conditions were already implemented and used in GRILLIX. Therefore no plot for the Braginskii closure is added here.

3.4 Single Lorentz functions

The contributions of the single Lorentz functions are investigated. Therefore we use again the medium collisional case with $T_0 = 30\,\mathrm{eV}$ from section 3.2 since the magnitudes of all three models are comparable here and therefore the heat fluxes can be plotted without normalising them to $\max(q) = 1$ as we did in fig. 19. Additionally, we plot in fig. 21 the contribution of every single Lorentzian function. We observe that mainly the Lorentzians $n = 2$ and $n = 3$ contribute to the total heat flux. Furthermore, we note that the lower active Lorentzians are important for the non-local behaviour of the heat fluxes, here $n = 2$.

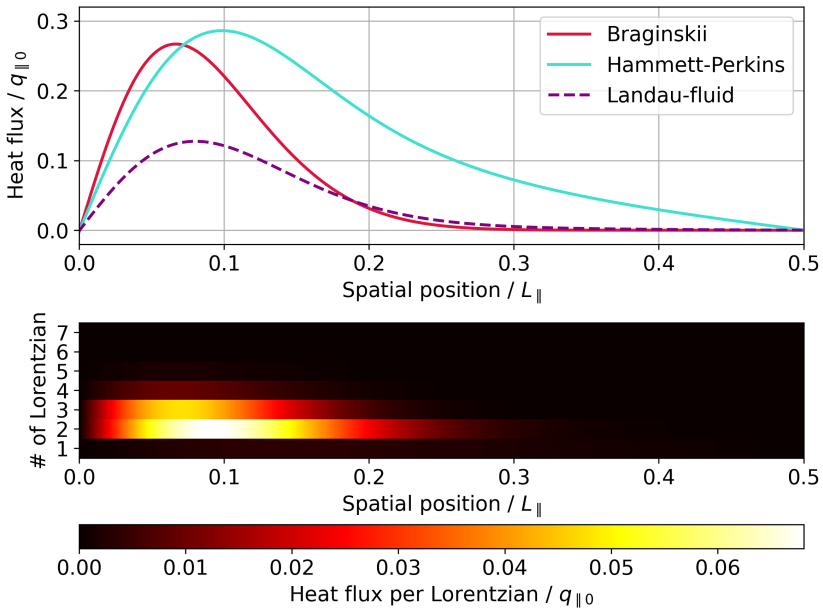

Figure 21: Heat fluxes and single Lorentzians of the Landau-fluid closure for $T_0 = 30eV$

What happens if we decrease the collisionality by increasing the temperature in our toy model? For this investigation, we just keep the Landau-fluid heat flux and use again the initial Gaussian temperature distribution from eq. (108) with the same value for σ and the values $T_0 \in \{30\,\mathrm{eV}, 300\,\mathrm{eV}, 1000\,\mathrm{eV}, 6000\,\mathrm{eV}\}$ for the background temperature. In fig. 22 the total heat flux predicted by the Landau-fluid closure plus the contribution of the single Lorentz functions are plotted. We observe that with increasing temperature (so decreasing collisionality) the higher-numbered Lorentzians carry the heat flux, which

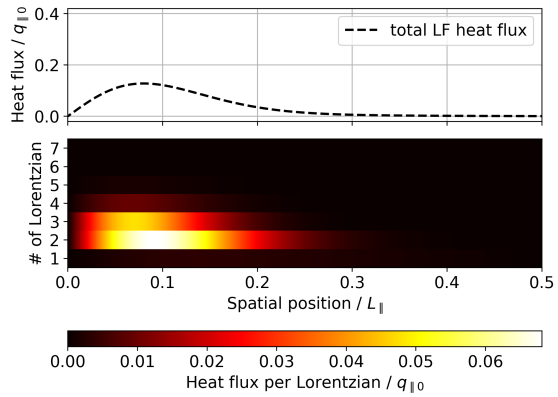

(a) Lorentz functions for $T_0 = 30\,\mathrm{eV}$

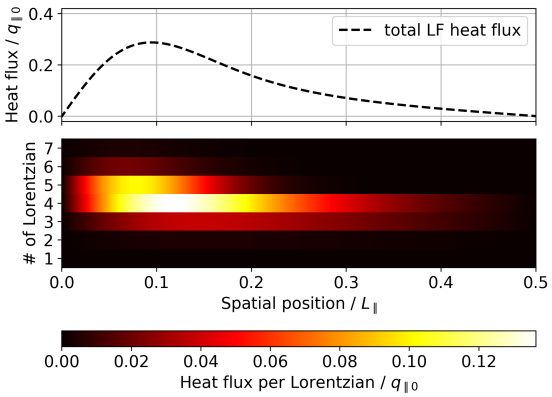

(b) Lorentz functions for $T_0 = 300\,\mathrm{eV}$

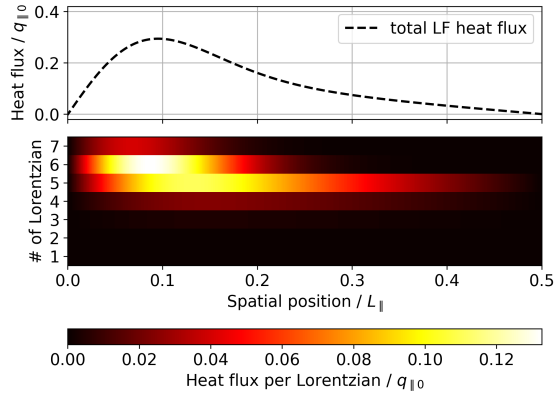

(c) Lorentz functions for $T_0 = 1000\,\mathrm{eV}$

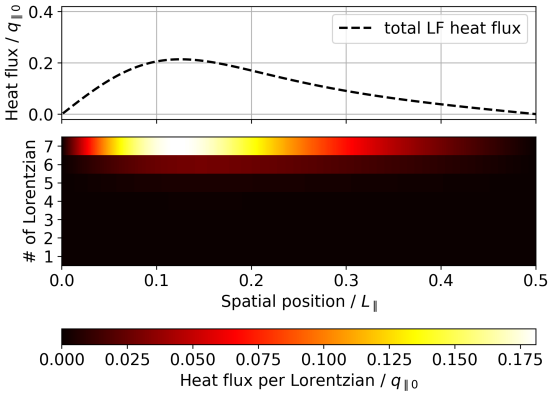

(d) Lorentz functions for $T_0 = 6000\,\mathrm{eV}$

Figure 22: Total Landau-fluid heat flux and the contribution of the different Lorentz functions for 4 different temperatures

is consistent with fig. 16b. The total heat flux increases from $T_0 = 30\,\mathrm{eV}$ to $T_0 = 300\,\mathrm{eV}$, but stays constant from $T_0 = 300\,\mathrm{eV}$ to $T_0 = 1000\,\mathrm{eV}$, which is in line what we already observed in fig. 18. With the last case $T_0 = 6000\,\mathrm{eV}$ we can observe what happens when the number of Lorentz functions is too little to describe this regime of collisionality adequately. The highest Lorentz function is reached, the total heat flux becomes less peaked and the magnitude of the total heat flux is underestimated. For even higher temperatures the magnitude of the heat flux becomes smaller and approaches a value of zero in the limit of infinitely high temperatures.

3.5 Examples with analytical initial conditions

Two examples are presented here to gain more intuition about how the Landau-fluid heat flux module behaves and reacts. The first case is kept close to the Gaussian temperature distribution, that was used already. The distribution is modified by adding a small perturbation on top

$$\hat{T}(x) = 1 + 0.3\exp(-x^2/\sigma) + 0.006\cos(50x), \tag{110}$$

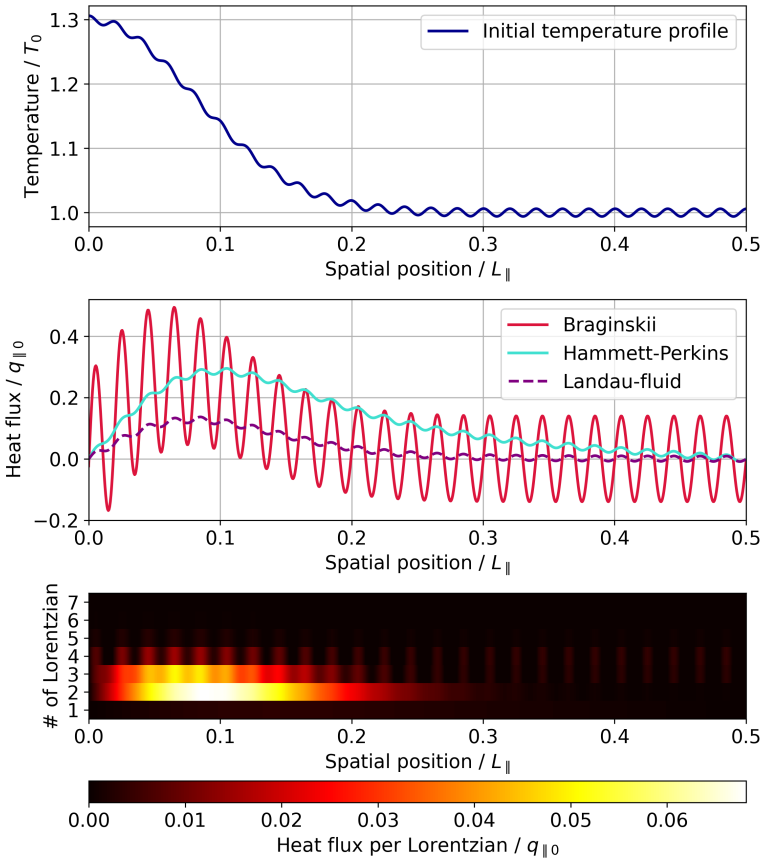

Figure 23: A modified initial state and the corresponding heat fluxes plus Lorentzians

with the form of a cosine function, which varies on smaller spatial scales than the Gaussian does. With this initial condition, we can mimic a perturbation that has different

components in the one-dimensional wave vector k. From fig. 16b one would assume that not only larger values of λ_{mfp} are carried by higher-numbered Lorentz functions, but also structures with a higher value in k, since the variable on the abscissa is $x = k_{\parallel}\lambda_{\mathrm{mfp}}/\delta_e$. This behaviour is also seen in fig. 23, where the structure with large k, so a small parallel wavelength is carried by Lorentz function with higher numbers in comparison to the larger structure arising from the Gaussian component. The Braginskii closure predicts significantly larger fluctuation amplitudes of the heat flux along the parallel direction, since here just the local temperature gradient plays a role. For the Landau-fluid and Hammett-Perkins closure, the heat fluxes are smoother due to the non-local effects, which can be thought of as a convolution from a mathematical point of view, as it was shown in section 2.2.8.

3.6 Chapter summary

Within this chapter, we explained how we set up a 1D model for testing the different fluid closures. A test with different values of collisionality was performed by varying the background temperature. All three closures behaved as expected from the theory section. We showed, that in this implemented 1D setup, the Landau fluid closure reproduces the Braginskii closure for high collisionality and the Hammett-Perkins closure for low collisionality, both in magnitude and spatial distribution. Furthermore, the Hammett-Perkins and the Landau-fluid closure predicted non-local heat fluxes. The application of Dirichlet boundary conditions necessary to imply sheath boundary conditions to the Landau fluid closure was successfully tested. Furthermore, the behaviour of the single Lorentz functions was examined for different values of collisionality. We saw that the heat flux is carried by higher-numbered Lorentzians with lower collisionality, while the lower-numbered active ones are responsible for the non-locality. We showed that for low values of collisionality, which are beyond the range of validity of the model, the heat flux is underestimated. Lastly, we observed that for a temperature distribution with small-scale and large-scale dependencies, the corresponding heat fluxes are carried by different Lorentzians, as they correspond to different values of the wave number k.

4 Implementation into the edge turbulence fluid code GRILLIX

This chapter is used for introducing the flux-coordinate-independent (FCI) approach, where we mainly follow [77, 48]. Special focus is put on the treatment of parallel operators, as they are important for the implementation of the Landau-fluid closure. The normalisation of GRILLIX is stated as well as the full normalised Landau-fluid equation, that is implemented into GRILLIX. We explain where magnetic flutter enters the Landau-fluid equation and how it is treated. The implementation is tested with the method of manufactured solutions and by comparing a test case to the one-dimensional toy model. A few simple tests utilising the geometric capability of GRILLIX for the Landau-fluid model are shown. Lastly, the numerical algorithm, which is used currently and alternatives that might be more efficient are discussed.

4.1 Discrete formulation

4.1.1 Flux-coordinate-independent approach

Modelling the edge region of magnetic confinement fusion devices entails the necessity of crossing the separatrix. Commonly used field-aligned coordinate systems, which have a large computational benefit due to exploiting the flute-mode character of turbulence, cannot be used here, since this coordinate system becomes singular at the separatrix. A method which enables simulations across the separatrix and still exploits the flute-mode character is the FCI approach. Herein the coordinate system consists of poloidal planes, which themselves are organised in an equidistant unstructured grid. The grid points of a plane are accessed via their indices in a one-dimensional array. In fig. 24a the index of each point is colour-coded to visualise the ordering of the unstructured grid. In between the planes, the magnetic field is traced until it intersects the following plane, where the intersection point is interpolated using the neighbouring grid points, as shown in fig. 24b. The discretization inside a poloidal plane is straightforward, since the grid is equidistant, it can be viewed for practical reasons as Cartesian.

The discretization along the parallel direction is more challenging. We explain briefly the key concepts for constructing parallel operators within the FCI approach, wherein we have to trace magnetic field lines along the parallel direction. A magnetic field line $\gamma(\varphi)$ with a starting point $\gamma(0)$ is parameterised in cylindrical coordinates $(x = R, \varphi = \varphi, y = Z)$ via

$$\dot{\gamma}(\varphi) = \begin{pmatrix} B_x/B_\varphi \\ 1 \\ B_y/B_\varphi \end{pmatrix} \qquad \text{with} \qquad \gamma(0) = \begin{pmatrix} x_0 \\ 0 \\ y_0 \end{pmatrix}, \tag{111}$$

with B_x, B_φ and B_y the components of the magnetic field in the corresponding directions. With the parameterisation we can find any point along the magnetic field line by performing the integral

$$\gamma(\varphi) = \gamma(0) + \int_0^\varphi \dot{\gamma}(\varphi')\,\mathrm{d}\varphi'. \tag{112}$$

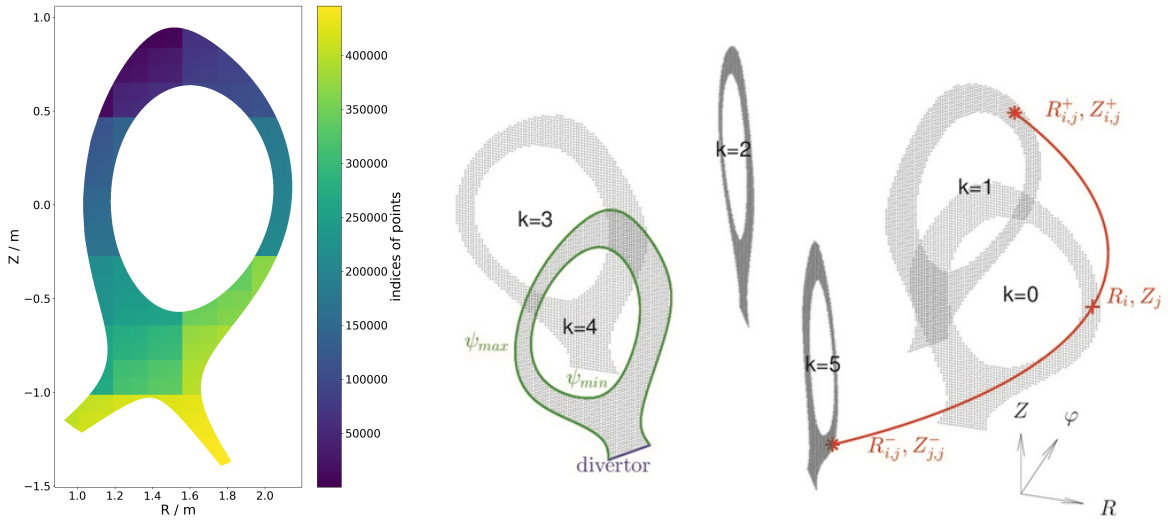

(a) Indices of points of the unstructured grid in a poloidal plane

(b) Field line tracing between planes, taken from [20]

Figure 24: Visualisation of the FCI approach

The arclength $s(\varphi)$ along the field line $\gamma(\varphi)$ is parameterised via

$$\dot{s}(\varphi) = \frac{|\boldsymbol{B}(\gamma(\varphi))|}{B_\varphi(\gamma(\varphi))} \qquad \text{with} \qquad s(0) = 0, \tag{113}$$

with $\boldsymbol{B}$ the total magnetic field. The value of s is determined by a similar integral as eq. (112). Suppose we start at a point $(x_0, 0, y_0)$ and follow the corresponding field line a toroidal distance of $\Delta\varphi$ until we intersect the following plane. We find the field line intersecting at the coordinates $\gamma(\Delta\varphi) = (x_P, \Delta\varphi, y_P)$. Since the points (x_P, y_P) on the following poloidal plane $k+1$ will most likely not coincide with a grid point, it is necessary to interpolate between the neighbouring grid points (x_i, y_i). For some variable u we use the notation $u(x_P, \Delta\varphi, y_P) = u_{k+1}(x_P, y_P)$ on one discrete plane. The interpolation can be written as

$$u_{k+1}(x_P, y_P) = \sum_i c_i u_{k+1}(x_i, y_i), \tag{114}$$

with c_i the interpolation coefficients and (x_i, y_i) the coordinates of a stencil of neighbouring points. By performing this task for every single grid point j an interpolation matrix $\boldsymbol{C}$ can be constructed and stored, which has the interpolation coefficients as entries $\boldsymbol{C}\big|_{ij} = c_{ij}$. With the help of these interpolation matrices, we are able to construct parallel operators. One major limitation of the FCI approach becomes apparent here, since the construction of the interpolation matrices is computationally expensive, a constant background magnetic field B_0 is favourable because the field line tracing has to be done once. For strong changes in the background magnetic field, however, the interpolation matrices would have to be updated regularly.

As we mentioned in the previous chapter for the parallel direction the grid implemented in GRILLIX consists of a canonical grid G with indices $k \in \{0, 1, 2, ...\}$ and a dual grid $G^\star$ with indices $k \in \{1/2, 3/2, 5/2, ...\}$. These grids are needed for the construction of

parallel operators according to the support operator method [78]. With this method of constructing parallel operators some conservation laws that hold true for the continuous formulation of equations can be maintained in the discrete formulation, for further details we refer to [78].

We focus now on the parallel gradient, which takes quantities from the canonical grid as input and computes quantities on the dual grid, and the parallel divergence, which works vice versa

$$\begin{aligned} \nabla_\parallel u \quad &: \quad G \;\Rightarrow\; G^\star, \\ \nabla\cdot(\boldsymbol{b}\,u) \quad &: \quad G^\star \;\Rightarrow\; G, \end{aligned} \tag{115}$$

with the parallel unit vector $\boldsymbol{b} = \boldsymbol{B}/B$. The calculation of the parallel gradient on the plane $k+1/2$ at the point (x_0, y_0) via a finite difference involves the intersection points (x_P^+, y_P^+) on the forward plane $k+1$ and (x_P^-, y_P^-) on the backward plane k. The parallel gradient reads in the standard form of a central finite difference

$$\left(\nabla_\parallel u\right)_{k+1/2}(x_0,y_0) = \frac{u_{k+1}(x_P^+, y_P^+) - u_k(x_P^-, y_P^-)}{s(\Delta\varphi/2) + s(-\Delta\varphi/2)}. \tag{116}$$

where the toroidal distance is $\Delta\varphi/2$ in forward and backward direction. A visualisation of the intersecting magnetic field lines is shown in fig. 25.

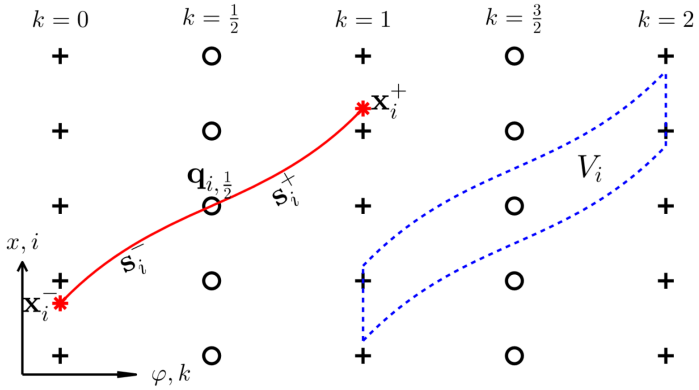

Figure 25: Visualisation of a magnetic field line intersecting neighbouring planes in the FCI approach an a flux box volume in two dimensions, taken from [20]

Since these points have to be interpolated in the poloidal plane, we can rewrite this simple finite difference for all grid points l, arranged in a vector, at once by using interpolation matrices

$$\left(\nabla_\parallel u\right)_{l,k+1/2} = \boldsymbol{Q}\cdot\boldsymbol{u}\big|_{l,k+1/2} = \frac{\left(\boldsymbol{C}_{fwd}\cdot\boldsymbol{u}_{k+1} - \boldsymbol{C}_{bwd}\cdot\boldsymbol{u}_k\right)_l}{s_{l,k+1/2}(\Delta\varphi/2) + s_{l,k+1/2}(-\Delta\varphi/2)}, \tag{117}$$

where $\boldsymbol{Q}$ is the complete matrix representation of the parallel gradient, while $\boldsymbol{C}_{fwd}$ and $\boldsymbol{C}_{bwd}$ are the interpolation matrices for the forward and backward neighbouring plane.

The parallel divergence is now constructed according to the support operator method [78]. The important property, which is kept from the continuous level towards the discrete one with this method, is the following

$$\int_V u\nabla\cdot(\boldsymbol{b}\nabla_\parallel v)\,\mathrm{d}V = -\int_V \nabla_\parallel u\nabla_\parallel v\,\mathrm{d}V + \int_{\partial V} ..., \tag{118}$$

where the integral over the boundary of the volume is dropped, as this has to be addressed via boundary conditions and is therefore treated separately. Note that for the discrete version the integrand of the left integral is living on the canonical grid, while the integrand of the right integral is living on the dual grid. Therefore the finite volumes, which approximate the integrals, are not the same. A visualisation of a flux box volume in two dimensions is shown in fig. 25. If $\varphi = 0$ at the canonical plane $k = 0$ The volume of the left integral is

$$V = \int_{-\Delta\varphi/2}^{\Delta\varphi/2} A(\varphi)\gamma(\varphi)\,\mathrm{d}\varphi \tag{119}$$

and for the right integral it is

$$\Lambda = \int_0^{\Delta\varphi} A(\varphi)\gamma(\varphi)\,\mathrm{d}\varphi, \tag{120}$$

which is not necessarily the same. $A(\varphi) = A(0)B_\varphi(0)/B_\varphi(\gamma(\varphi))$ is the cross-section of the flux box we are following due to magnetic flux conservation and $A(0) = h^2$ with h the grid spacing. Now we are able to translate the formula above into its discrete formulation

$$\sum_{\alpha,\beta,\gamma} u_\alpha P_{\alpha,\beta} Q_{\beta,\gamma} v_\gamma V_\alpha = -\sum_{\mu,\nu,\xi} Q_{\mu,\nu} u_\nu Q_{\mu,\xi} v_\xi \Lambda_\mu, \tag{121}$$

where $P_{\alpha,\beta}$ denotes the parallel divergence and V_α the finite flux box volume of grid point α on the canonical grid G and Λ_μ the flux box volume of grid point μ on the dual grid $G^\star$. Since this equation has to hold true for any u and v we find after renaming the indices

$$P_{\alpha,\beta} = -Q_{\beta,\alpha}\frac{\lambda_\beta}{V_\alpha} \tag{122}$$

by interpreting $\boldsymbol{V}$ and $\boldsymbol{\Lambda}$ as diagonal matrices with the corresponding flux box volumes as entries, we can write the equation as

$$\boldsymbol{P} = -\boldsymbol{V}^{-1}\boldsymbol{Q}^T\boldsymbol{\Lambda}. \tag{123}$$

With this method of constructing the parallel divergence, we make sure that the parallel divergence is the negative adjoint operator with regard to the parallel gradient also on the discrete level. Therefore the property of eq. (118) is conserved also in the discrete formulation up to machine precision.

4.1.2 Landau-Fluid closure as 3D-problem

During the construction of parallel operators, we recognised that they become three-dimensional in the framework of FCI, in comparison to flux-aligned coordinate systems, where they stay one-dimensional. We take a look at the equation for the Landau-fluid heat flux eq. (95) again

$$\left(\frac{\delta_\alpha \beta_n}{\lambda_{\text{mfp}}}\right)^2 q^{\text{LF}}_{\parallel\alpha,n} - \nabla_\parallel \left(\nabla \cdot \left(\boldsymbol{b}\, q^{\text{LF}}_{\parallel\alpha,n}\right)\right) = -A\frac{\delta_\alpha}{\lambda_{\text{mfp}}}\alpha_n \nabla_\parallel T_\alpha, \tag{124}$$

which we write down here ad hoc in terms of the available parallel operators, which are the parallel gradient and divergence. This equation lives on the dual grid since $q_\parallel$ is defined on the dual grid, as well as the gradient of the divergence of $q_\parallel$ and the gradient of temperature. Since the temperature is a known quantity, the evaluation of the right-hand side can be done with a simple matrix-vector multiplication. The left-hand side can be written as a matrix $\boldsymbol{A} = \boldsymbol{Q}^T\boldsymbol{Q}$, with the sparse matrix $\boldsymbol{Q}$. The first term of eq. (124) is a diagonal matrix and the second term a matrix including off-diagonal elements. The whole equation can be written as

$$\boldsymbol{A} \cdot \boldsymbol{q} = \boldsymbol{r}, \tag{125}$$

with $\boldsymbol{q}$ the vector of all values of the parallel heat flux and $\boldsymbol{r}$ the right-hand side of the equation. Since the problem is three-dimensional, the vector $\boldsymbol{q}$ has a length of $N \times P$ with N the number of points per plane and P the number of planes. The Matrix $\boldsymbol{A}$ has therefore the dimension $(N \times P) \times (N \times P)$, but is sparse. In GRILLIX a parallelisation is used across the poloidal planes, where every plane is handled by a separate process of the Message-Passing-Interface (MPI). The matrix $\boldsymbol{A}$ is usually too large for the usage of direct solvers, so iterative methods are considered. To avoid the necessity of building the dense matrix $\boldsymbol{A}$, the PIM (Parallel Iterative Methods) library [79] is used, which just needs information about the sparse matrices $\boldsymbol{Q}$ and $\boldsymbol{Q}^T$. This library provides a set of parallel matrix-free methods that can solve equations of type eq. (125), which are spread across different MPI processes with a low communication effort and without building a global matrix.

4.1.3 Parallel boundary conditions

There are perpendicular and parallel boundary conditions present in GRILLIX. The perpendicular ones are treated numerically in a rather standard way as expected for an unstructured equidistant grid. For parallel heat flux, the perpendicular boundary conditions are homogeneous Neumann boundary conditions. There is no major influence of these boundary conditions expected and found since buffer zones, particle and heat sources are active as well in the regions where the perpendicular boundary conditions are applied. In FCI the parallel boundary conditions are enforced as source terms within an immersed boundary method [37, 80]. Therefore a penalisation function χ is defined with a value of $\chi = 0$ inside the domain and $\chi = 1$ where the boundary conditions are applied. The transition between the two domains happens smoothly and can be tuned via a penalisation strength $1/\epsilon$. The penalisation is visualised in fig. 26.

With this penalisation function, the parallel boundary conditions are added as explicit terms to the equations we want to solve, so an equation of the form of eq. (125) reads then

$$(1-\chi)\,\boldsymbol{A} \cdot \boldsymbol{q} + \frac{\chi}{\epsilon}\boldsymbol{q} = (1-\chi)\,\boldsymbol{r} + \frac{\chi}{\epsilon}\boldsymbol{q}_{\text{bnd}}, \tag{126}$$

with $\boldsymbol{q}_{\text{bnd}}$ the value of the Dirichlet boundary condition, which is opposed here. The parallel boundary conditions applied to the heat flux at the divertor targets are sheath

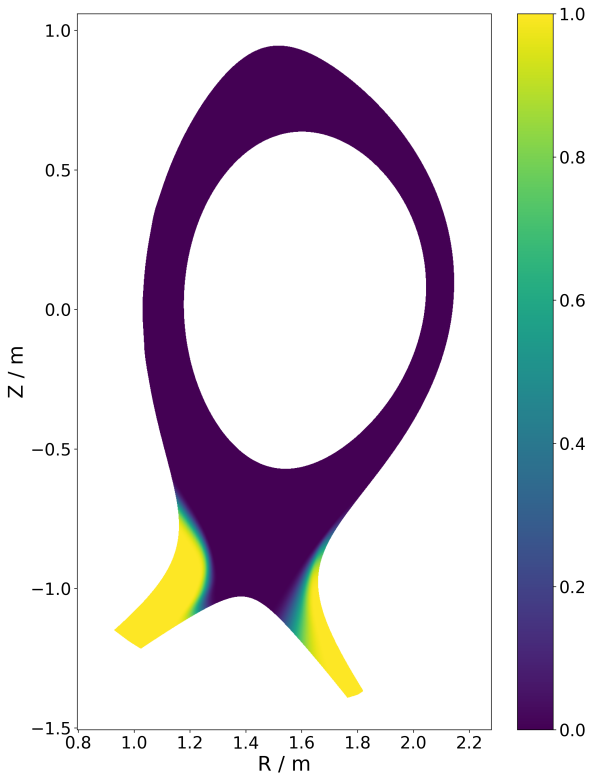

Figure 26: Penalisation function χ, which reaches from 0 to 1 and immerses the parallel boundary conditions

boundary conditions, defined in eq. (131), as proposed e.g. in [63]. Regarding the Landau-fluid closure, sheath boundary conditions can be applied directly to the heat flux as a Dirichlet boundary condition. For the Braginskii closures, on the other hand, sheath boundary conditions have to be applied via Neumann boundary conditions on the temperature.

4.1.4 Magnetic flutter in FCI

The effect of magnetic flutter was implemented into GRILLIX recently [50]. We investigate shortly the consequences of magnetic flutter on the implementation of the Landau-fluid closure for the parallel heat flux. The effect of magnetic flutter corresponds physically to small perturbations $\boldsymbol{B}_1 = \nabla \times A_\parallel$ of the background magnetic field $\boldsymbol{B}_0$ lines due to turbulent fluctuations in the parallel vector potential $A_\parallel$. A background and perturbed magnetic field line is visualised (not to scale) in fig. 27

The treatment of magnetic flutter within the FCI approach modifies parallel operators, e.g. the parallel gradient takes the form

$$\nabla_\parallel f = \frac{\mathbf{B}_0}{B_0} \cdot \nabla f - \frac{\mathbf{B}_0}{B_0^2} \cdot \left(\nabla A_\parallel \times \nabla f \right), \tag{127}$$

where the term including the fixed magnetic background B_0 is treated internally still via stored mapping matrices, as explained at the beginning of this chapter. The deviation from the B_0 due to magnetic flutter is treated via a perpendicular correction term. In the

Landau-fluid closure eq. (124) this modification of parallel operators applies to the parallel gradient of temperature on the right-hand side and the second-order parallel derivative on the left-hand side. In globally aligned approaches the inclusion of magnetic flutter on the right-hand side of eq. (124) is easy to implement and works the same way as including magnetic flutter in the temperature gradient of a Braginskii-type closure [65]. On the other hand, due to the implementation of the left-hand side, many advantages of field-aligned codes are lost, since the originally one-dimensional problem would become three-dimensional. However, since the parallel operators are already three-dimensional in the framework of FCI the inclusion of both terms is natural and quite straightforward.

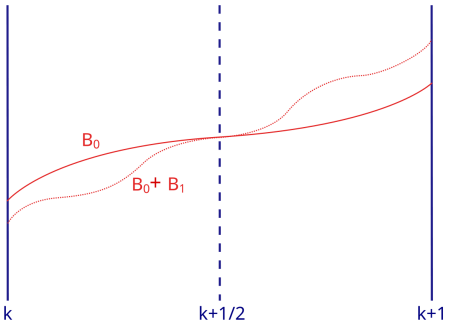

Figure 27: Visualisation of magnetic flutter with a background magnetic field line $\boldsymbol{B}_0$ and a small perturbation $\boldsymbol{B}_1$, not to scale

4.2 Implementation

4.2.1 Implemented Landau-fluid equation

The current set of equations employed by GRILLIX is listed in appendix A. Two equations need to be adapted, namely the two temperature equations (eq. (151), eq. (152)), in which the Braginskii expressions (eq. (60)) for $q_{\parallel e}$ and $q_{\parallel i}$ are replaced by the Landau-fluid expressions (eq. (95)). In order to solve the model equations numerically, the normalisation of GRILLIX has to be applied to eq. (124). The magnetic field is normalised by B_0, the density by n_0, the temperatures via T_{e0} and T_{i0}, the electrostatic potential by T_{e0}/e, the parallel velocities by sound speed $c_{s0} = \sqrt{T_{e0}/M_i}$, the current by $c_{s0}en_0$, the perpendicular length scales by $\rho_{s0} = c\sqrt{T_{e0}M_i}/(eB_0)$, the parallel length scales by R_0, the time by R_0/c_{s0} and the parallel component of the magnetic vector potential by $\beta_0 B_0 \rho_{s0}$, with $\beta_0 = 4\pi n_0 T_{e0}/B_0^2$.

After applying penalisation and expressing quantities in their normalised versions, starting from the Landau-fluid equation eq. (95) we arrive at

$$\begin{aligned} \frac{\chi^e_{\parallel 0}\sqrt{\mu}}{3.16\delta_e\alpha_n\sqrt{8/\pi}} \left((1-\chi)\left[\left(\frac{3.16\delta_e}{\chi^e_{\parallel 0}\sqrt{\mu}} \frac{\hat{n}}{\hat{T}_e^2}\beta_n \right)^2 - \hat{\nabla}_\parallel \left(\hat{\nabla}\cdot\mathbf{b} \right) \right] + \frac{\chi}{\epsilon} \right) \hat{q}_{\parallel e,n} \\ = -(1-\chi)\frac{1}{\sqrt{\mu}} \frac{\hat{n}^2}{\sqrt{\hat{T}_e}} \hat{\nabla}_\parallel \log \hat{T}_e + \frac{\chi}{\epsilon}\hat{q}_{\parallel e,n,\mathrm{bnd}}, \end{aligned} \tag{128}$$

$$\begin{aligned}\frac{\chi^i_{\parallel 0}\zeta^{-1/2}}{3.9\delta_i\alpha_n\sqrt{8/\pi}}&\left((1-\chi)\left[\left(\frac{3.9\delta_i}{\chi^i_{\parallel 0}\zeta^{-1/2}}\frac{\hat{n}}{\hat{T}_i^2}\beta_n\right)^2-\hat{\nabla}_\parallel\left(\hat{\nabla}\cdot\mathbf{b}\right)\right]+\frac{\chi}{\epsilon}\right)\hat{q}_{\parallel i,n}\\ &=-(1-\chi)\sqrt{\zeta}\frac{\hat{n}^2}{\sqrt{\hat{T}_i}}\hat{\nabla}_\parallel\log\hat{T}_i+\frac{\chi}{\epsilon}\hat{q}_{\parallel i,n,\mathrm{bnd}},\end{aligned} \tag{129}$$

where a hat indicates normalised quantities, $\mu = m_e/M_i$ is the mass ratio between electrons and ions, $\zeta = T_{i0}/T_{e0}$ the ratio of normalised ion and electron temperature and $\mathbf{b} = \mathbf{B}_0/B_0$ is the unit vector in the direction of the magnetic field, which is the parallel direction. The parallel derivatives on the left-hand side act on $\nabla_\parallel(\nabla\cdot(\mathbf{b}\hat{q}_{\parallel,n}))$. The factor $\chi^\alpha_{\parallel 0}$ is the normalised Braginskii heat conductivity which is

$$\chi^\alpha_{\parallel 0} = \begin{cases} 3.16\, c_{s0}\tau_{e0}/\left(\mu R_0\right) & \text{for electrons,}\\ 3.9\, c_{s0}\tau_{i0}\zeta/R_0 & \text{for ions.}\end{cases} \tag{130}$$

The parallel boundary condition $\hat{q}_{\parallel\alpha,\mathrm{bnd}}$ take the form [63]

$$\hat{q}_{\parallel e,n,\mathrm{bnd}} = \begin{cases} \pm\frac{\gamma_{sh,e}\sqrt{\mu}\chi^e_{\parallel 0}\hat{n}\hat{T}_e\sqrt{\hat{T}_e+\zeta\hat{T}_i}}{3.16\delta_e\alpha_n\sqrt{8/\pi}} & \text{for } n=1,\\ 0 & \text{for } n\neq 1,\end{cases} \tag{131}$$

$$\hat{q}_{\parallel i,n,\mathrm{bnd}} = \begin{cases} \pm\frac{\gamma_{sh,i}\chi^i_{\parallel 0}\hat{n}\hat{T}_i\sqrt{\hat{T}_e+\zeta\hat{T}_i}}{3.9\delta_i\sqrt{\zeta}\alpha_n\sqrt{8/\pi}} & \text{for } n=1,\\ 0 & \text{for } n\neq 1,\end{cases} \tag{132}$$

with $\gamma_{sh,\alpha}$ the conductive sheath heat transmission factor, which has a value of $\gamma_{sh,e} = 1.0$ for electrons and $\gamma_{sh,i} = 0.1$ for ions in the presented simulations of ASDEX Upgrade in the following two chapters. The factor ± 1 corresponds to the outer and inner divertor leg. The implementation of the eqs. (128) and (129) is checked via MMS and explained in more detail later.

4.2.2 Solvers

Due to the size of the three-dimensional problem we aim to solve, direct solvers are no option. Until now for solving the set of elliptic equations of the Landau-fluid closure a robust GMRES (Generalised Minimal RESidual) algorithm provided by the PIM library [79] is used, which also offers matrix-free methods as mentioned before. To speed up convergence a Jacobi preconditioner is used. The GMRES algorithm [81] belongs to the class of Krylov-subspace solvers and is applicable to a wide range of problems since the matrix $\boldsymbol{A}$ has to be only invertible, without further criteria. However, for the presented problem we know about additional properties of our matrix $\boldsymbol{A}$. By constructing parallel operators via the support operator method, we find the discrete version of the second derivative in eq. (124)

$$\nabla_\parallel\left(\nabla\cdot(\boldsymbol{b}f)\right) \quad\Rightarrow\quad \boldsymbol{QP}f, \tag{133}$$

where $\boldsymbol{P} = -\boldsymbol{V}^{-1}\boldsymbol{Q}^T\boldsymbol{\Lambda}$. The first term on the left-hand side of eq. (124), can be ignored here since it corresponds to a diagonal matrix. The matrix $\boldsymbol{QP}$ is by construction self-adjoint, as $\boldsymbol{P}$ is derived from $\boldsymbol{Q}$ to keep this property on the discrete level (eq. (123))

Furthermore, the matrix $\boldsymbol{QP}$ is symmetric up to the flux bx volumes. When ignoring the box volumes for a moment by assuming $V_\beta/\Lambda_\alpha \approx 1 \; \forall \; \alpha, \beta$, the matrix $\boldsymbol{QP} = -\boldsymbol{QQ}^T$ is by construction also symmetric.

Since $\boldsymbol{QP}$ is self-adjoint, it is also positive definite. The properties of our matrix are then to be symmetric and positive-definite. With these properties of the matrix, it should be possible to utilise more efficient methods for solving this problem numerically, e.g. a CG (Conjugate-Gradient) algorithm [82]. Within a CG algorithm, each iteration requires the same amount of numerical operations, unlike the GMRES, where the number of operations grows with the iteration number squared. Employing a CG algorithm should be therefore computationally advantageous.

Initial tests to utilise a CG algorithm, also provided by the PIM library, in GRILLIX were made. The method works for simple geometries, like a periodic slab. However, by changing to more complex diverted geometries, the CG solver does not converge. Investigations regarding this issue revealed that the algorithm does not converge when the flux box volumes deviate from unity. Further points that might break the symmetry or the positive-definiteness of the matrix $\boldsymbol{QP}$ are the penalisation function χ or the treatment of boundary and ghost points on the plane.

In summary, the problem was found and it should be possible to utilise more efficient algorithms for solving the set of Landau-fluid equations by changing the way how it is implemented. However, this task was beyond the scope of this thesis.

4.3 Verification

4.3.1 Method of manufactured solutions

Reproduced from C. Pitzal, A. Stegmeir, W. Zholobenko, K. Zhang, and F. Jenko, "Landau-fluid simulations of edge-SOL turbulence with GRILLIX," Physics of Plasmas, vol. 30, no. 12, 2023., with the permission of AIP Publishing.

"To verify the correctness of the implementation the method of manufactured solutions (MMS) [83] is used. The test is performed in slab geometry with three Cartesian coordinates $x \in [0, 1]$, $y \in [0, 1]$ periodic and $z \in [0, 2\pi]$ periodic and a time coordinate $t \in [0, 0.5]$. The model parameters used in GRILLIX are set to the be $\delta_0 = 680$, $\eta_{\parallel 0} = 1.2$, $\eta_{i0} = 0.3$, $\nu_{e0} = 0.2$, $\zeta = 0.8$, $\beta_0 = 0.05$, $\nu = 0.01$, $\kappa_{\parallel e0} = 0.12$ and $\kappa_{\parallel i0} = 0.1$. Analytical solutions for all dynamical quantities including $q_{\parallel e}$ and $q_{\parallel i}$ are prescribed. The neutrals model is tested separately and not shown here. The analytical solution for any plasma quantity has the form:

$$f_{\mathrm{MMS}}(x, y, z, t) = \alpha_0 + \alpha_1 \sin\left(2\pi\, k_x\, x\right) \sin\left(2\pi\, k_y\, y - \phi_y\right) \cos\left(k_z\, z - \phi_z\right) \sin\left(\omega t - \phi_t\right), \tag{134}$$

with the corresponding parameters for each plasma field shown in table 2.

With these analytical solutions, source terms are calculated as described as in Salari et al. [83]. Those source terms are added on the right-hand side of all equations in appendix A and also for the two Landau-fluid equations eq. (128) and eq. (129). Those source terms are calculated with a symbolic computation program, in this case, Mathematica. With MMS we can verify that e.g. eq. (128) and eq. (129) are implemented as

	α_0	α_1	k_x	k_y	ϕ_y	k_z	ϕ_z	ω	ϕ_t
n	1.15	1.0	1.0	2.0	0.1	1.0	1.1	59.0	0.4
ϕ	0.0	0.8	1.0	3.0	0.7	1.0	0.2	83.0	1.1
$u_\parallel$	0.0	1.3	2.0	2.0	1.2	1.0	0.1	99.0	0.5
$A_\parallel$	0.0	0.7	1.0	3.0	0.5	1.0	0.6	66.0	0.3
T_e	1.3	1.2	2.0	3.0	0.3	1.0	0.5	79.0	0.1
T_i	1.07	0.9	2.0	2.0	0.4	1.0	0.8	61.0	0.6
$q_{\parallel e}$	0.0	0.5	2.0	3.0	0.8	1.0	0.4	71.0	0.7
$q_{\parallel i}$	0.0	0.6	1.0	2.0	0.6	1.0	0.3	51.0	0.2

Table 2: Parameters for the numerical solutions eq. (134) for each dynamical plasma field including $q_{\parallel e}$ and $q_{\parallel i}$

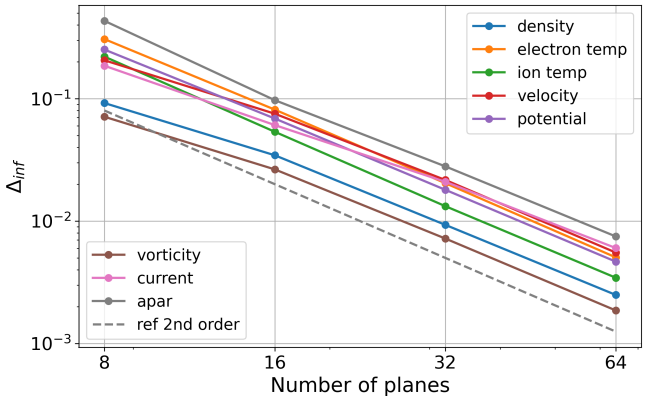

Figure 28: Supremum norm of numerical error Δ_{inf} for MMS verification of the Landau-fluid closure in slab geometry

they are written down here and that the solution converges against the prescribed analytical solution with the expected order of discretization, for our case second order in space. We have tested numerous subsystems, including just the parallel-heat-flux term isolated or just the two temperature equations isolated. In fig. 28 the results of such a convergence test for the full system including all terms are shown starting with 8 poloidal planes and 1120 points per plane, doubling the parallel perpendicular and temporal resolution three times until we arrive at 64 poloidal planes. The supremum norm of the numerical error Δ_{inf} of all plasma quantities is converging as expected with second order. Therefore we have strong evidence that the implementation was performed correctly. The supremum norm of the numerical error is given by $\Delta_{\text{inf}} = |f_{\text{num}} - f_{\text{MMS}}|_\infty / |f_{\text{MMS}}|_\infty$ with the numerical solution f_{num} obtained by GRILLIX and the analytical MMS solution f_{MMS} for each plasma field. The model was tested in simple slab geometry for the purpose of finding e.g. typing errors in the implementation of the model. The 3D-solvers used for solving eq. (128) and eq. (129) and the model with limited Braginskii closure are also tested in more complex geometries. The test performed here is not the pinnacle of verification, but it adds one additional layer of safety."

4.3.2 Comparison to 1D toy model

An additional layer of verification was added by comparing the Landau-fluid heat flux predicted by GRILLIX to the predictions of the one-dimensional toy model from section 3. For this purpose, a case was specially set up in GRILLIX. The geometry is as simple as possible, a set of 32 circular planes with a homogeneous magnetic field along the parallel direction and parallel periodic boundary conditions. In this geometry a Gaussian temperature distribution according to eq. (108) along the parallel direction with $T_0 = 100\,\mathrm{eV}$ is prescribed, along the radial coordinate the distribution is also Gaussian. A sketch of this setup is shown in fig. 29, where in red an equi-temperature surface is visualised, which has the form of a blob. In green the magnetic field lines are plotted and in orange the line of sight, i.e. the line along the comparison between GRILLIX and the one-dimensional model is performed. A case with the same number of points and the same length of the system is used in the one-dimensional model.

To perform the comparison, the normalisation of both models has to be checked against each other and all the physical parameters need to be specified with identical precision. Further, we have to make sure that the peak temperature is the same since the grid generated by GRILLIX does not necessarily have a point at the position $(x = 0, y = 0)$ on a poloidal plane, however, the temperature is initialised with an analytical Gaussian profile with a peak at $(x = 0, y = 0)$. Therefore the temperature of the 1D-model was prescribed to match exactly the peak value on the line of sight in GRILLIX. After taking care of such issues we compare the temperature profiles as well as the Landau-fluid heat fluxes predicted by the two codes in fig. 30. Here we find that both quantities match qualitatively. For the sake of brevity, we compare here just the electron heat fluxes, similar tests were performed for the ion heat fluxes.

To perform a quantitative comparison, we calculate the errors between the two codes according to

$$err(f) = \sum_i^N \frac{|f_{GR}(i) - f_{1D}(i)|}{N}. \tag{135}$$

For the temperature distribution, we find $err(T) = 9.638 \cdot 10^{-15}$, which is effectively machine precision. For the Landau-fluid heat flux, we find $err(q^{\mathrm{LF}}) = 2.391 \cdot 10^{-10}$. This error is not limited by machine precision but by the residuum of the iterative solver used in GRILLIX, which was chosen to be 10^{-10}. A similar test was performed for the Braginskii

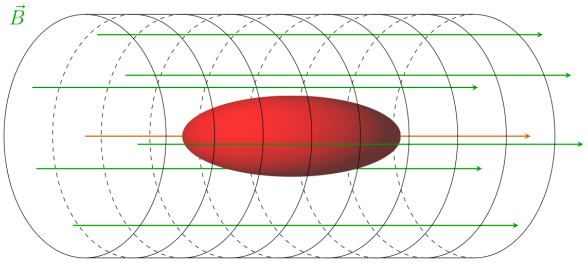

Figure 29: Sketch of the setup in GRILLIX for comparison to 1D model, in red an equi-temperature surface, in green magnetic field lines and in orange the line of sight

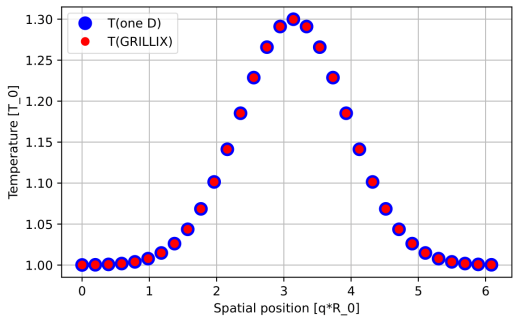

(a) Initial temperature in GRILLIX and the 1D model

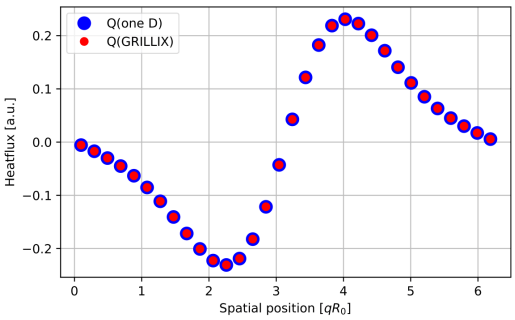

(b) Heat fluxes proposed by GRILLIX and the 1D model

Figure 30: Comparison between the 1D toy model and GRILLIX

heat flux, which just involves derivatives. Here an error of $err(q^{\mathrm{BR}}) = 9.120 \cdot 10^{-14}$ was found.

4.3.3 Blobs in AUG

One further test, which shows nicely the geometric capabilities of GRILLIX as well as the non-local character of the Landau-fluid heat flux is performed here. A similar temperature blob, Gaussian distribution in the plane but constant in parallel direction, is placed exactly on top of the X-Point in a magnetic equilibrium of an L-mode discharge in ASDEX Upgrade shown in fig. 31a. The Gaussian has again an amplitude of 30 % of the background temperature $T_0 = 100\,\mathrm{eV}$. Within GRILLIX the heat fluxes according to the Landau-fluid and the Braginskii closure were calculated and plotted in figs. 31b and 31c. The same plots are shown again with a strongly limited colour bar in figs. 31d and 31e, here we observe that the Braginskii heat flux stays local, while the Landau-fluid heat flux spreads non-locally along the separatrix. We want to emphasise, that the plots shown here involve no temporal evolution yet but are just the heat fluxes corresponding to the initial temperature distribution. A similar test was already performed with a blob at the top of a diverted tokamak with the code BOUT++ [49].

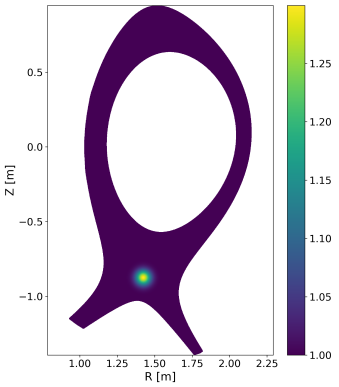

(a) Initial temperature

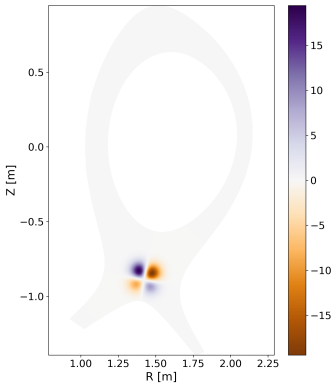

(b) Braginskii heat flux

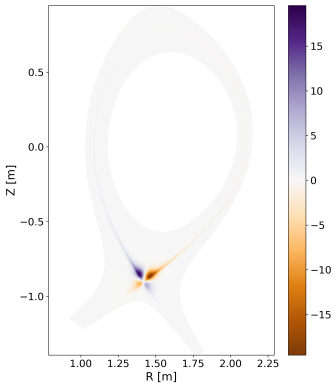

(c) Landau fluid heat flux

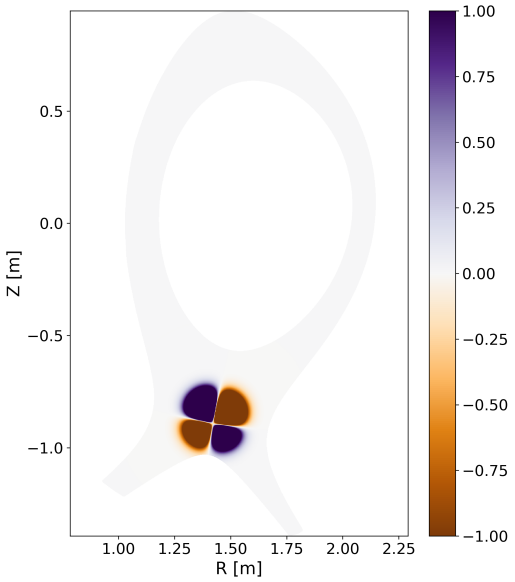

(d) Braginskii heat flux with limited colour bar

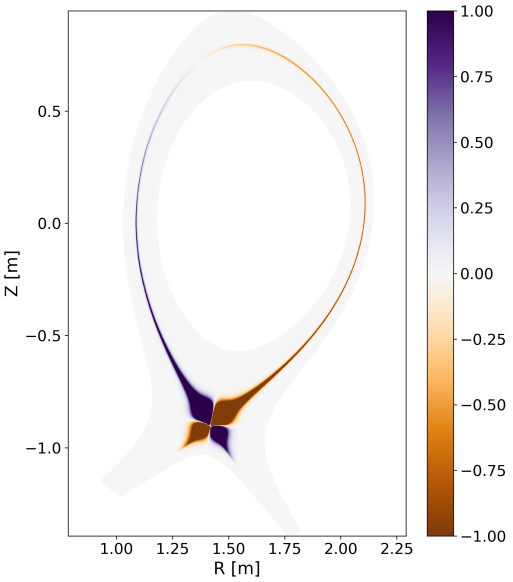

(e) Landau fluid heat flux with limited colour bar

Figure 31: Gaussian temperature distribution and heat fluxes according to the Landau-fluid and Braginskii closure

4.4 Chapter summary

Within this chapter, we explained the FCI approach with a special focus on parallel operators and how they are constructed. The Landau-fluid equation became three-dimensional within the framework of FCI. We saw, that the discrete version of the second-order parallel derivative in the elliptic Landau fluid equation is self-adjoint by construction of the parallel operators. However, the corresponding matrix does not have to be symmetric. Parallel boundary conditions are treated via a penalisation method and we showed how this modifies the implemented Landau fluid equation. Furthermore, the inclusion of magnetic flutter into the Landau-fluid closure was straightforward within FCI. The normalised and implemented elliptic Landau fluid equations were presented as well as the parallel sheath boundary conditions applied to them. We explained that currently a GMRES algorithm is used to solve these three-dimensional problems and that the possibility of employing also a CG algorithm exists, which would require further efforts and was beyond the scope of this work. To verify the implementation into GRILLIX the method of manufactured solutions was used and a comparison between the 1D model and GRILLIX was performed, which resulted in an agreement up to the residuum of the iterative 3D solver. Finally, the Landau fluid closure was tested in tokamak geometry, where a temperature blob was placed at the X-point and the corresponding non-local heat fluxes were calculated.

5 Turbulence simulations in ASDEX Upgrade

Reproduced from C. Pitzal, A. Stegmeir, W. Zholobenko, K. Zhang, and F. Jenko, "Landau-fluid simulations of edge-SOL turbulence with GRILLIX," Physics of Plasmas, vol. 30, no. 12, 2023., with the permission of AIP Publishing.

The parts section 5.1 up to section 5.6 are direct quotes from the mentioned publication including all figures within these sections. The corresponding sections are therefore marked with quotation marks.

In this chapter simulations based on a L-mode discharge in the ASDEX Upgrade (AUG) tokamak are performed and investigated in detail. The rough setup is visualised in fig. 32. The detailed simulation setup is explained as well as the parameters of the three performed simulations, which employ the Landau-fluid closure as well as the Braginskii-closure with different heat-flux limiters. Outboard-mid-plane (OMP) profiles are compared as well as the measured input power, required to keep up the prescribed temperature at the inner core boundary.

A spurious ion temperature asymmetry is found in the simulations with the Braginskii-closure and strong heat-flux limiters. It is shown, that this asymmetry evolves due to the artificial limitation of the parallel heat conductivity and the resulting interplay between parallel and diamagnetic heat fluxes.

The Landau-fluid closure within a turbulence simulation is investigated in detail, especially which of the Lorentz functions are active in the simulation and if the number of employed Lorentz functions is sufficient for this setup. Furthermore, we find a radial dependence of the active Lorentzians, in line with the decreasing collisionality towards the core boundary.

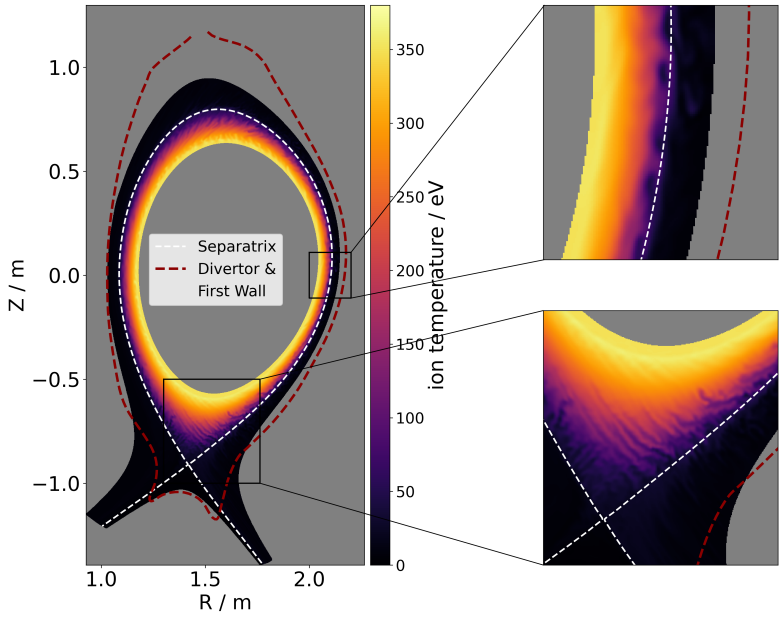

Figure 32: Ion temperature snapshot within a saturated turbulent state (same as fig. 6)

The non-locality of the Landau-fluid closure is also investigated during a turbulence simulation via an effective heat conductivity, which depends strongly on how the data were averaged. Finally, the performance of the simulations is compared.

5.1 Simulation Setup

"We investigate and compare the Landau-fluid closure with the previously used Braginskii closure in a fully non-linear turbulence simulation resembling the ASDEX Upgrade experiment. Three simulations are performed, the first one using the Braginskii closure with a strong heat-flux limiter ($\alpha = 0.1$), the second one also with the Braginskii closure but a weaker heat flux limiter ($\alpha = 1.0$) and the third one employs the Landau-fluid closure. The complete physical model is given in appendix A, for a comprehensive discussion of the model we refer to Zholobenko et al. [84]. Besides the Landau-fluid closure, two further model improvements have been applied since then, namely magnetic flutter and neoclassical ion viscosity. Magnetic flutter, as introduced in eq. (127), is used for all parallel operators in our system and for the Landau-fluid equations (128) and (129) just in the temperature gradient on the right-hand side, after preliminary tests showed that including it in the left-hand side does not change the physical results, but the computational cost of the 3d-solver is increased. The neoclassical ion viscosity extension is briefly discussed in appendix A. Both extensions will be discussed in detail in separate publications. The geometry and the equilibrium of these simulations are based on ASDEX Upgrade discharge #36190, an attached L-mode with a plasma current of 800 kA, $q_{95} = 4.4$ and an average triangularity of $\delta = 0.21$. The toroidal magnetic field strength is $B_{\text{tor}} = 2.5\,\text{T}$ on axis in favourable configuration, i.e. the ion-∇B drift points towards the active X-point. The plasma was heated in the experiment with Ohmic heating and neutral beam injection. After subtracting the radiation losses, which are not modelled by GRILLIX, the total input power was 475 kW in the experiment. Two species are considered in the simulation, electrons and deuterium ions. In all simulations, the density, electron and ion temperature are kept constant at the inner core boundary of our simulation domain by an adaptive source at $\rho_{\text{pol}} = 0.91$, which maintains the values $n(\rho_{\text{pol}} = 0.91) = 2.0 \times 10^{19}\,\text{m}^{-3}$ and $T_e(\rho_{\text{pol}} = 0.91) = T_i(\rho_{\text{pol}} = 0.91) = 350\,\text{eV}$. Additionally, a diffusive neutrals model is used for all the simulations [40], which requires a fixed neutrals density at the divertor as boundary condition, this value is here chosen to be $5.0 \times 10^{17}\,\text{m}^{-3}$. All parameters remain the same for the three simulations, except for the different heat flux closures employed."

5.2 General comparison

"The time traces of flux-surface-averaged density, electron and ion temperature at $\rho_{\text{pol}} = 0.998$ for all three simulations are depicted in fig. 33. Both the Braginskii case with weak limiter ($\alpha = 1.0$) and the Landau-fluid case seem to approach convergence. However the Braginskii case with strong limiter ($\alpha = 0.1$) shows a second rise in the electron and ion temperature starting at $t = 2.5\,\text{ms}$. This originates in a strong asymmetry in the ion temperature, which will be explained in more detail in section 5.3.

To compare the three simulations directly we plotted the outboard-midplane (OMP) profiles of density, electron and ion temperature on top of each other for the three simulations at $t = 2.5\,\text{ms}$ in fig. 34, averaged toroidally and over $\Delta t = 100\,\mu\text{s}$. The density

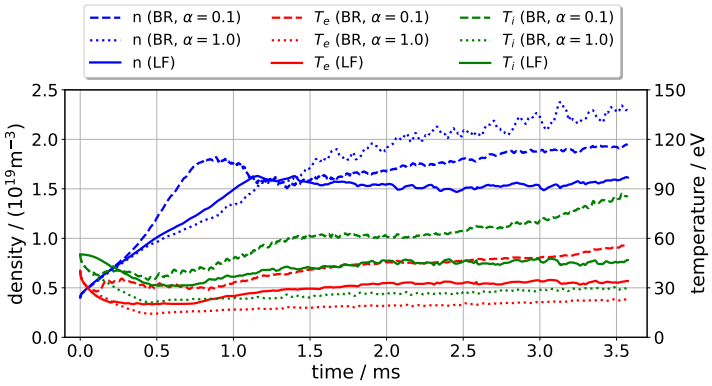

Figure 33: Time trace of flux-surface-averaged density, electron and ion temperature at $\rho = 0.998$

profiles exhibit distinct "shoulders" near the separatrix, especially for the two cases with Braginskii closure. These shoulders are caused by neutral gas that is ionised near the X-point. For the Landau-fluid closure, this effect is less pronounced. Since the neutrals density at the divertor is a free parameter in the model, a careful scan would be necessary to match the actual experimental values. However, this work focuses on the investigation of the different heat flux closures and their respective influence, an extensive validation against the experiment we leave for future work. The electron (fig. 34b) and ion temperature profiles (fig. 34c) are more directly influenced by the respective heat-flux closure. Here we see for the temperature of both species that the Landau-fluid case falls in between the two Braginskii cases in terms of separatrix temperature. Deep in the edge region ($\rho_{\text{pol}} < 0.97$) the three cases predict similar temperature profiles, except for the ion temperature profile of the Braginskii case with $\alpha = 0.1$, where the different shape of the ion temperature profile is due to an asymmetry in ion temperature, which is examined in the subsequent section. Looking closer especially at the temperature profiles, a decrease of the fluctuation amplitudes by going from $\alpha = 0.1$ to $\alpha = 1.0$ to the Landau-fluid model is visible. This indicates a change in the underlying turbulent dynamics. To investigate this a little deeper, the radial electric field is shown in fig. 34d. The origin and properties of the radial electric field in simulations with GRILLIX were analysed in great detail by Zholobenko et al. [84] for the same setup and compared with the experimentally measured values. We find that with the Landau-fluid closure the quantitative values of the radial electric field are significantly closer to the experiment [40]. An extensive discussion of the influence of the closure on the radial electric field will be left for the future since it is

	P_e	P_i
Braginskii ($\alpha = 0.1$)	350 kW	600 kW
Braginskii ($\alpha = 1.0$)	20 kW	400 kW
Landau-fluid	40 kW	400 kW
experiment	475 kW	

Table 3: Input powers for electrons P_e and ions P_i for all three cases taken at $t = 2.5$ ms and averaged for $\Delta t = 500\,\mu$s

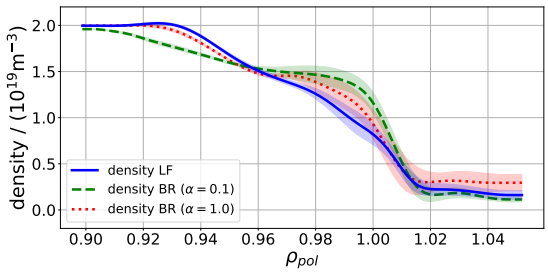

(a) OMP density profiles

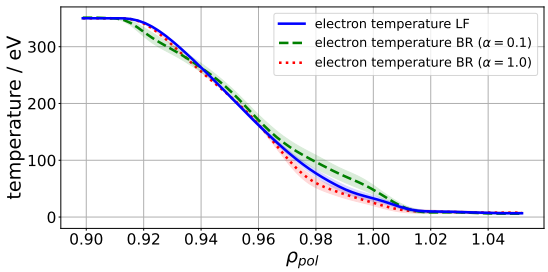

(b) OMP electron temperature profiles

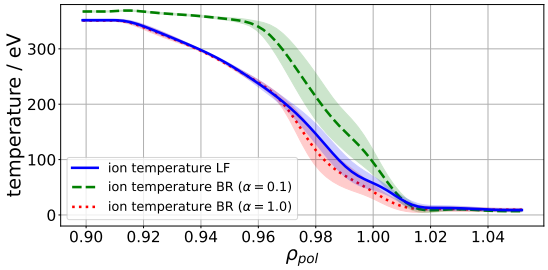

(c) OMP ion temperature profiles

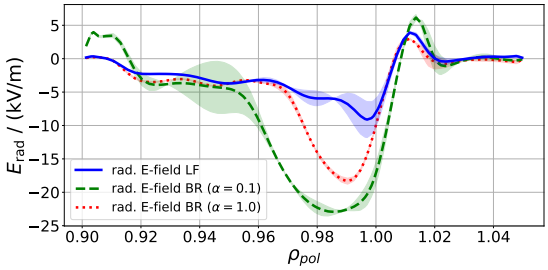

(d) OMP radial electric field profiles

Figure 34: OMP profiles with fluctuation amplitudes (shaded) at $t = 2.5\,\text{ms}$ averaged over $\Delta t = 100\,\mu\text{s}$

beyond the scope of this work.

Comparing the input power in table 3, we observe the Braginskii case ($\alpha = 1.0$) and Landau-fluid being similar in terms of total input power and close to the experiment. The case with Braginskii closure ($\alpha = 0.1$) deviates strongly in electron input power, regardless of the just slightly flatter electron temperature profile (fig. 34b). Nevertheless, the flux limiters work as expected since an increase in α leads to smaller temperature fluctuations therefore to decreased radial heat transport, so less input power is needed to keep the temperature constant at the core boundary. In Zholobenko et al. [40] a very similar case was considered in the original Braginskii limit ($\alpha \to \infty$). Such simulations are computationally challenging as the parallel heat conductivity is becoming very stiff. A further steepening of the profiles and a very low input power, much lower than typical experimental values, were obtained."

5.3 Parallel vs. diamagnetic heat fluxes

"The already mentioned asymmetry in ion temperature for the Braginskii case ($\alpha = 0.1$) becomes apparent by looking at the corresponding ion temperature across the whole simulation domain in fig. 35 in comparison with the two other cases. A strong up-down asymmetry is present in the ion temperature which is shifted in anti-clockwise direction due to the poloidal $E \times B$ rotation. Since this asymmetry is still present at the OMP, it determines the shape of the ion temperature profile fig. 34c.

The origin of this asymmetry lies in an interplay between perpendicular and parallel heat fluxes within our system. In toroidal plasmas the main component of the perpendicular heat flux is diamagnetic and not divergence-free

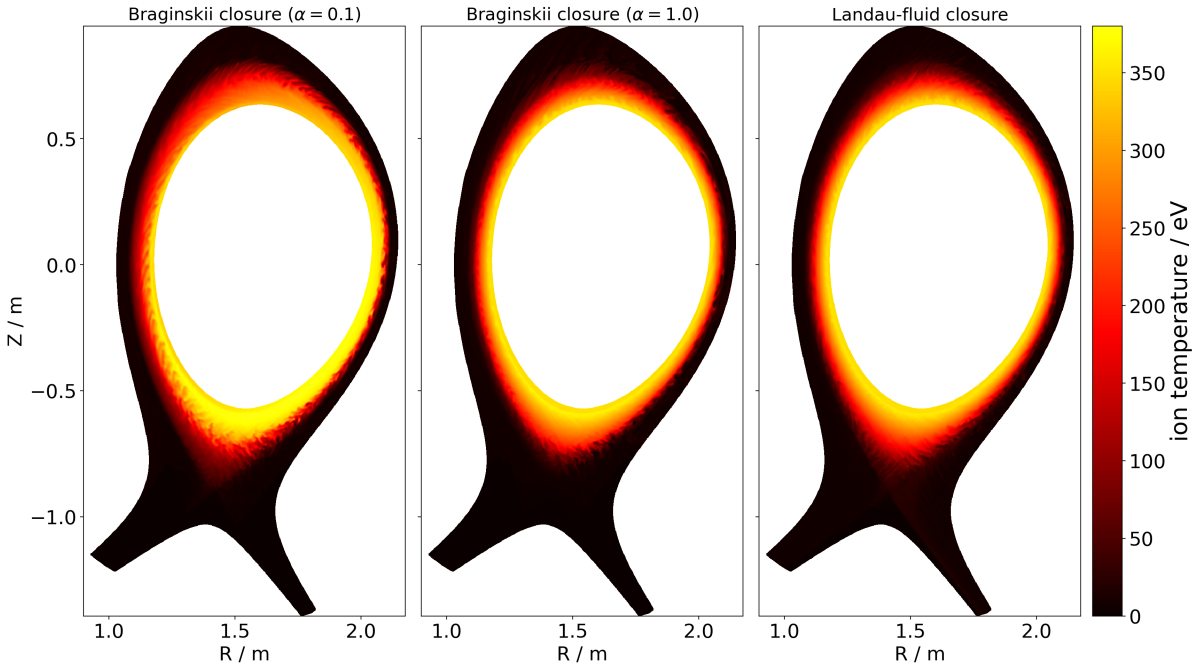

Figure 35: Ion temperature at $t = 2.5\,\mathrm{ms}$ with strong poloidal asymmetry for Braginskii ($\alpha = 0.1$), but not for the two other cases

$$\nabla \cdot \left(\frac{5 p_j}{2 q_j B^2} \mathbf{B} \times \nabla T_j \right) \neq 0 \tag{136}$$

due to the toroidicity of the geometry, with p_j the pressure and q_j the charge of each species, $\mathbf{B}$ the magnetic field and B its absolute value. For the total heat flux to become divergence-free, which is a requirement for steady state, there is an additional parallel return flux necessary (Helander et al., chapter 8) [55]. This parallel return flux is realised in our system via the parallel conductive heat flux $q_\parallel$ and is driven by a temperature gradient along a field line connecting the minimum and maximum of the temperature asymmetry. As we limit the parallel conductive heat flux artificially and quite substantially for the Braginskii case ($\alpha = 0.1$), the total heat flux is not divergence-free and we observe an accumulation of ion temperature in the region of poloidal angle $\theta \in (3\pi/2, 2\pi)$ (between the X-point and the OMP). The temperature asymmetry is building up during the simulation and therefore the flux surface averaged electron and ion temperatures rise again in fig. 33 when the temperature asymmetry reaches $\rho_{\mathrm{pol}} = 0.998$ at approximately $t = 2.5\,\mathrm{ms}$. The term in the ion temperature equation eq. (152) that contains the diamagnetic heat flux is $5/2\zeta \hat{T}_i C(\hat{T}_i)$, for electrons in eq. (151) respectively $-5/2\hat{T}_e C(\hat{T}_e)$, and is referred to in the following as curvature term. The parallel term that balances the diamagnetic term is $1/\hat{n}\nabla \cdot \left(\hat{q}_{\parallel i}\mathbf{b}\right)$ in eq. (152) and $1/\hat{n}\nabla \cdot \left(\hat{q}_{\parallel e}\mathbf{b}\right)$ in eq. (151) and is referred to in the following as parallel-heat-flux term.

The limitation of the parallel conductive ion heat flux for the Braginskii ($\alpha = 0.1$) case is indeed apparent from fig. 37a, where $< | < q_{\parallel i} >_\varphi | >_{\theta,t}$ is plotted. On the other hand, the electron heat flux in fig. 37b shows no big difference between the two Braginskii cases, but for the Landau-fluid case. Firstly, we note that the limiting free-streaming heat

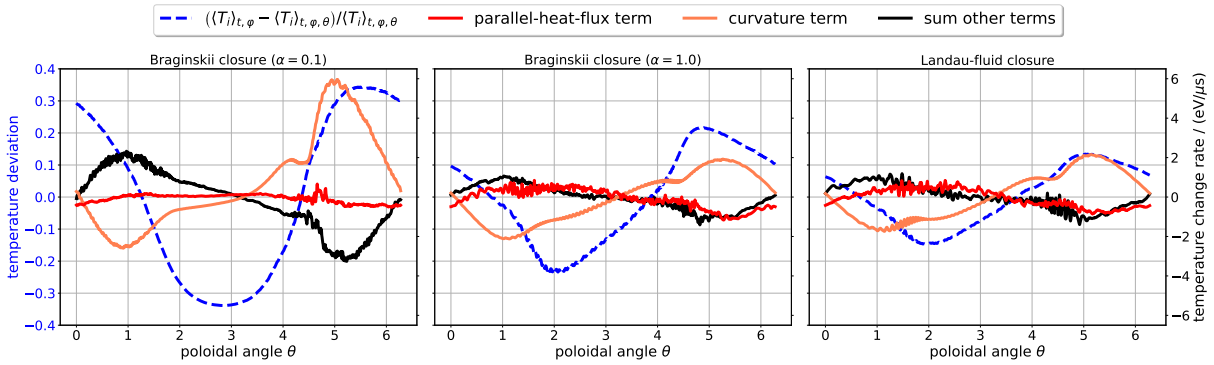

Figure 36: Ion temperature deviation, curvature and parallel-heat-flux term and the sum over the remaining terms of the ion temperature equation eq. (152) along the flux surface $\rho_{\text{pol}} = 0.965$ at $t = 2.5\,\text{ms}$ averaged over $\Delta t = 100\mu\text{s}$

conductivity is about a factor $\sqrt{M_i/m_e} \approx 60$ higher for electrons than ions. Secondly, we have to keep in mind that the heat conductivity is limited and not the heat flux directly. Therefore, we additionally plot $< | < \nabla_\parallel T_j >_\varphi | >_{\theta,t}$ in figs. 37c and 37d. As expected, we find for electrons in the case Braginskii ($\alpha = 0.1$) that the similar amplitude of the heat flux in comparison with the case Braginskii ($\alpha = 1.0$) can just be obtained by a significantly larger parallel temperature gradient in the quasi-stationary state. We want to highlight that the Braginskii case ($\alpha = 1.0$) is still limited in comparison to an unlimited Braginskii case ($\alpha \to \infty$), which would provide significantly larger parallel heat fluxes for comparable temperature gradients. Interestingly we note that the parallel electron heat flux for the Landau-fluid case is large despite the small parallel temperature gradient, which illustrates that no simple linear connection between $\nabla_\parallel T$ and $q_\parallel$ exists for this case. This finding is investigated in more detail in section 5.5.

To ensure that the asymmetry in ion temperature is caused by the curvature term and balanced by the parallel-heat-flux term, we examine those terms along the flux surface at $\rho = 0.965$. The value of ρ is chosen to match the radial position of the largest temperature asymmetry. This analysis is performed for all three cases and depicted in fig. 36, the black line shows the sum of all remaining terms of eq. (152). The ion temperature asymmetry is strongest for the case with Braginskii closure ($\alpha = 0.1$) and weakest for the case with the Landau-fluid closure. The analysis confirms that the curvature term is building up the asymmetry as it peaks for all cases near the maximum of the temperature asymmetry and is again strongest for the case with Braginskii closure ($\alpha = 0.1$). We can not compare the three cases one to one, since every case is a full non-linear turbulence simulation and changing the parallel heat conduction changes the state of the whole system. Nevertheless the parallel-heat-flux term in fig. 36 for Braginskii ($\alpha = 1.0$) and Landau-fluid together with the sum of the remaining terms of the ion temperature equation (black line) counteracts the curvature term and decreases the ion temperature asymmetry. For Braginskii ($\alpha = 0.1$) we see the heat flux term being close to zero throughout the whole flux surface because of the strong heat-flux limiter. Comparing the two terms to the sum of all remaining terms of the ion temperature equation shows that the two terms are not just small perturbations, but significant contributions.

A similar asymmetry in ion temperature was observed and described already in circular geometry by Zhu et al. [41] with the GDB code. In their simulations, a weak up-down

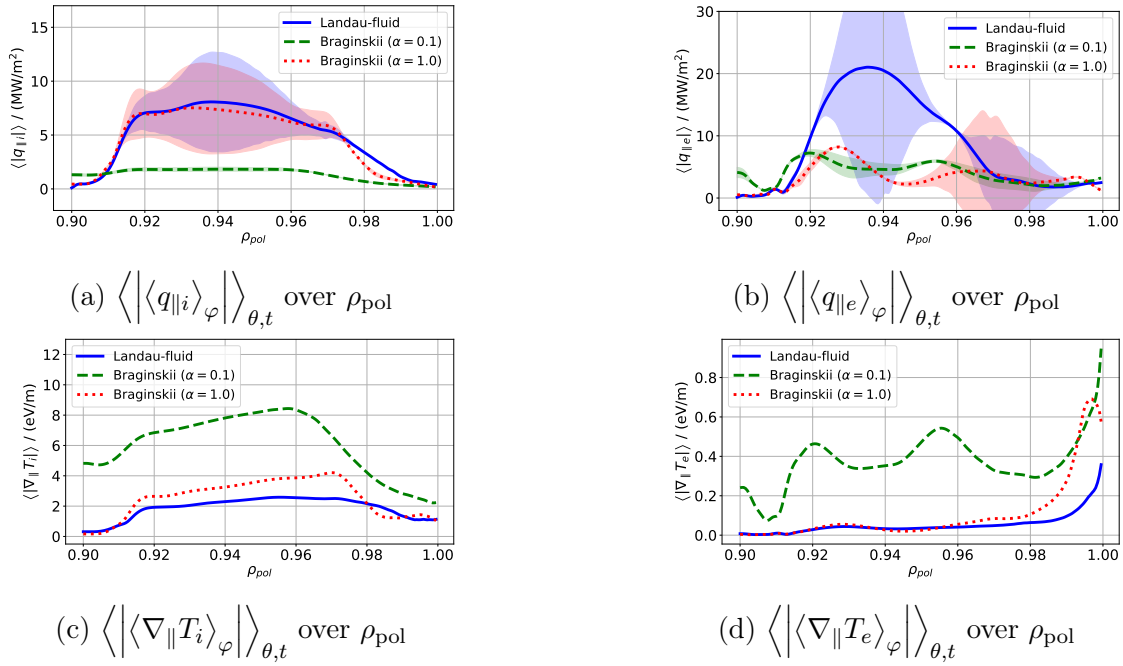

(a) $\left\langle \left| \langle q_{\parallel i} \rangle_{\varphi} \right| \right\rangle_{\theta,t}$ over ρ_{pol}

(b) $\left\langle \left| \langle q_{\parallel e} \rangle_{\varphi} \right| \right\rangle_{\theta,t}$ over ρ_{pol}

(c) $\left\langle \left| \langle \nabla_{\parallel} T_i \rangle_{\varphi} \right| \right\rangle_{\theta,t}$ over ρ_{pol}

(d) $\left\langle \left| \langle \nabla_{\parallel} T_e \rangle_{\varphi} \right| \right\rangle_{\theta,t}$ over ρ_{pol}

Figure 37: Flux-surface averaged absolute values of parallel heat fluxes and parallel temperature gradients over ρ_{pol} with fluctuation amplitudes for the parallel heat fluxes at $t = 2.5\,\mathrm{ms}$ averaged over $\Delta t = 100\,\mu\mathrm{s}$

asymmetry was observed in all quantities but the most prominent one in ion temperature. By turning off the parallel heat conduction the asymmetry got more pronounced, which can be understood as an extreme case in terms of heat-flux limiters by setting $\alpha = 0$."

5.4 Looking under the bonnet - Landau-fluid closure at work

"In the theory section, we have discussed already that the Landau-fluid closure employs higher numbered Lorentzians to represent the parallel heat flux as collisionality decreases. This correlation was found with a simple one-dimensional model. To investigate if this characteristic is also visible in a turbulence simulation, where temperature distributions along field lines are far more complex than a simple Gaussian, we plot the flux surface averaged absolute values of the individual Lorentzians $< | < q^{\mathrm{LF}}_{\parallel j,n} >_{\varphi} | >_{\theta,t}$ over ρ_{pol} in fig. 38. For electrons fig. 38a it is clearly observed how the number of the relevant Lorentzian is increasing with decreasing ρ_{pol}. This is perfectly in line with our expectation, since with decreasing ρ_{pol} the temperature is increasing and therefore the collisionality reduces. For ions, the same behaviour is visible although not as distinctly separated as for electrons. This method offers also a straightforward approach for testing if the number of Lorentzians used in the simulation is sufficient. If the ensemble of active Lorentzians would reach the highest number or even move out of the frame, the number of Lorentzians is insufficient for resolving the range of collisionality. Furthermore, two additional simulations were conducted with 3 and 12 Lorentzians to ensure the consistency of this heat-flux closure. For 3 Lorentzians we found that the simulation is indeed underresolved in terms of Lorentzians. In this case, a similar ion temperature asymmetry as for the Braginskii case ($\alpha = 0.1$) was observed, since the parallel ion heat flux is artificially

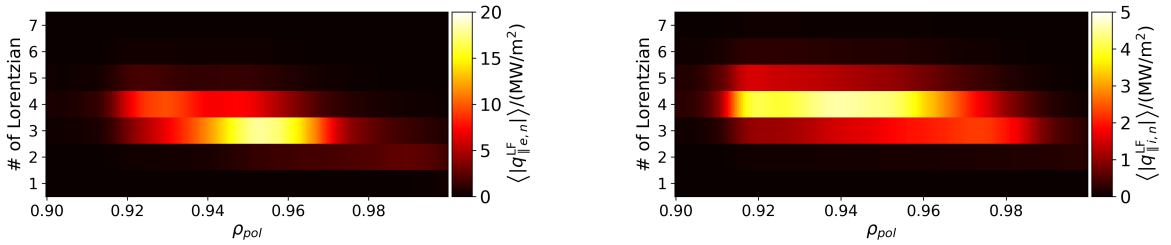

(a) For electrons (b) For ions

Figure 38: Flux-surface average of the absolute value of the single Lorentz functions for one snapshot at $t = 2.5\,\mathrm{ms}$

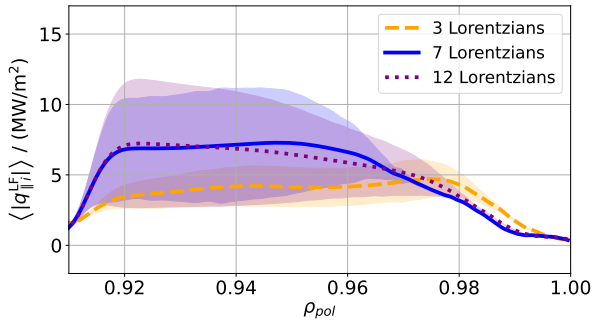

Figure 39: Flux-surface averaged absolute values of the parallel heat fluxes $< | < q_{\parallel i} >_{\varphi} | >_{\theta,t}$ over ρ_{pol} with fluctuation amplitudes at $t = 1.3\,\mathrm{ms}$ averaged over $\Delta t = 100\,\mu\mathrm{s}$

damped, see fig. 39, as there are no higher numbered Lorentzians to represent it.

This mechanism becomes evident from fig. 16a, where the parallel heat flux predicted by the Landau-fluid closure approaches zero for very low collisionality. The simulation with 12 Lorentzians does not show any major differences compared with the standard case with 7 Lorentz functions."

5.5 Non-local heat fluxes

"We want to investigate whether the non-local heat fluxes predicted for Landau-fluid closure in the one-dimensional setup (see fig. 21) are also relevant in a three-dimensional turbulence simulation. Further, we want to investigate if the effect of the Landau-fluid closure could be approximated for this case by an appropriate local closure.

First, we assume the Landau-fluid closure to be local and therefore proportional to a heat conductivity times a parallel temperature gradient. We calculate an effective heat conductivity

$$\tilde{\kappa}^{\mathrm{LF}}_{\parallel j} = -\frac{\left\langle q^{\mathrm{LF}}_{\parallel j} \right\rangle_{t,\varphi}}{\left\langle \nabla_{\parallel} T_j \right\rangle_{t,\varphi}}, \tag{137}$$

where $\langle f \rangle_{t,\varphi}$ is an average in time and toroidal direction on a test function f. This averaged effective heat conductivity is set equal to the flux-limited heat conductivity, which we get from eq. (63) divided by the parallel temperature gradient. By solving this

equation for the flux-limiting parameter we get an effective α^{LF}. The expression we find is

$$\alpha^{\mathrm{LF}} = \frac{1}{\kappa_{\|j}^{\mathrm{FS}}} \frac{\kappa_{\|j}^{\mathrm{BR}} \tilde{\kappa}_{\|j}^{\mathrm{LF}}}{\kappa_{\|j}^{\mathrm{BR}} - \tilde{\kappa}_{\|j}^{\mathrm{LF}}}, \tag{138}$$

which we have to interpret carefully. There are two cases in which α^{LF} is reaching excessively high absolute values. Firstly for $\kappa_{\|j}^{\mathrm{BR}} = \tilde{\kappa}_{\|j}^{\mathrm{LF}}$, which happens especially in the collisional SOL of our simulation and is no signature for non-local dynamics. Therefore, we restrict the domain for this analysis to the closed-field-line region.

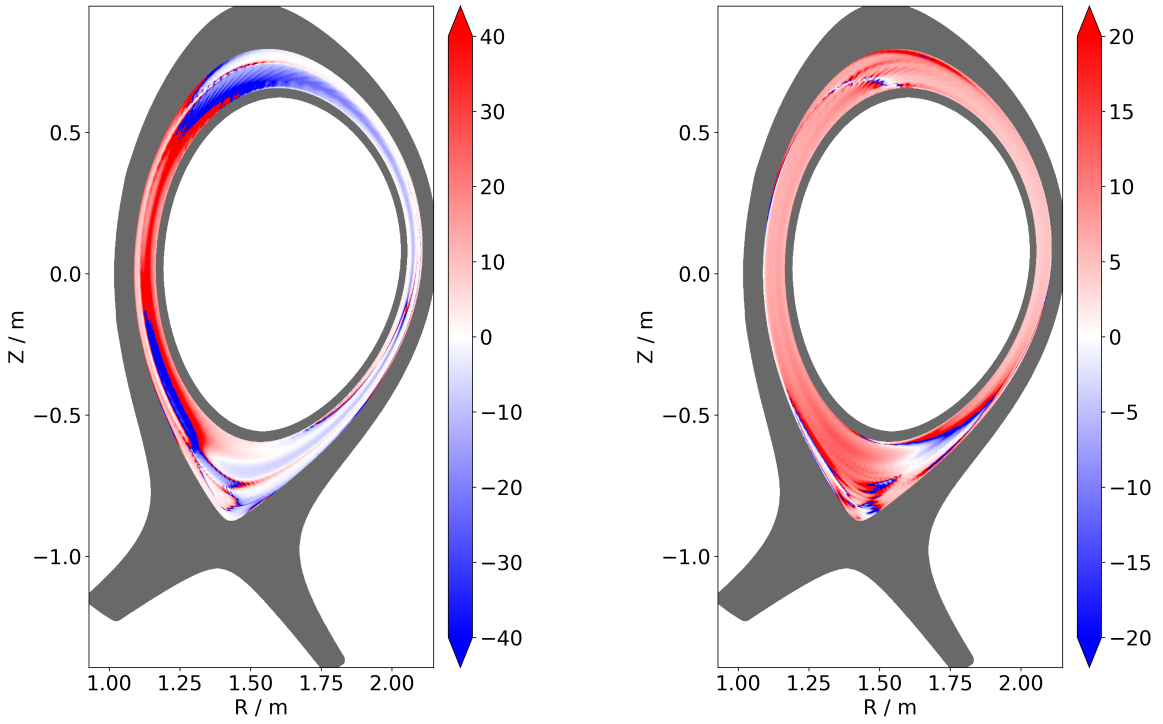

(a) For electrons

(b) For ions

Figure 40: Effective α^{LF} calculated according to eq. (138), calculated at $t = 2.5\,\mathrm{ms}$ and averaged over $\Delta t = 300\,\mu\mathrm{s}$

Further, we exclude the area near the core boundary since the temperature and density sources are active there. Secondly α^{LF} can reach high values when $\tilde{\kappa}_{\|j}^{\mathrm{LF}}$ itself becomes very large. This is the case we are interested in since it implies a non-locality as we observe a heat flux in the region of vanishing temperature gradients.

The calculated effective α^{LF} for electrons and ions is depicted in fig. 40. We have cut the colour scale since α^{LF} is reaching excessively high values in this region. The value of the cut is arbitrary and chosen here for visualisation reasons, but we want to denote that the values in the domains reach higher values ($\alpha_j^{\mathrm{LF}} > 1000$). For both electrons and ions, we find values for α^{LF} that are far beyond the usually used limit of $\alpha = 3$. This is strong evidence that the non-local behaviour of the Landau-fluid closure is not just academically relevant in simple one-dimensional cases (section 3) but also in non-linear edge turbulence simulations. The high values of α^{LF} also indicate that the parallel temperature gradients

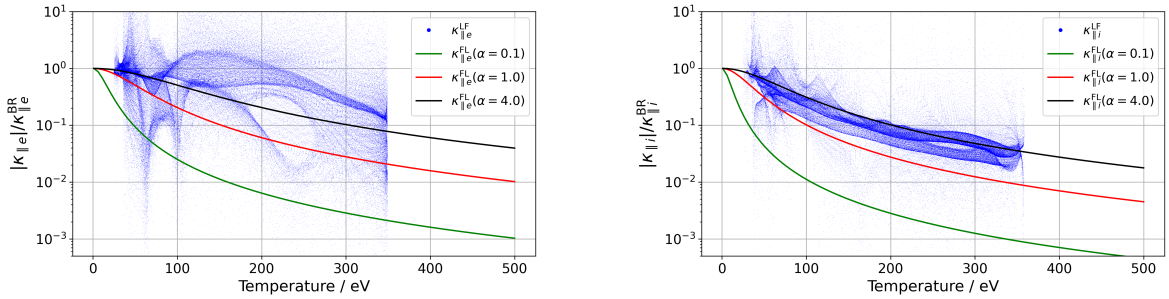

(a) For electrons (b) For ions

Figure 41: Absolute value of effective Landau-fluid heat conductivity point wise over corresponding temperature for the same spacial domain and time average as in fig. 40 and analytically calculated flux-limited heat conductivities, all normalised to $\kappa_{\parallel}^{\mathrm{BR}}$

are significantly smaller with the Landau-fluid closure than with the Braginskii closures, considering that the heat fluxes are of the same order of magnitude, see fig. 37. Further, it is interesting to note that α^{LF} also reaches negative values which implies that heat fluxes in those regions flow upwards the temperature gradient. This effect is by definition not possible for a local closure. The conclusion of constant flux-limiters in space and time being unable to represent non-local heat-flux models was drawn in Omotani et al. [85] (figure 4) for a one-dimensional time-dependent system already. However, we do not want to make estimations for relevant values of α to conduct simulations with a flux-limited closure, since this rather pragmatic comparison between local and non-local closures is not expected to work quantitatively. Detailed quantitative investigations of non-local heat-flux models in simpler geometries have been already conducted by e.g. Brodrick et al. [86]. We tried to investigate the Landau-fluid closure specifically for turbulence simulations.

Another way to visualise this behaviour of the Landau-fluid closure is by plotting the effective heat conductivity (eq. (137)) for every point in the domain in fig. 40 over the corresponding temperature in fig. 41. We can draw the same conclusion here, since the single points spread over an area they can not be described by an analytic regression function dependent on temperature as it is possible for the flux-limited expressions, especially for electrons."

5.6 Performance

"To give an impression on the computational cost, for the Landau-fluid simulation $3.8 \cdot 10^6$ time steps were performed for simulating well into the saturated state until 3.5 ms of physical time. This simulation was carried out on the MARCONI SKL partition from CINECA, employing 8 compute nodes with 48 cores each and took approximately 40 days, i.e. $3.7 \cdot 10^5$ CPUh in total.

As pointed out in Stegmeir et al. [80] parallel dynamics play a crucial role for code performance. From the computational perspective, the Landau-fluid and Braginskii model are very similar, as the implicit treatment of the Braginskii heat-flux term also results in an elliptic problem along magnetic field lines, similar to equations (128) and (129), which is solved with the same GMRES method from the PIM [79] library. The difference being,

	time per time step [s]	RHS [%]	2D solver [%]	3D solver [%]	others [%]
BR ($\alpha = 0.1$)	0.3909	28.3	36.7	23.1	11.9
BR ($\alpha = 1.0$)	0.3889	28.4	35.4	23.8	12.4
LF ($N = 3$)	0.4449	25.2	34.0	29.4 (22.6)	11.4
LF ($N = 7$)	0.5682	19.6	24.9	47.0 (41.5)	8.5
LF ($N = 12$)	0.7350	14.8	19.2	59.2 (54.8)	6.8

Table 4: Seconds per time step of GRILLIX and relative fraction for calculating the RHS of all equations, employing the 2D- and the 3D-solvers and for other parts of the code (MPI, auxiliary variables, etc.) for different heat flux closures. The value in brackets for the 3D solvers denotes the fraction consumed by the Landau-fluid closure.

that for the Braginskii model only one such elliptic problem has to be solved per species, whereas for the Landau-fluid model, N problems depend on the number of Lorentzians. Otherwise, we were able to use similar time-step sizes for all simulations.

For a direct performance comparison, we continued all five simulations for a few thousand time steps starting from the last stored point in time on 8 nodes of the RAVEN cluster, which employs Intel Xeon IceLake-SP 8360Y processors with 72 cores per node, from the Max Planck Computing and Data Facility. In table 4 the average duration for a single time step of the plasma model is given, which comprises evaluation of explicit terms (RHS), 2D elliptic solves for the electrostatic and parallel perturbed electromagnetic potential, and 3D field-aligned solves (where the necessary MPI communication is included) for the parallel heat fluxes and parallel momentum dissipation. As expected the Landau-Fluid model comes with an expense in computational time increasing with the number of Lorentzians. The increase of 46 % for 7 Lorentzians can be considered acceptable given the gained validity of the physical model and the removal of free parameters.

Finally, the bottleneck of the code shifts from the 2D solvers to the 3D solvers. While a lot of optimisation effort has already gone into the 2D elliptic solvers, for which even a GPU porting is currently ongoing, little work has been invested into the 3D solver so far, but only a naive GMRES algorithm with Jacobi preconditioning is employed. Therefore, a large span of optimisation is still possible, by employing more advanced algorithms, e.g. algebraic multigrid methods offered by the HYPRE [87] library that comes already with GPU support."

5.7 Connection between Landau-fluid closure and flux limiters

One further investigation was performed by employing a different averaging procedure for the effective heat conductivity in comparison to eq. (137), where an average in time and in toroidal direction was performed. Now we investigate the effective heat conductivity averaged in toroidal direction and over a flux-surface

$$\hat{\kappa}_{\parallel j}^{\mathrm{LF}} = -\frac{\left\langle |q_{\parallel j}^{\mathrm{LF}}| \right\rangle_{\theta,\varphi}}{\left\langle |\nabla_\parallel T_j| \right\rangle_{\theta,\varphi}}, \tag{139}$$

where we investigate the absolute values of the heat flux and the temperature gradient

here since a flux-surface average would annihilate the parallel gradient used in the denominator otherwise. The flux-surface average was evaluated at 200 equidistant flux surfaces within the closed-field line region of the simulation domain from $\rho_{\mathrm{pol}} = 0.9 - 0.9995$ with step width of $\Delta\rho_{\mathrm{pol}} = 0.0005$. We do not perform an average in time, but plot the values for different points in time and evaluate their spreading. The result of this analysis is plotted in fig. 42.

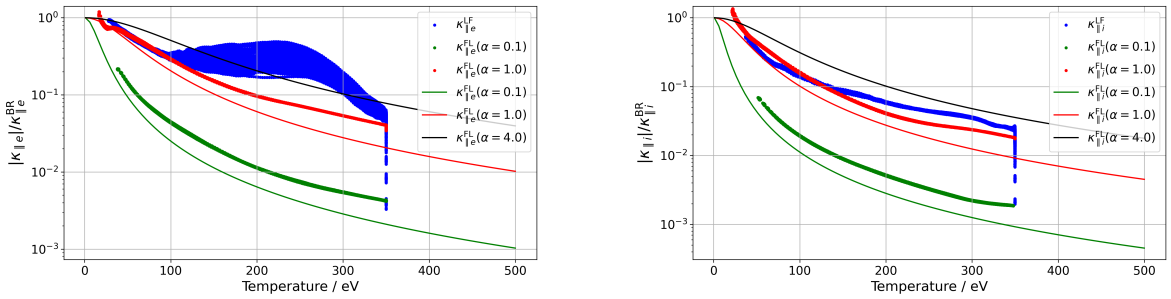

(a) For electrons (b) For ions

Figure 42: Effective Landau-fluid heat conductivity averaged in toroidal direction and over flux surfaces for the same time interval as in fig. 40, all values normalised to $\kappa_\parallel^{\mathrm{BR}}$

We find that the flux-limited expressions for both $\alpha = 0.1$ and $\alpha = 1.0$ correlate perfectly as expected, however, the analytical expressions (solid lines) are not matched exactly. The reason for this deviation is that for the analytical expressions the density is kept fixed to the normalisation value n_0. For the values extracted from the simulations, however, the density varies over ρ_{pol} (see fig. 34a). To verify, that the density variation is really the reason for the deviation, we keep the data for $\hat{\kappa}_{\parallel j}^{\mathrm{LF}}$ extracted from the simulations as they are, but for the analytical expressions we assume a density profile that varies linearly with temperature as $n(T_j) = n_0(1.5 + 0.1T_j)$. The data with density-corrected analytical expressions are shown in fig. 43, where we see excellent agreement between the data extracted from the simulation for the two Braginskii cases and the analytical expressions.

For the Landau-fluid closure, we find with this averaging procedure a very high correlation for ions and also a high correlation for electrons in comparison to the analysis shown in fig. 41. The electrons still show a larger spreading, which is in agreement with fig. 41a in comparison to fig. 41b. The Landau fluid data close to $T_j = 350\,\mathrm{eV}$ should not be taken seriously, as this is the region where temperature sources and buffer zones are active.

It makes sense, that the correlation of the effective heat conductivity is significantly larger after taking a flux-surface average, since the parallel direction in which the non-local behaviour of the Landau-fluid heat flux is showing up, is averaged out.

As pointed out by Zholobenko et al. [51] the free-streaming limited Braginskii heat flux eq. (63) can be derived from the Landau-fluid expression (eq. (89)), by approximating $k_\parallel \approx 1/(q_{95}R_0)$, $ik_\parallel T_{j,k} = \nabla_\parallel T_j$ and the flux-limiting parameter $\alpha = \sqrt{8/\pi}$ we find

$$-nv_{th,j}\sqrt{8/\pi}\frac{ik_\parallel}{|k_\parallel| + \delta_j/\lambda_{\mathrm{mfp}}}T_{j,k} \approx -\kappa_{\parallel,j}^{\mathrm{BR}}\left(1 + \frac{\kappa_{\parallel,j}^{\mathrm{BR}}}{\alpha n\sqrt{T_j/m_j}R_0 q_{95}}\right)^{-1}\nabla_\parallel T_j. \tag{140}$$

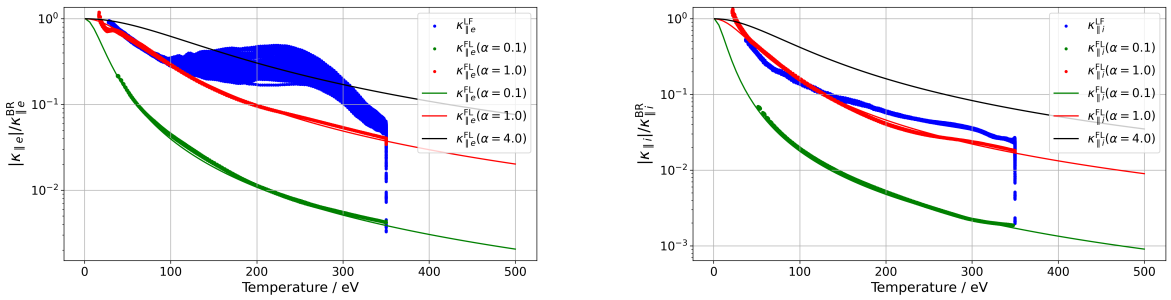

(a) For electrons (b) For ions

Figure 43: The same analysis as in fig. 42 with a density correction of the form $n(T_j) = n_0(1.5 + 0.1T_j)$

This indicated that for a suitable choice of the flux-limiting parameter α global transport behaves quite similarly between the flux-limited Braginskii closure and the Landau-fluid closure, which is indicated by the input power in table 3 and the density and temperature profiles in fig. 34. This observation is also confirmed by simulations GRILLIX in H-mode conditions [51]. The averaging method in eq. (139), might be used to give estimations on reasonable values for values of the flux-limiting parameter α.

It is emphasised that while global behaviour can be matched between the two closures, the dynamics along field lines are very different between the two closures. These dynamics are important for more intricate global phenomena such as zonal flows and geodesic acoustic modes and might explain the differences visible in the radial electric field of the three simulations fig. 34d.

5.8 Chapter summary

Within this chapter, we performed and analysed turbulence simulations in the geometry of ASDEX Upgrade. In a general comparison, the three cases behave similarly and the profiles are close to each other, except for the ion temperature in the case Braginskii ($\alpha = 0.1$), which links to an ion temperature asymmetry. The radial electric field for the Landau fluid case was significantly closer to the experimental measurements than the other two cases. An ion temperature asymmetry was found for the case Braginskii ($\alpha = 0.1$), which originates in the artificial small parallel heat fluxes due to the strong flux limiter and is explained in detail. The Landau fluid closure was investigated during the turbulence simulation. We found that with increasing temperature, i.e. dependent on the radial coordinate, higher-numbered Lorentzians carry the heat flux. Furthermore, we showed that a simulation employing only three Lorentzians would not be sufficient for this case. The non-local behaviour of the Landau-fluid closure was investigated, where we found that at single points in the simulation domain, the heat-flux deviates strongly from a local description, while averages over a flux surface agree better with local descriptions and comparisons with flux limiters are possible. Nevertheless, more intricate dynamics are very different between the two closures, as can be seen in the radial electric field. Lastly, the performance of the turbulence simulations was addressed, where we found a 46 % increase in computation time from the flux-limited Braginskii closure to the Landau-fluid closure.

6 GRILLIX simulations in the I-mode regime

6.1 The I-mode regime

The Improved-confinement mode (I-mode) [24] is a type-I ELM-free operational regime with significantly improved energy confinement time τ_E in comparison to the standard L-mode regime and low impurity accumulation. This makes the I-mode an attractive regime for future reactors.

In I-mode, the energy confinement is H-mode-like while the particle confinement is L-mode-like. This is also reflected in the density and temperature profiles. Profiles of the L-mode discharge # 36190, the I-mode discharge # 37980 and the H-mode discharge # 40411 are shown in fig. 44. It is commonly said that I-mode shows a pedestal in temperature but not in density. Looking at the I-mode density profile isolated in fig. 47, a steep-gradient region is visible here as well. However, this is not considered a pedestal compared to the H-mode pedestals. The temperature pedestal is even higher for the considered I-mode than for the H-mode, which is not necessarily the case.

It is considered that parallel heat fluxes play an important role in decoupling particle and heat transport [88]. Due to the absence of a transport barrier like in H-mode [89], the I-mode does not suffer from strong impurity accumulation. The operational window of the I-mode in terms of heating power opens up between L-mode and H-mode if the necessary input power to access H-mode is high enough. Therefore I-mode discharges are performed in unfavourable configuration, where the ion ∇B drift points away from the active X-point and the heating power required for accessing H-mode is higher than in favourable configuration, where the ion ∇B drift points towards the active X-point. The I-mode regime was observed in different machines, i.e. in Alcator C-mode [24], ASDEX Upgrade [52] and DIII-D [90]. While the L-mode regime is characterised by broadband turbulence, a prominent feature in I-mode turbulence is the so-called Weakly-Coherent Mode (WCM) [52, 88], which is observed in ASDEX Upgrade in the outer confined region $\rho_{\text{pol}} = 0.98 - 1.00$ with a frequency of $70 - 140\,\text{kHz}$. There are also challenges, e.g. for achieving detachment in I-mode [91].

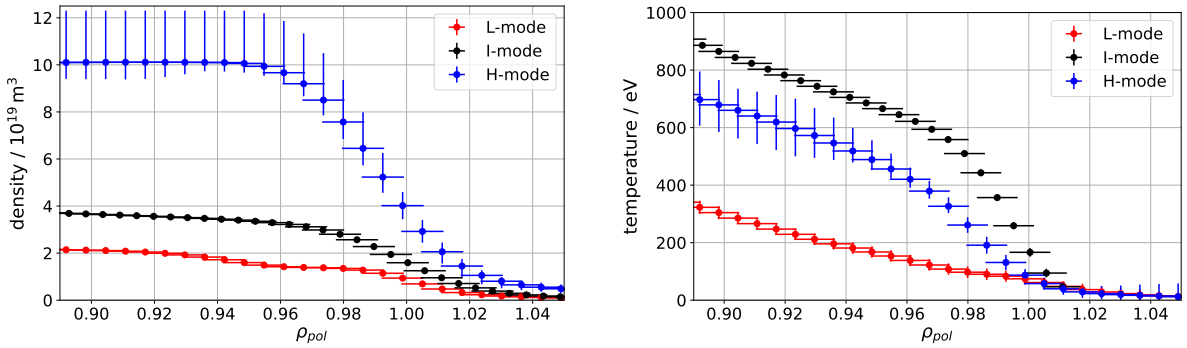

(a) Density profile

(b) Electron temperature profiles

Figure 44: Density and electron temperature profiles in L-mode (# 36190), I-mode (discharge #37980) and H-mode (discharge #40411)

Due to high temperatures and low densities in the edge region the collisionality in I-mode is rather low. To quantify this we plot also the calculated collisionality for the three experimental profiles in fig. 44 according to eq. (36). With the reference length chosen as $L_{ref} = q_{95} R_0 = 6.6\,\mathrm{m}$ we arrive at

$$\frac{L_{ref}}{\lambda_{\mathrm{mfp}}} \approx 6.86 \cdot 10^{-16} \, \frac{n_{\mathrm{exp}}}{T_{e,\mathrm{exp}}^2}, \tag{141}$$

with n_{exp} in m^{-3} and $T_{e,\mathrm{exp}}$ in eV. The calculated collisionality is plotted in fig. 45, where we observe that the collisionality in I-mode is nearly an order of magnitude lower over the whole closed-field-line region. Due to these low values of collisionality, the I-mode regime provides perfect conditions for testing the low-collisionality extension of the Landau-fluid closure.

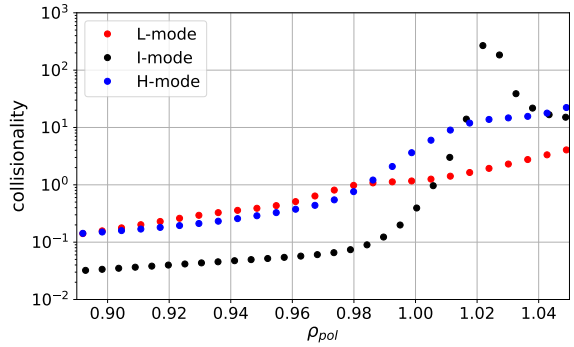

Figure 45: Collisionality calculated for profiles in L-mode (# 36190), I-mode (discharge #37980) and H-mode (discharge #40411) from fig. 44 according eq. (141).

6.2 Simulation setup

For the simulations with GRILLIX, we investigate the ASDEX Upgrade discharge #37980. This discharge starts in L-mode, accesses I-mode for a long stationary phase of several seconds and enters H-mode at the end of the discharge where the heating power is further increased. The simulation setup is taken from the stationary I-mode phase in the experiment at the time $t = 4.1\,\mathrm{s}$ within the discharge. The experiment was performed in upper single-null geometry and unfavourable configuration. The toroidal magnetic field has a strength of $B_{\mathrm{tor}} = 2.5\,\mathrm{T}$ on axis. The plasma was heated by electron cyclotron resonance heating and neutral beam injection. After subtracting the radiation losses, the total input power was ca. 1.9 MW in the experiment. The experimental density and electron temperature profiles can be seen in fig. 44, and the experimental ion temperature profile is shown in fig. 47c. The values at the inner core boundary of our simulation domain, which are maintained by adaptive sources at $\rho_{\mathrm{pol}} = 0.91$ are $n(\rho_{\mathrm{pol}} = 0.91) = 3.8 \times 10^{19}\,\mathrm{m}^{-3}$, $T_e(\rho_{\mathrm{pol}} = 0.91) = 800\,\mathrm{eV}$ and $T_i(\rho_{\mathrm{pol}} = 0.91) = 500\,\mathrm{eV}$.

The normalisation used for this simulation is precisely the same as for the L-mode simulations in section 5. A few model extensions are employed in these simulations compared to the last chapter. Instead of the one-moment neutrals model a more advanced

three-moment neutrals model is used here, involving the density, parallel velocity and temperature of the neutrals. This three-moment neutrals model will be discussed in detail in a separate publication in the near future. The fixed neutrals density at the divertor as a boundary condition, is still necessary and is chosen to be $1.0 \times 10^{18}\,\mathrm{m}^{-3}$. Two simulations are presented in the following, one performed with the Landau-fluid closure and one with the Braginskii closure and heat-flux limiters with a value of $\alpha_e = \alpha_i = 1.0$. Magnetic flutter is also incorporated in both simulations.

The I-mode regime is challenging for fluid models since the collisionality is rather low in the simulations domain due to high temperatures and low densities, as shown in fig. 45. Because of the low collisionality and the possible importance of parallel heat fluxes for this regime, the I-mode is an ideal test case for the low collisionality extension of the Landau-fluid closure. However, we still need to be careful when evaluating the simulation results, as we might encounter issues due to other fluid-closure terms. Deviations from the experimental results are also possible due to missing kinetic effects in the fluid model, that might be important for the I-mode regime, e.g Finite-Larmor-Radius (FLR) effects [88].

The computation time used for the Landau-fluid simulation for 5.2 ms of physical time on the MARCONI SKL partition from CINECA was approximately 3.5×10^5 CPUh, corresponding to a run time of 40 days. The computational cost is approximately the same as for the L-mode simulation in the last chapter, the increase in physical time is mainly due to a larger time step, which is possible due to the improved neutrals model. The computation time for the Braginsii simulations was about $30 - 40\%$ less.

6.3 Approaching the simulation

The simulation behaves very differently from the previous L-mode simulations. A time trace of the input power, required to keep the temperatures at the inner core boundary on its target value, is shown in the first panel of fig. 46. After the initial instability up to $t = 0.4\,\mathrm{ms}$, we find a quiescent phase interrupted by three peaks at $t = 1.75\,\mathrm{ms}$, $t = 3.25\,\mathrm{ms}$ and $t = 4.75\,\mathrm{ms}$ mainly in the electron heating power P_e. The axis here is truncated, the three peaks have maximum amplitudes of 32 MW, 23 MW and 22 MW. This behaviour differs greatly from the L-mode simulations in section 5, where we observed an initial instability followed by a successive convergence towards a quasi-stationary state in fig. 33.

A series of tests and investigations were performed to check if these bursts might be caused due to numerical issues. Until now they seem to be a persistent feature of these I-mode simulations performed with the Landau-fluid closure.

To gain further insights we investigate the OMP profile of several quantities over time, namely density, electron and ion temperature, radial electric field, perturbed magnetic field and parallel electron and ion heat fluxes. All quantities are shown in fig. 46. The peaks in heating power are visible in all plotted quantities, except for density and ion temperature, where just minor changes are observed. For further analysis, we first investigate the quasi-stationary phases in between the bursts and compare them to experimental measurements. Afterwards, we investigate the bursts in detail, where we will connect them with pedestal relaxation events (PREs) [53]. Therefore we will call the bursty events in the simulation PREs from in the following.

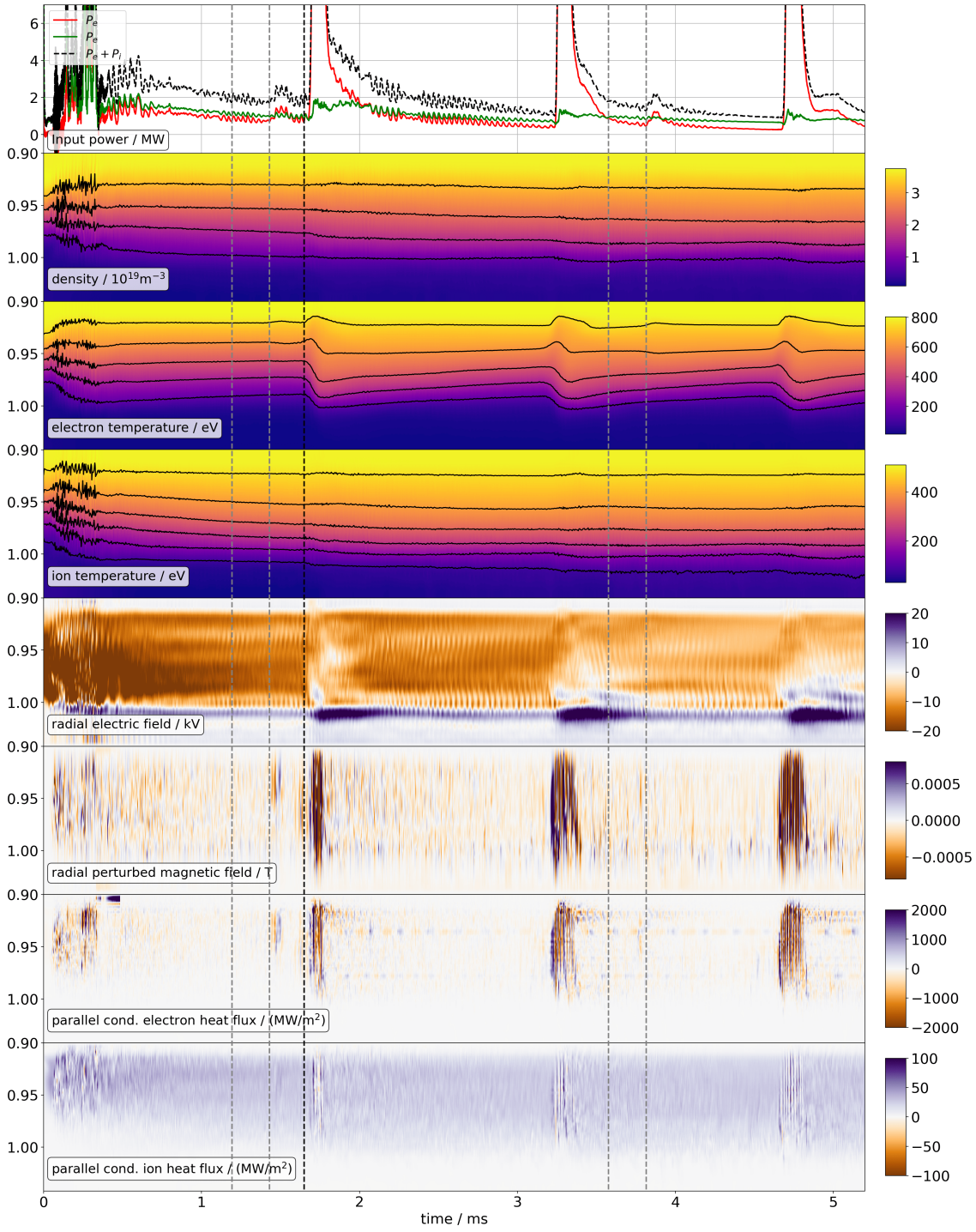

Figure 46: Heating power and OMP profile (y-axis in ρ_{pol}) for different quantities over time. The black dotted line marks the beginning of the first burst, and the two time intervals marked by grey dotted lines are used to calculate averaged profiles, which are shown in fig. 47

6.4 Analysis of quasi-stationary phases

6.4.1 General observations

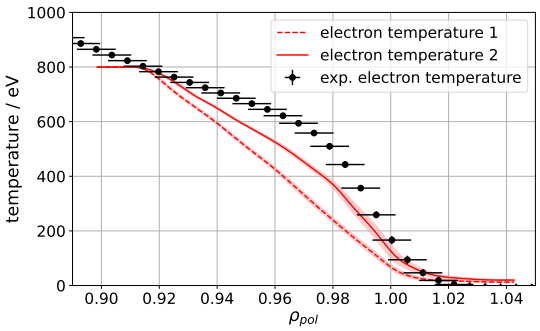

(a) Electron temperature profile

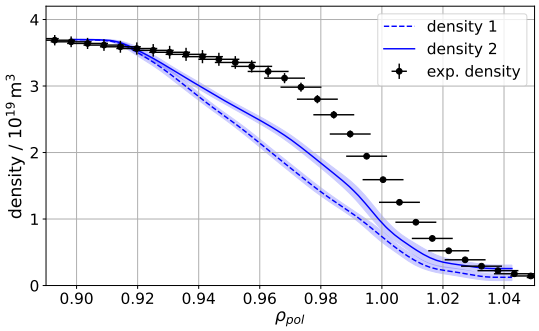

(b) Density profile

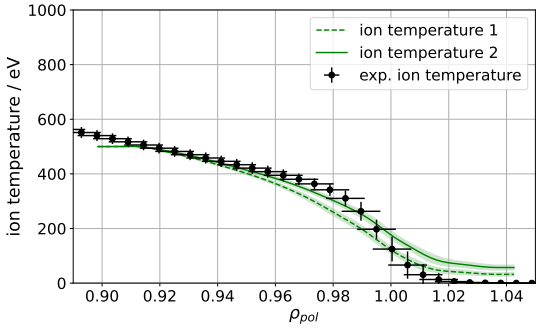

(c) Ion temperature profile

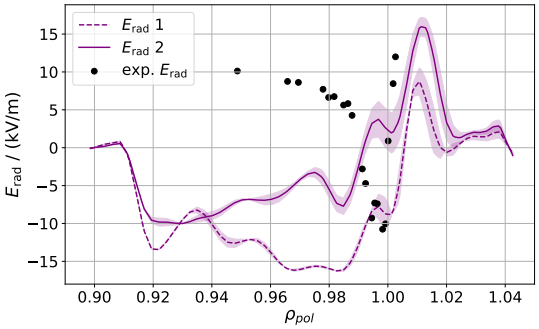

(d) Radial electric field profile

Figure 47: Density, electron temperature, ion temperature and radial electric field profiles for the first (1) time interval $t = 1.19 - 1.43$ ms and the second (2) time interval at $t = 3.58 - 3.81$ ms, each marked by a pair of grey lines in fig. 46

We compare profiles at two different time intervals within two different quasi-stationary phases. The two time intervals we picked are between $t = 1.19 - 1.43$ ms and $t = 3.58 - 3.81$ ms in fig. 47 to avoid the strong changes during the bursts. The two time intervals are also marked with grey lines in fig. 46. We observe that the profiles in the second time interval are considerably closer to the experimental values than in the first time interval, especially for the electron temperature. Looking again at the fig. 46, we observe in the electron temperature profile, that it relaxes again slightly until the third burst occurs.

6.4.2 The weakly-coherent mode

The weakly-coherent mode (WCM) is a key feature of the I-mode regime. However, it is not exclusively observed in I-mode but also less pronounced in L-mode. In experiments, the WCM is visible e.g. in the electron cyclotron emission signal or in reflectometry signals, where it is caused by edge density fluctuations [52, 92]. An example of a measurement of density fluctuations during different an I-mode discharge is shown in fig. 48.

A possible explanation for the WCM is, that the broadband turbulence, which is usually present in L-mode is damped at large scales due to phase randomisation and at

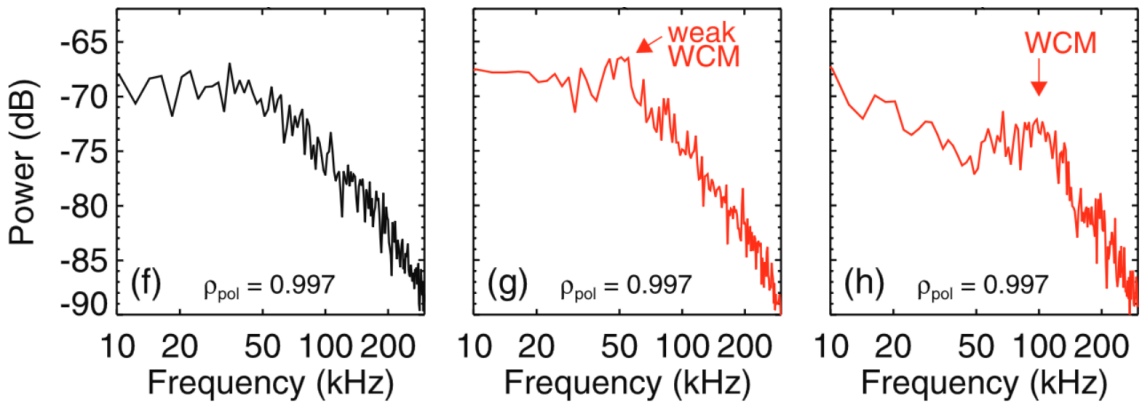

Figure 48: Measurements of a WCM during different stages of an I-mode discharge, where the WCM is not visible at first and becomes then more pronounced, taken from [52]

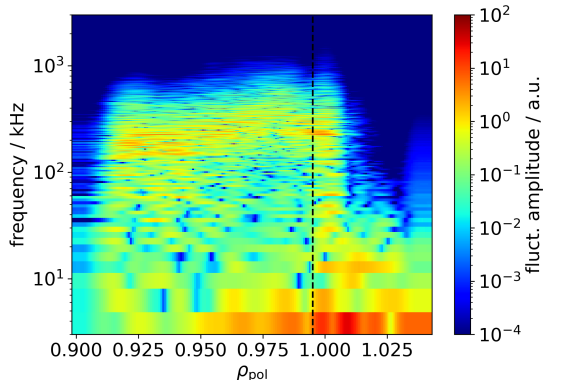

(a) Spectrum at $t = 0.95 - 1.27\,\text{ms}$

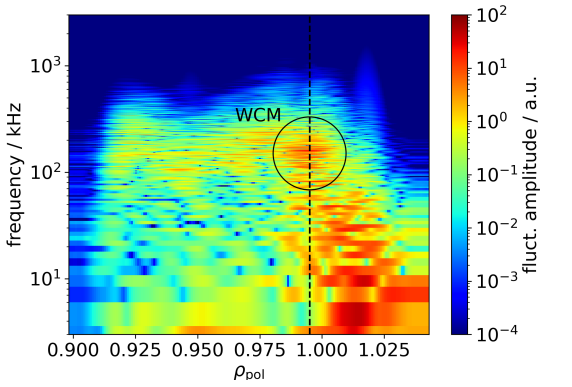

(b) Spectrum at $t = 3.82 - 4.23\,\text{ms}$

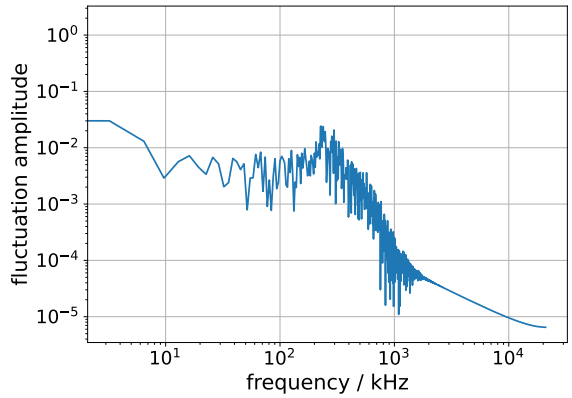

(c) Spectrum at $t = 0.95 - 1.27\,\text{ms}$ at $\rho_{\text{pol}} = 0.95$

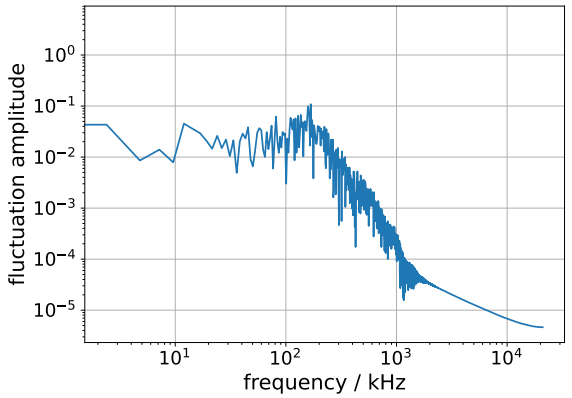

(d) Spectrum at $t = 3.82 - 4.23\,\text{ms}$ at $\rho_{\text{pol}} = 0.95$

Figure 49: Spectrum of density fluctuations before the first burst ($t = 0.95 - 1.27\,\text{ms}$) and after the second burst ($t = 3.82 - 4.23\,\text{ms}$), where a WCM is more pronounced and marked by a circle. Additional to the 2D colour maps, a cut at $\rho_{\text{pol}} = 0.995$ is plotted for easier comparison to fig. 48.

small scales due to FLR stabilisation [88]. The WCM would then be just the remainder of broadband turbulence at scales which are damped less efficiently. In ASDEX Upgrade in the outer confined region $\rho_{\text{pol}} = 0.98 - 1.00$ with a frequency of $70 - 140\,\text{kHz}$ [52, 88].

In the simulation, we investigate density fluctuations directly. We consider the time evolution of density at the OMP with a high temporal resolution of $\Delta t = 0.24\,\mu\text{s}$. The density signal $n(t)$ is Fourier transformed for each value of ρ_{pol}. The resulting spectra over frequency and ρ_{pol} are plotted in fig. 49 for similar time intervals as they were used to calculate the OMP profiles, i.e. $t = 0.95 - 1.27\,\text{ms}$ and $t = 3.82 - 4.23\,\text{ms}$. In comparison to OMP profiles, more data are necessary for calculating clear signals, therefore, the time intervals are longer than the ones used for the OMP profiles. The frequencies for all positions along the OMP are plotted colour-coded in figs. 49a and 49b and additionally as a curve similar to fig. 48 at the position $\rho_{\text{pol}} = 0.95$ in figs. 49c and 49d. In both time intervals, a structure similar to the WCM is found. The structure is spread over the whole closed field line region, especially for the first time interval, in comparison to the experiments, where the WCM is radially localised around $\rho_{\text{pol}} = 0.98 - 1.00$ [93, 52, 88]. For the second time interval in fig. 49b a more localised structure in the expected region is observed and marked by a circle.

The observed frequency $f \approx 200\,\text{kHz}$ is higher than the observed values in AUG of $f = 70 - 140\,\text{kHz}$. A possible explanation for this deviation is connected to the differences in the radial electric field E_r between simulation and experiment (see fig. 47d). The radial electric field is mainly responsible for the background rotation of the confined region. Since E_r is negative in our simulation the background rotation is in electron diamagnetic direction, while in the experiment the background rotation is in ion diamagnetic direction linked to a positive E_r in the confined region. The WCM propagates in electron diamagnetic direction [93] and propagates faster than the background rotation. Therefore, the background rotation would add up to the propagation speed of the wave and the measured frequency of the WCM in the lab frame is Doppler shifted to higher frequencies, in contrast to the experiment, where the measured frequency of the WCM is lower due to the background rotation in opposite direction. However, this argument does not apply to the position $\rho \approx 1.0$, where the radial electric field in the experiment is also negative.

An idea to match the background rotation is to adapt the boundary value of the parallel velocity at the inner core boundary. A rotation e.g. induced by NBI could be mimicked since the NBI heating is not intrinsically captured in GRILLIX, which might explain the deviations between the radial electric fields.

6.5 Pedestal relaxation events

Some I-mode discharges show so-called Pedestal Relaxation Events (PREs) [92, 53, 94], not to be confused with ELMs. PREs are not generally present in I-mode, but just if the I-mode is close to a transition into H-mode [53]. PREs tend to relax the pedestal, as the name suggests. They affect mainly the electron pressure profile and they show magnetic precursors [94]. However, during a PRE typically about 1% of the plasma stored energy is lost, which is much less than ca. 10% during Type-I ELMs [53]. The possible mechanism behind PREs was already assumed to be due to micro-tearing modes [94], although this was neither shown in experiments nor in simulations.

6.5.1 Micro-tearing modes

The small introduction on Micro-tearing modes (MTMs) is based on [28]. MTMs are electromagnetic modes, which are closely linked to their macroscopic relative, the neo-classical tearing mode. Since they are electromagnetic modes, they appear more likely in high confinement regimes due to the higher values of β. MTMs are driven by the electron temperature gradient and propagate in electron diamagnetic direction. They show tearing parity and show strong fluctuations in $A_\parallel$. MTMs increase mainly the radial transport of electron thermal energy [95]. The linear analytical dispersion relation for MTMs taken from [96, 97], reads

$$(\nu_e - 0.54i\omega)\,(\omega - \omega_{e*}) - 0.8\omega_{T*}\nu_e = 0, \tag{142}$$

with ν_e the electron collision frequency, $\omega_{e*} = k_\theta \rho_s c_s (1/L_n + 1/L_{Te})$ and $\omega_{T*} = k_\theta \rho_s c_s (1/L_{Te})$, the density gradient length $L_n = (\nabla n)/n$ and the electron temperature gradient length $L_{Te} = (\nabla T_e)/T_e$. In the original paper, k_y was used instead of k_θ due to a different coordinate system, but no significant difference is expected, since the two directions are nearly the same.

6.5.2 PREs in the simulation

We take another look at fig. 46. The black dotted line indicates the beginning of the first PRE, where the electron temperature profile starts to change significantly. The first precursors of this burst show up in the perturbed magnetic field and the parallel electron heat flux, where slightly increased amplitudes are visible shortly before the burst happens. This agrees well with the magnetic precursors of PREs in the experiment [94]. After the black dotted line strong changes in all quantities are observed, except for density and ion temperature, where just moderate changes occur.

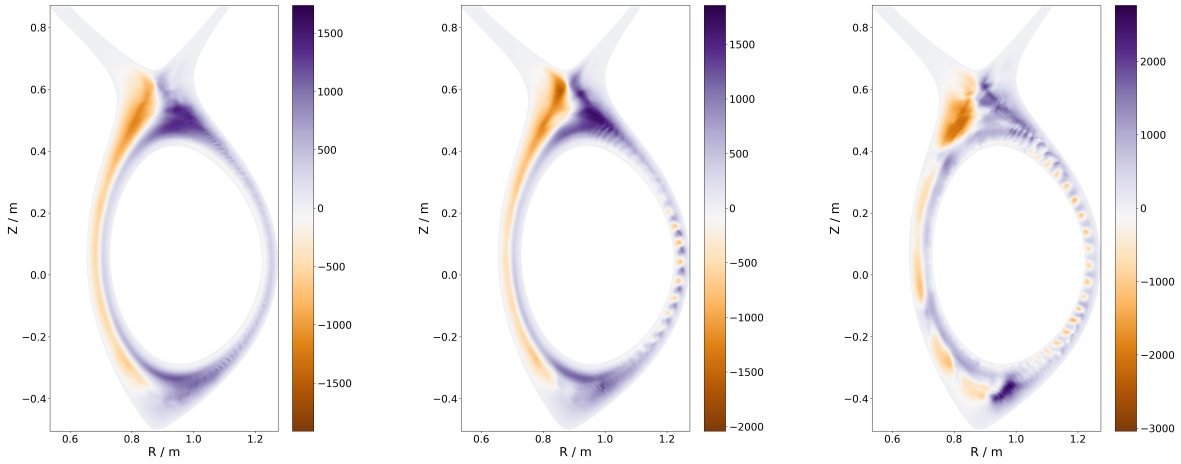

(a) $\tilde{A}_\parallel$ at $t = 3.05\,\mathrm{ms}$ (b) $\tilde{A}_\parallel$ at $t = 3.23\,\mathrm{ms}$ (c) $\tilde{A}_\parallel$ at $t = 3.29\,\mathrm{ms}$

Figure 50: Fluctuating $A_\parallel$ before, at the beginning of and during the first burst

This chain of events suggests that first the electron heat transport increases quite rapidly and thereafter the input power for electrons P_e is strongly increasing to keep the electron temperature at its target value.

A conceptual difference needs to be stated first: In experiments, it is observed, that a temperature pedestal builds up and relaxes in a small time interval of the order of 100 μs. In our simulation, on the other hand, the profiles do not show any pedestal in electron temperature in fig. 47a as dashed line before the first burst occurred. After the first burst and even more after the second one, plotted as solid line, the profiles are considerably closer to the experimental profiles. The major difference between experiment and simulation in this regard is that in the experiment the plasma is heated with constant power, while in the simulation an adaptive temperature source is employed, which leads to a time-varying power input (see fig. 46). Therefore, the source will change its value only if the radial transport in the system changes. Nevertheless, the underlying mechanism leading to the PREs in the simulation agrees very well with experimental observations.

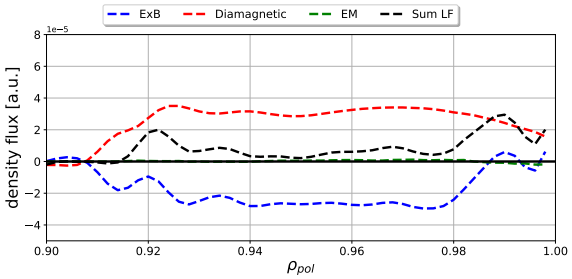

(a) Density flux before the burst

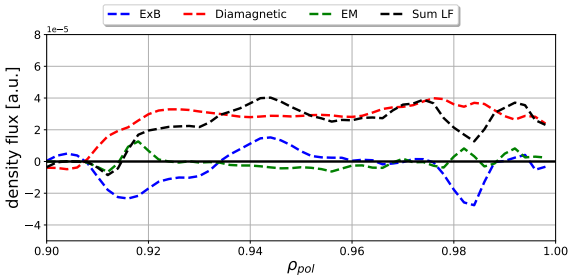

(b) Density flux during the burst

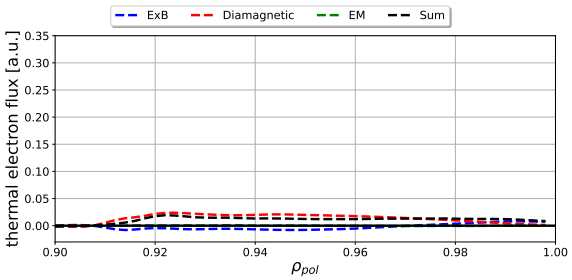

(c) Thermal electron flux before the burst

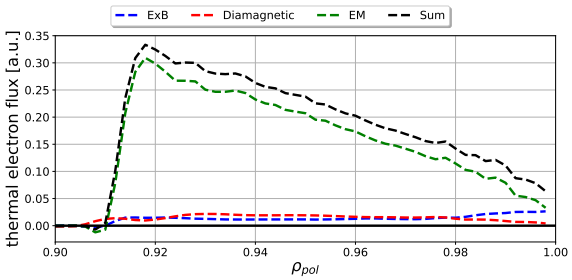

(d) Thermal electron flux during the burst

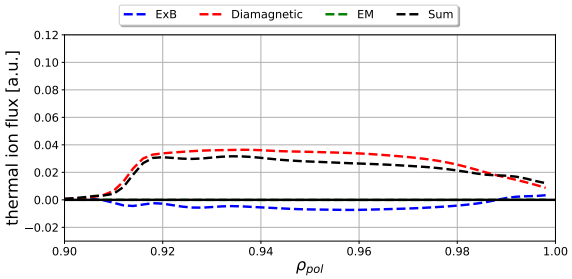

(e) Thermal ion flux before the burst

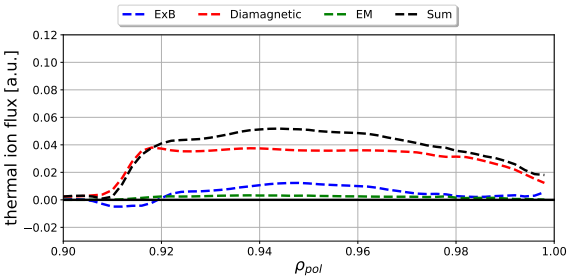

(f) Thermal ion flux during the burst

Figure 51: Radial transport for density, electron and ion temperature before ($t = 2.81 - 2.93$ ms) and during the burst ($t = 3.29 - 3.41$ ms)

Motivated by the magnetic precursors to the PRE in our simulation, we investigate the perturbed parallel magnetic vector potential $\tilde{A}_\parallel$. The perpendicular perturbed magnetic field is derived from $\tilde{A}_\parallel$ via $\tilde{B}_\perp = \nabla \times \tilde{A}_\parallel$. We plot $\tilde{A}_\parallel$ at three points in time in fig. 50, before ($t = 3.05\,\mathrm{ms}$), at the begin ($t = 3.23\,\mathrm{ms}$) and during the second burst ($t = 3.29\,\mathrm{ms}$).

In comparison to the time point before the burst $\tilde{A}_\parallel$ shows at the beginning of the burst a coherent structure at the low-field side, which becomes more pronounced during the crash. This is the first hint of an electromagnetic mode present in the system. Next, we directly compare the radial transport before and during the crash in fig. 51. The radial particle flux and the flux of ion thermal energy are mildly changed mainly due to a change in the $E \times B$-transport. However, the main difference is found in the radial flux of electron thermal energy, shown in fig. 51c and fig. 51d. The flux of electron thermal energy is increased strongly due to electromagnetic transport. This increase in the electron thermal transport is in line with an MTM as dominant instability.

To gain insights into the temporal evolution of the bursts, a spectrogram of electron temperature fluctuations is calculated for the flux surface at $\rho_{\mathrm{pol}} = 0.95$ in fig. 52.

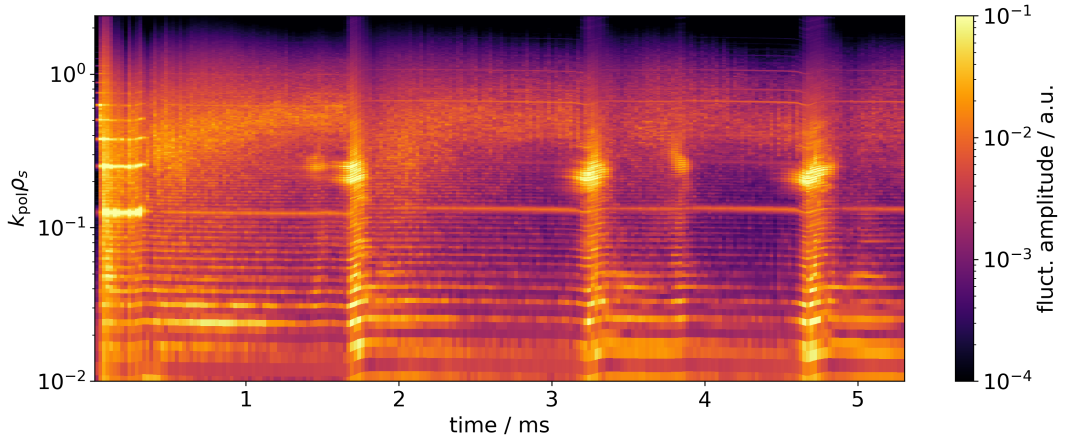

Figure 52: Spectrogram of electron temperature fluctuations at the flux surface $\rho_{\mathrm{pol}} = 0.95$

We observe that before all three bursts, which are clearly visible in the spectrogram, a mode starts to grow with at $k_{\mathrm{pol}}\rho_s \approx 0.2$. This mode appears as a precursor and leads to the burst event. Additional to the three bursts two smaller events are visible in the spectrogram at $t \approx 1.5\,\mathrm{ms}$ and $t \approx 3.8\,\mathrm{ms}$. These two events are also visible in the input power in the top panel of fig. 46, where the P_e is larger than P_i for a short time. The smaller events seem to be closely connected to the PREs, but too small to lead to a relaxation of the pedestal. The band with higher amplitude around $k_{\mathrm{pol}}\rho_s \approx 0.5$ is probably the WCM which is also visible in the spectrogram.

To find a waterproof argument, we calculate the dispersion relation of the underlying mode during the second PRE between $t = 3.2187 - 3.3617\,\mathrm{ms}$ for the flux surface at $\rho_{\mathrm{pol}} = 0.95$, where the background $E \times B$-rotation is calculated and subtracted. The result of this analysis is shown in fig. 53. Here we can see clearly, that the mode propagates in electron diamagnetic direction. Furthermore, we observe that our mode matches the linear dispersion relation for MTMs eq. (142) very well. The second analytical dispersion relation plotted in red is for resistive ballooning modes and can be considered as an upper

bound for resistive MHD modes according to [98]. The observed mode has a significantly higher propagation velocity than resistive MHD modes.

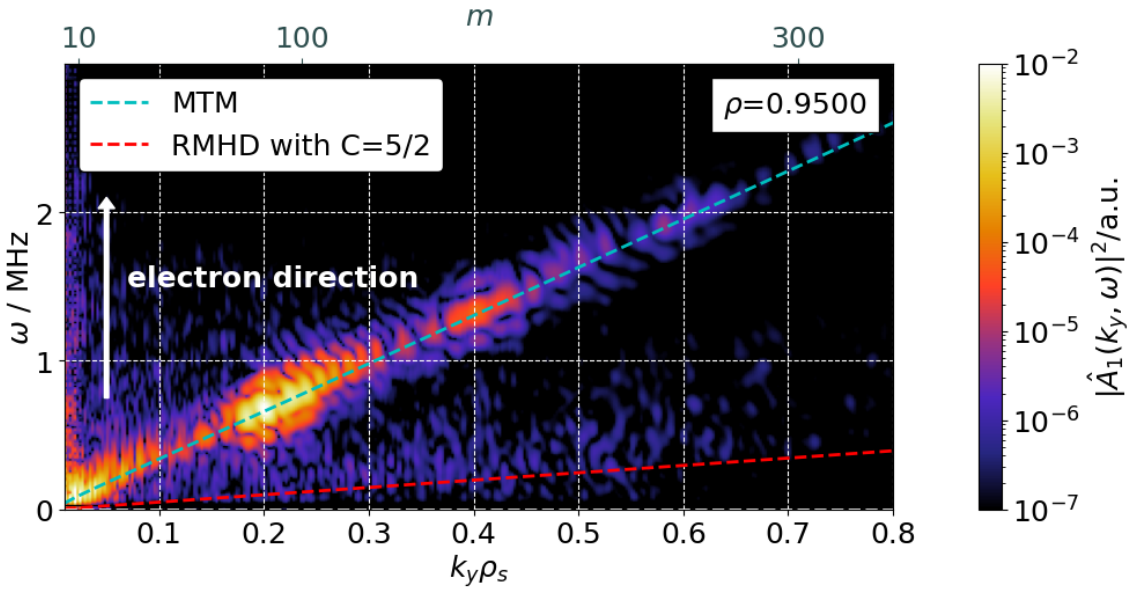

Figure 53: Dispersion relation of $A_\parallel$ for the mode present during the PRE, where an excellent agreement to the linear dispersion relation is observed

A further quantity investigated is the parallel electric field, which should be large for MTMs and can be quantified via

$$\hat{E}_\parallel = \frac{\int \left|-\partial_\parallel \phi + i\omega A_\parallel\right| \mathrm{d}x_\parallel}{\int \left|\partial_\parallel \phi\right| \mathrm{d}x_\parallel + \int \left|i\omega A_\parallel\right| \mathrm{d}x_\parallel}, \tag{143}$$

with $x_\parallel$ the parallel coordinate, according to [99]. Usually $\hat{E}_\parallel < 0.1$ for KBMs, during the bursts present in the simulations we achieve values of up to $\hat{E} \approx 0.9$.

Lastly, we investigate the parity of fluctuations of the electrostatic potential ϕ and the parallel magnetic vector potential $A_\parallel$ along a flux surface with $\rho_{\mathrm{pol}} = 0.95$. Explicitly we calculate

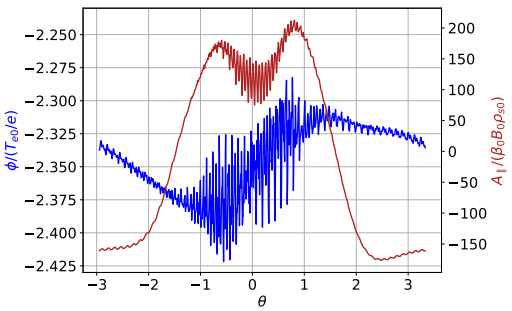

(a) In I-mode during a burst

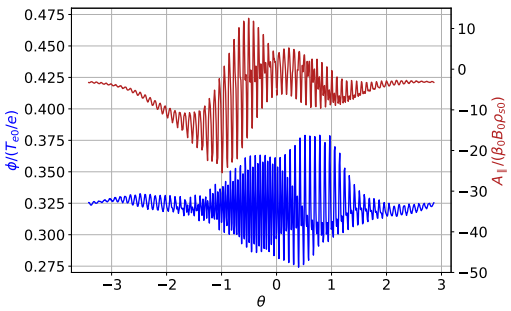

(b) In L-mode

Figure 54: Parity of ϕ and $A_\parallel$ during a burst in I-mode and as a reference in L-mode

$$\langle \phi(t_0) - \langle \phi \rangle_t \rangle_\varphi \quad \text{and} \quad \left\langle A_\parallel(t_0) - \left\langle A_\parallel \right\rangle_t \right\rangle_\varphi , \tag{144}$$

with $t_0 = 3.2187\,\text{ms}$ and the time average over $t = 3.2187 - 3.3617\text{ms}$. The mean is subtracted to get rid of the background of the quantities, this is also necessary for ϕ, since in our turbulence simulations it is no perfect flux-surface function, but shows a small up-down asymmetry. The resulting plot is shown in fig. 54. We find in the PREs that ϕ is an odd function, while $A_\parallel$ is an even function. This configuration is called tearing parity and is typical for MTMs. As a consistency check, the same analysis was performed for the L-mode simulation from the last chapter. Here we find the opposite configuration called ballooning parity, i.e. ϕ is an even function, while $A_\parallel$ is an odd function.

With all investigations and indications presented within this chapter, we can conclude, that the mode which is responsible for the PREs in our simulation is an MTM. For the very last plot of this chapter, we made a 3D visualisation of the MTM visible in the fluctuating parallel vector potential $\tilde{A}_\parallel$ in fig. 55.

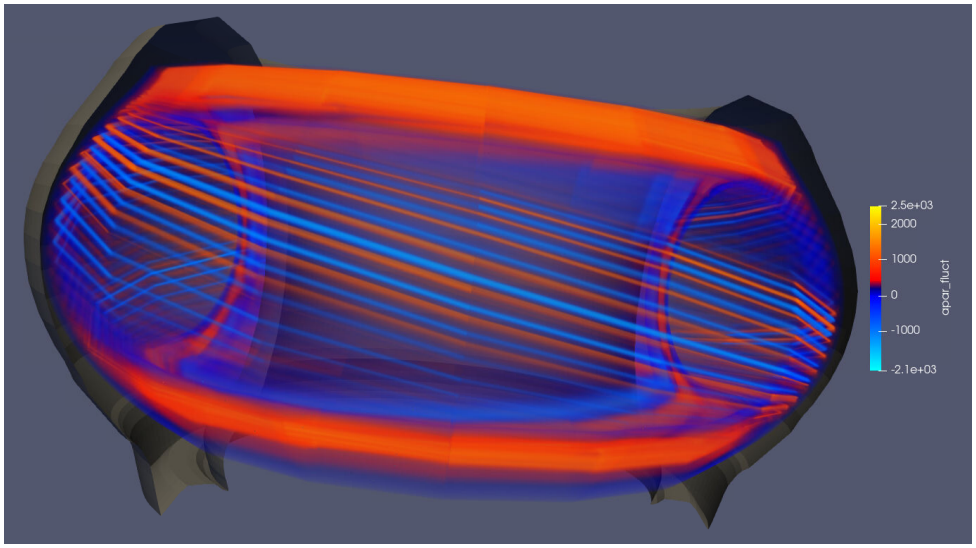

Figure 55: 3D visualisation of $\tilde{A}_\parallel$ during a PRE

6.6 The role of the heat-flux model

In this part, we want to emphasise the importance of the employed heat-flux mode for modelling plasma edge turbulence accurately.

6.6.1 Landau-fluid heat conductivity

We check how the heat Landau-fluid heat conductivity behaves during the simulation. Therefore we perform the same analysis as for the L-mode simulation and calculate the effective heat conductivity for the Landau-fluid closure. The data were averaged over a time interval of $t = 4.172 - 4.292$ms, which should be a relative quiescent phase between two bursts.

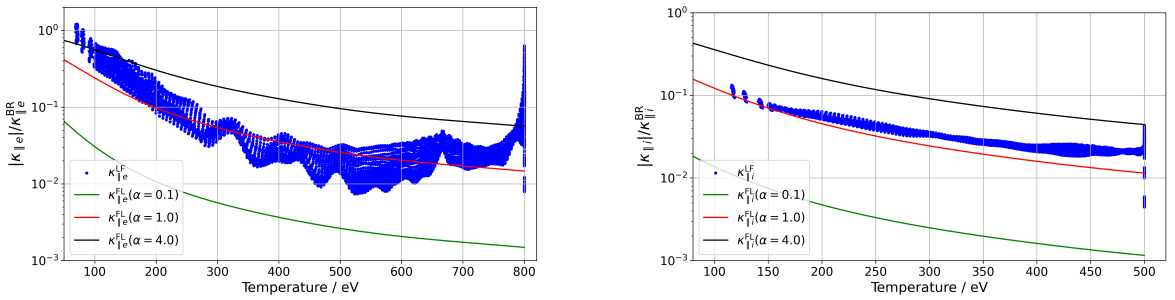

(a) For electrons (b) For ions

Figure 56: Effective Landau-fluid heat conductivity averaged in toroidal direction and over flux surfaces for the time interval $t = 4.172 - 4.292$ms, all values normalised to $\kappa^{BR}_{\parallel}$

In this analysis, we incorporated the accurate density profile for the flux-limited expressions in comparison to the analysis in the last chapter. Therefore the averaged density for each value of ρ_{pol} is connected to the corresponding averaged ion and electron temperature. The density as a function of temperature is then fitted via a polynomial regression, this regression formula is used for the density in the formula for the flux-limited heat flux.

We find again that electrons show a larger scatter than ions. The scatter here is partly due to the simulation being not in a steady state even between two bursts. Overall the data agree quite well with a value of $\alpha = 1.0$, in comparison to the lines at $\alpha = 0.1$ and $\alpha = 4$. Although we see for ions a deviation for high temperatures, where the Landau-fluid model would suggest a value of $\alpha \approx 2.0$. For electrons, we see higher values for $\kappa^{LF}_{\parallel e}$ for the highest and lowest temperatures present, but $\alpha = 1.0$ is still in reasonable agreement with most of the data.

6.6.2 Braginskii closure with heat-flux limiters

A second simulation was performed with the same setup but with the Braginskii closure and heat-flux limiters with values of $\alpha_e = \alpha_i = 1.0$ for electrons and ions. In fig. 57 the time trace of power is shown as well as the flux-surface averaged values of density, electron and ion temperature at $\rho_{\text{pol}} = 0.998$. In the time traces no burst events are observed as they were present in the Landau-fluid simulations, instead, the simulation is quiescent and converging towards a steady state. Profiles at the OMP can be seen in fig. 58 for the time interval $t = 4.768 - 4.888$ ms, which is also indicated by grey lines in fig. 57.

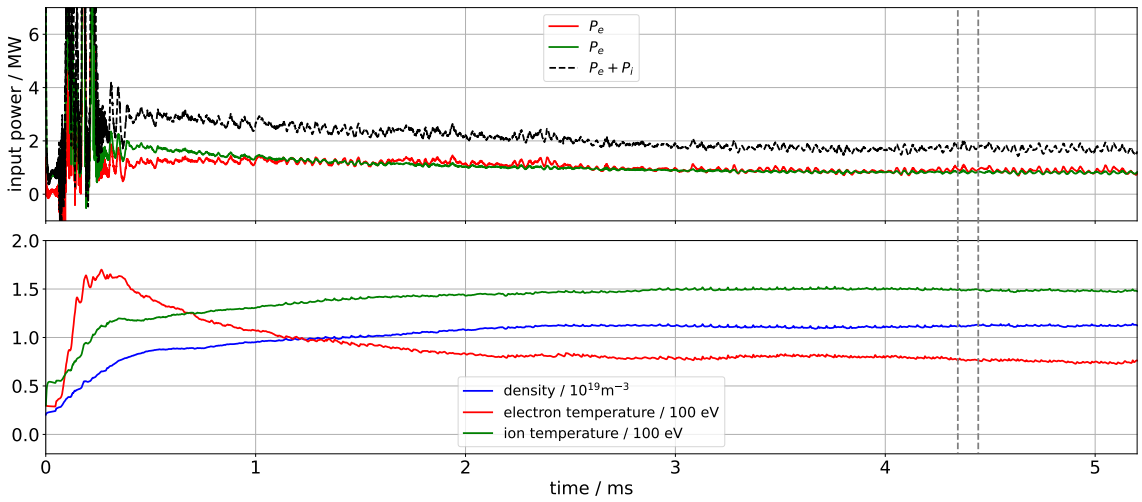

Figure 57: Input power and flux surface average at $\rho_{\text{pol}} = 0.998$ of density, electron and ion temperature over time

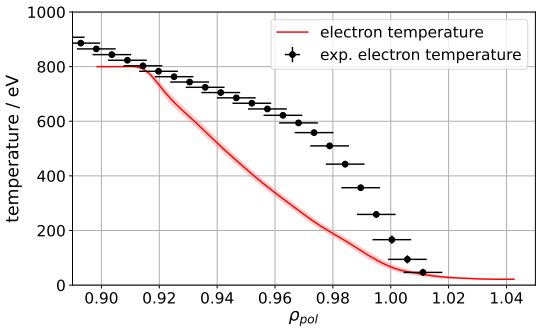

(a) Electron temperature profile

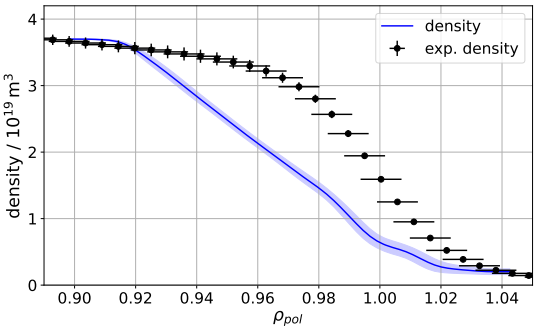

(b) Density profile

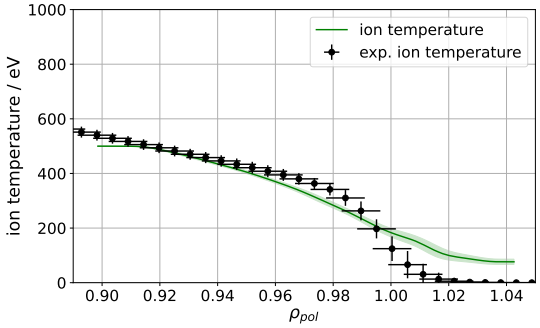

(c) Ion temperature profile

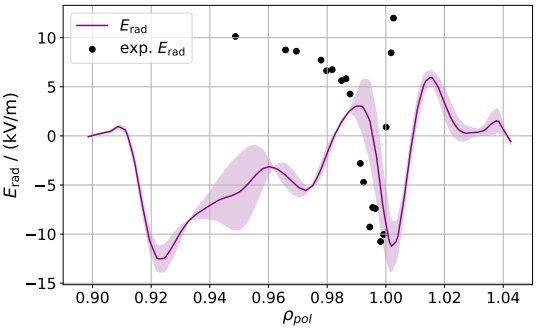

(d) Radial electric field profile

Figure 58: Density, electron temperature, ion temperature and radial electric field profiles for the time interval $t = 4.768 - 4.888$ ms

We observe especially in the electron and ion temperature profile that no pedestal is present and the simulation results are far off from the experimental measurements. In fact, the profiles tend more towards a strongly heated L-mode, instead of an I-mode. To find the exact reason for the absence of the bursts in comparison to the Landau-fluid simulations more investigations are necessary. For now, we can just state this fact due to

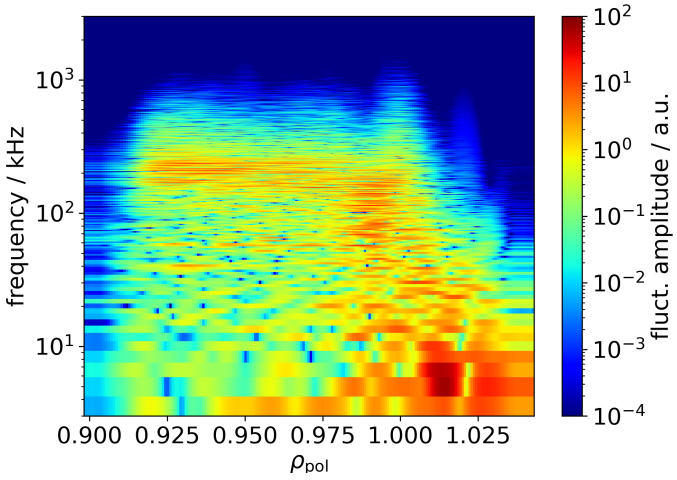

Figure 59: Spectrum of density fluctuations in the time interval $t = 1.907 - 2.403\,\mathrm{ms}$

observations in the two simulations.

We calculate a density fluctuation spectrum for the time interval $t = 1.907 - 2.403\,\mathrm{ms}$ in fig. 59, for comparing to the spectra shown for the Landau-fluid simulations. We observe that there are increased fluctuation amplitudes at ca. 200 kHz over the whole closed field line region ($\rho_{\mathrm{pol}} < 1.0$), except for the inner region at $\rho_{\mathrm{pol}} < 0.91$, where buffer regions and sources are active. This matches qualitatively with fig. 49a, the large radial extend is more visible for the limited Braginskii case.

6.6.3 Removal of heat-flux limiters

We perform an artificial test with the Braginskii closure, which should be considered as an academic test case. The simulation shown in the last section was continued and the heat-flux limiters α_e and α_i were removed, i.e. the original Braginskii closure [43] was used, which predicts parallel heat fluxes of significantly greater amplitude.

The evolution of profiles can be seen in fig. 60, where the black dotted line marks the point, where the heat-flux limiters were removed. The parallel heat fluxes increase strongly as expected and the temperature profiles develop a pedestal, most pronounced in electron temperature. After saturation in this new state of the system at $t \approx 4\,\mathrm{ms}$, even the total input power of $P \approx 2.2\,\mathrm{MW}$ is in reasonable agreement with the experimental value of 1.9 MW.

The profiles in steady state without heat-flux limiters at $t = 4.530 - 4.768\,\mathrm{ms}$ are shown in fig. 61. The two temperature profiles are in excellent agreement with the experimental data, whereas the density and radial electric field are also close to the experimental measurements.

This academic test illustrates nicely the importance of the correct treatment of parallel heat fluxes for simulations of the I-mode regime, but also for edge fluid turbulence simulations in general. Furthermore, this indicates, that radial particle and heat transport can be decoupled due to parallel heat conduction, if the parallel heat conductivity is high enough.

The mechanism which leads to the difference in the profiles with and without heat-flux

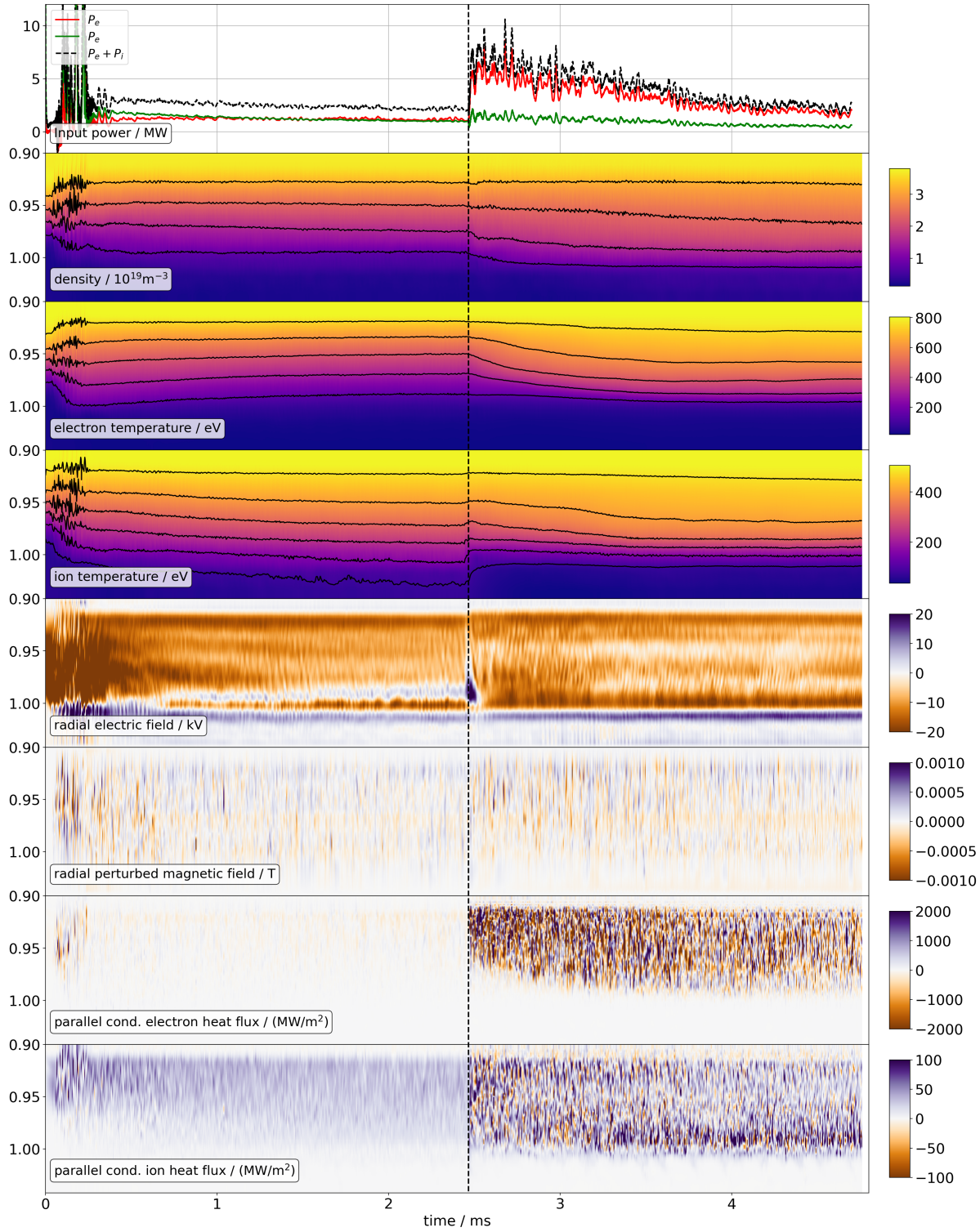

Figure 60: Heating power and OMP profile (y-axis in ρ_{pol}) for different quantities over time. The black dotted line marks the point, where the heat-flux limiters were removed

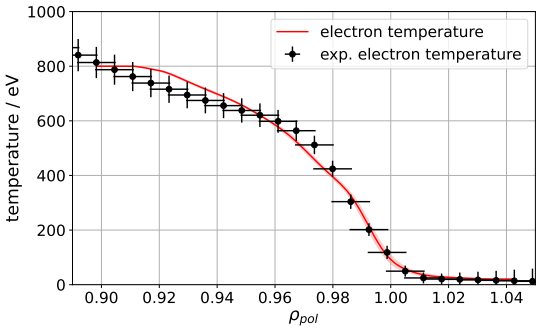

(a) Electron temperature profile

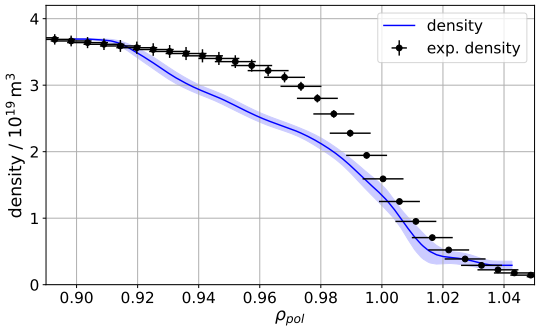

(b) Density profile

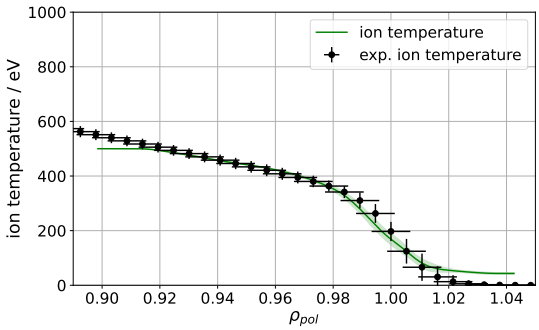

(c) Ion temperature profile

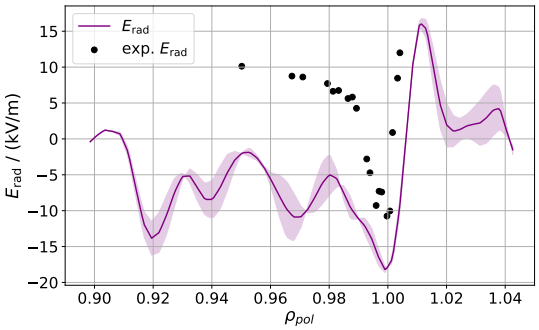

(d) Radial electric field profile

Figure 61: Density, electron temperature, ion temperature and radial electric field profiles for the Braginskii closure without heat-flux limiters for $t = 4.530 - 4.768\,\text{ms}$

limiters can be understood by investigating the fluctuation amplitudes σ for both cases. The fluctuation amplitudes are plotted in fig. 62 for the case with heat-flux limiters ($t = 2.146 - 2.384\,\text{ms}$) in solid lines and without limiters ($t = 4.530 - 4.768\,\text{ms}$) in dashed lines. In the fluctuation amplitudes of electron and ion temperature, we see a strong reduction due to the missing heat-flux limiters. Larger parallel heat fluxes damp decrease the temperature fluctuation amplitudes, and smaller fluctuation amplitudes in temperature correlate with less radial heat transport and steeper temperature gradients in the profiles. However, we want to emphasise, that the pure Braginskii closure is not valid in the present range of collisionality. Therefore this section needs to be understood as an academic test case.

For the sake of completeness, we also plot the density fluctuation spectrum for the Braginskii closure without heat-flux limiters. The spectrum for the time interval $t = 4.053 - 4.768\,\text{ms}$ is shown in fig. 63. We observe smaller fluctuation amplitudes in comparison to the previous cases, especially for high frequencies ($f > 40\,\text{kHz}$). In fig. 63 we do not find indications for a WCM, which confirms that this academic test case reproduces the experimental profiles by accident and not by capturing the underlying physics present in the experiments. Nevertheless, the simulation without heat-flux limiters illustrates how important parallel heat fluxes and their accurate description are for modelling plasma turbulence with fluid models.

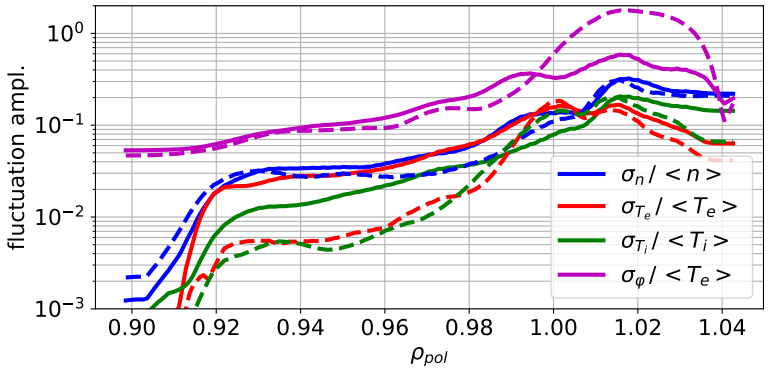

Figure 62: Fluctuation amplitudes for the time interval $t = 2.146 - 2.384$ ms with heat-flux limiters (solid lines) and $t = 4.530 - 4.768$ ms without heat-flux limiters (dashed lines)

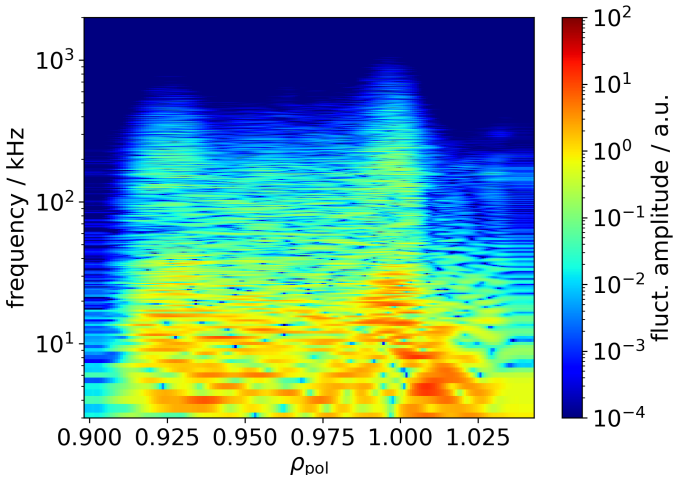

Figure 63: Spectrum of density fluctuations in the time interval $t = 4.053 - 4.768$ ms

6.7 Chapter summary and outlook

Within this chapter, an attempt to simulate the I-mode regime with the extended plasma fluid model of GRILLIX was undertaken. The simulations were expected to be challenging due to the low collisionality of the I-mode regime. Although no stationary I-mode could be simulated, many features of an I-mode in experiments were visible in the simulation data, e.g. the profiles were not far off the experimental ones, traces of a WCM were visible and PREs were observed. A perfect match with the profiles was not expected, since in the experiment, there are no PREs present. Furthermore, a detailed analysis of the observed PREs revealed that we could pinpoint the underlying microinstability with confidence to be an MTM. Finally, we highlighted the importance of the employed heat flux model. Simulations with a limited Braginskii closure reached from an overheated L-mode up to profiles close to the experimental ones depending on the flux-limiting parameter α. However, despite the matching in profiles, the match is by chance and not by capturing the underlying physics accurately, as is indicated by the total absence of a WCM. This last simulation with $\alpha = \infty$ is understood therefore as an academic test case.

Simulating a stationary I-mode is left for future work. To work in this direction a few points should be tested. Firstly and most importantly the magnetic equilibrium used for the simulation was constructed without a pressure constraint. A corrected version was already obtained and the first tests with this new equilibrium were made, which showed significant differences. However, performing a new set of simulations was beyond the scope of this thesis. A further point that might be relevant is the boundary condition applied to the neutral gas at the divertor, which might be too low, as suggested by the recycling rate. Simulations with higher values of neutral gas at the divertor or with a recently implemented recycling model, which eliminates this boundary condition as a free parameter, might be performed to investigate this point. A final point is, that no resolution scans were performed. This task is also left for future work. Nevertheless, the insights gained by this first I-mode simulation with the Landau fluid closure, especially the observation of PREs and the clear evidence of underlying MTMs, give some confidence that plasma fluid simulations of the I-mode regime are possible with the drift-reduced fluid model employed by GRILLIX including the Landau fluid closure.

7 Conclusion and Outlook

Within this thesis the drift-reduced fluid model employed by the edge turbulence code GRILLIX has been extended for low collisionality with a Landau-fluid closure, replacing the previously used limited Braginskii closure.

In Chapter 2 the necessity of fluid closures to close the fluid hierarchy was explained, as well as a derivation for the Braginskii closure [43] for the special case of a plasma under the Lorentz approximation. Furthermore, we explained why the Braginskii closure for the parallel heat fluxes breaks first for low collisionality. The Landau-fluid closure was motivated and derived in detail, following the original work [45, 44], including the motivation of matching the linear kinetic response function with a fluid model. The transformation into configuration space via an approximation with Lorentz functions [72] was shown. Lastly, we demonstrated that the drift reduction procedure leaves the Landau-fluid closure unaffected.

Chapter 3 is dedicated to a one-dimensional setup to show the effects of the Landau-fluid closure in a simple environment. The Landau-fluid closure was compared to the original Braginskii closure for various values of collisionality. The magnitudes of the heat fluxes match the theoretical expectations. A non-local behaviour of the Landau-fluid heat flux was observed in line with previous research [46]. The limits in terms of collisionality are examined in this setup and the behaviour when crossing them, where the predicted heat-flux is too low in amplitude.

The implementation of the Landau-fluid closure within the FCI framework is shown in Chapter 4. The major difference, that arose, is the problem becoming three-dimensional in comparison to a one-dimensional one in flux-aligned coordinate systems. A straightforward combination with the effect of magnetic flutter compensates for the disadvantage of the problem being fully three-dimensional. The implementation into GRILLIX was verified via MMS and by setting up a comparison case between the one-dimensional model and the implementation, where we achieved an agreement up to machine precision or the residuum of the iterative solver respectively.

In Chapter 5 turbulence simulations of an AUG L-mode discharge were performed and compared between the Braginskii closure with different heat-flux limiters and the Landau-fluid closure. Large parts of the content of this chapter have already been published [100]. It was shown that an incorrect treatment of parallel heat fluxes, i.e. too strong limitation in the Braginskii closure leads to a nonphysical temperature asymmetry. The Landau-fluid closure including the single Lorentz functions was investigated during the simulation, where the behaviour matches the expectations. The non-local behaviour was examined and we can conclude, that for every single point in the simulation domain, the correlation between parallel temperature gradient and heat flux is low, especially for electrons. The correlation is significantly higher after taking a flux-surface average and a comparison to flux limiters is possible. Overall only little global differences between the Landau-fluid closure and the Braginkii closure with $\alpha = 1.0$ were found, except for the radial electric field, where the Landau-fluid closure provided a radial electric field which was in better agreement with the experiment. Also for H-mode studies, that were conducted with GRILLIX, the best match of the radial electric field was best employing the Landau fluid closure [51]. However, the radial electric field plays a crucial role in improved confinement regimes and transitions like the L-H or I-H transition. Therefore capturing the radial

electric field accurately is a major improvement of the plasma fluid model.

An attempt to simulate the I-mode regime was undertaken in Chapter 6. The I-mode is an ELM-free, reactor-relevant operational regime with increased energy confinement time compared to L-mode [24]. Moreover, the I-mode shows high temperatures and low densities at the edge, i.e. low collisionality. In the quasi-stationary phases of the I-mode simulations, the profiles were not far off the experimental ones and traces of a WCM were visible. However, since in comparison to the simulation, no PREs were present in the experiment, a perfect match of the profiles was not expected. In between the quasi-stationary phases, intermittent events happen that can be linked to PREs, which are present in some I-mode discharges. The instability responsible for the sudden increase in radial energy transport is investigated in detail and identified with confidence to be a micro-tearing mode. Major experimentally measured properties of PREs are reproduced by the simulation. In contrast to the Landau-fluid closure, the Braginskii closure reproduces L-mode-like profiles and does not show any intermittent events within the simulation. Lastly, an academic test was performed, where the heat flux limiters were removed and the original Braginskii closure was employed. Although the profiles agree here with the experimental ones, the underlying physics do not. This demonstrates how sensitive the system reacts to changes in the parallel heat fluxes and how different the result can be for different flux limiters. Therefore, this test underlines the importance of modelling parallel heat fluxes accurately to make predictive and quantitative simulations possible. The results of this chapter emphasise that the Landau-fluid closure is a valuable extension for simulations in low collisional regimes.

Besides the progress that was made, a few points were raised within this work, that were left for future work. The first point is the solver for the elliptic Landau-fluid equation. Exchanging the currently used GMRES solver with more efficient methods might have the potential to save computation time and increase the stability of simulations. The second important point arises from the last chapter about the I-mode. The bursts which relate to PREs are a most interesting subject to study, especially due to the micro-tearing modes present. Nevertheless, a simulation of a stationary I-mode remains for future work. Ideas to approach this were listed in the corresponding section. Furthermore, it would be interesting to attempt simulations of an L-I transition, which means starting in L-mode conditions and increasing the heating power until a transition starts to happen. These simulations will probably need a long time as the heating power has to be adjusted stepwise after the simulation saturates. For this thesis, such simulations were beyond the scope.

There are also further reactor-relevant regimes, like the QCE regime or the XPR, which can be performed now with even more confidence, after simulating the I-mode regime, as the collisionality is significantly higher in those regimes and the fluid approximation deeper in its region of validity. Moving from tokamak to stellarator simulations is another big task for GRILLIX. The geometric capabilities are present, but to perform such simulations a lot of work and effort is needed. However, this is a task of major importance, since there are even fewer codes, which are able to perform edge turbulence simulations for stellarators than for tokamaks.

Looking from a more theoretical perspective, performing a comparison between the Landau-fluid closure, which includes linear Landau-damping into the fluid model, and a

gyro-kinetic code as e.g. GENE-X [101] or the arbitrary-moment approach [42] would provide further insights but is also left for future work.

To conclude, this thesis provides a step towards plasma edge turbulence simulations of reactor-relevant scenarios and devices. The observation of modelling the radial electric field more accurately with the Landau fluid closure is one of the main findings and will be of major importance for future simulations of transitions, e.g. the L-H transition, or improved confinement regimes, in which the radial electric field plays a crucial role. With the attempt to simulate the I-mode regime, we approached a reactor-relevant operational regime, which is the second big result of this thesis. Although there is still much work to do, with this step we started paving the path to simulate such scenarios regularly and make predictions for machines like ITER. Following this path further will hopefully gain deep insights for future fusion research and the first terrestrial stars may seem a little less distant.

Appendix

A Model equations

The physical model used for the turbulence simulations consists of eight equations, the continuity equation (147), vorticity equation (148), parallel-momentum equation (149), Ohms law (150), electron temperature equation (151), ion temperature equation (152), Amperes law (153) and the equation for the neutrals density (154). In the following equations $\phi = (T_{e0}/e)\hat{\phi}$ is the electrostatic potential, $p_e = nT_e$ and $p_i = nT_i$ the electron and ion pressure, $j_\parallel = n(u_\parallel - v_\parallel) = c_{s0} e n_0 \hat{j}_\parallel$ the parallel current, $u_\parallel = c_{s0}\hat{u}_\parallel$ the parallel ion velocity, $v_\parallel = c_{s0}\hat{v}_\parallel$ the parallel electron velocity, the remaining physical quantities were mentioned in the main text. The curvature operator is defined as

$$\hat{C}(f) = \delta_0 \left[-\left(\hat{\nabla} \times \left(\mathbf{b}/\hat{B} \right) \right) \cdot \hat{\nabla} f \right] \tag{145}$$

for a test function f. The ion viscous stress function is $G = n_0 T_{i0} \hat{G}$ with

$$\hat{G} = -\tilde{\eta}_{i0} \hat{T}_i^{5/2} \left[2\hat{B}^{-3/2} \hat{\nabla} \cdot \left(\hat{u}_\parallel \hat{B}^{3/2} \mathbf{b} \right) - \hat{C}(\hat{\phi})/2 - \hat{C}(\hat{p}_i)/(2\hat{n}) \right]. \tag{146}$$

The terms $D_\alpha(\alpha)$ are numerical diffusion terms acting on a quantity α, and S_α are source terms for density and temperature, including the heating at the core boundary as well as the interaction with neutral gas. The ion viscous heating term, which is the eighth term on the right-hand side of eq. (152) was turned off for the presented simulations. In eq. (154) N is the neutrals density and $D_N = T_i/(M_i k_{\mathrm{cx}} n)$, with k_{iz} the ionisation rate coefficient, k_{rec} the recombination rate coefficient, k_{cx} the charge-exchange rate coefficient, for further details on the neutrals model we refer to Zholobenko et al. [40]. The dimensionless parameters used in the equations are $\delta_0 = \frac{R_0}{\rho_{s0}}$, $\zeta = T_{i0}/T_{e0}$, $\beta_0 = 4\pi n_0 T_{e0}/B_0^2$, $\mu = m_e/M_i$ with m_e the electron and M_i the ion mass, $\eta_{\parallel 0} = 0.51\mu\nu_{e0}$, $\nu_{e0} = R_0/(c_{s0}\tau_{e0})$, $\eta_{i0} = 0.96 c_{s0}\tau_{i0}/R_0$, $\kappa_{\parallel e0} = 3.16 c_{s0}\tau_{e0}/(R_0\mu)$ and $\kappa_{\parallel i0} = 3.9 c_{s0}\tau_{i0}\zeta/R_0$. The advective derivative is defines as $\frac{\mathrm{d}}{\mathrm{d}t} = \frac{\partial}{\partial t} + \delta_0 \left(\mathbf{b}/\hat{B} \times \nabla\hat{\phi} \right)$. All quantities in the following equations are normalised, therefore we omit the hat for indication of normalised quantities.

$$\frac{\mathrm{d}}{\mathrm{d}t} n = nC(\phi) - C(p_e) + \nabla \cdot \left[\left(j_\parallel - n u_\parallel \right) \mathbf{b} \right] + D_n(n) + S_n \tag{147}$$

$$\begin{aligned} \nabla \cdot \left[\frac{n}{B^2} \left(\frac{\mathrm{d}}{\mathrm{d}t} + u_\parallel \nabla_\parallel \right) \left(\nabla_\perp \phi + \zeta \frac{\nabla_\perp p_i}{n} \right) \right] = & -C(p_e + \zeta p_i) + \nabla \cdot \left(j_\parallel \mathbf{b} \right) \\ & - \frac{\zeta}{6}(G) + D_\Omega(\Omega) \end{aligned} \tag{148}$$

$$\left(\frac{\mathrm{d}}{\mathrm{d}t} + u_\parallel \nabla_\parallel \right) u_\parallel = -\frac{\nabla_\parallel (p_e + \zeta p_i)}{n} + \zeta T_i C(u_\parallel) - \frac{2}{3}\zeta \frac{B^{3/2}}{n} \nabla_\parallel \frac{G}{B^{3/2}} + D_{u_\parallel}(u_\parallel) \tag{149}$$

$$\beta_0 \frac{\partial}{\partial t} A_\parallel + \mu \left(\frac{\mathrm{d}}{\mathrm{d}t} + \nu_\parallel \nabla_\parallel \right) \frac{j_\parallel}{n} = - \left(\frac{\eta_{\parallel 0}}{T_e^{3/2}} \right) j_\parallel - \nabla_\parallel \phi + \frac{\nabla_\parallel p_e}{n} + 0.71 \nabla_\parallel T_e + D_{\Psi_m} \left(\Psi_m \right) \tag{150}$$

$$\begin{aligned} \frac{3}{2} \left(\frac{\mathrm{d}}{\mathrm{d}t} + v_\parallel \nabla_\parallel \right) T_e =& T_e C(\phi) - \frac{T_e}{n} C(p_e) - \frac{5}{2} T_e C(T_e) - T_e \nabla \cdot \left(v_\parallel \mathbf{b} \right) \\ &+ 0.71 \frac{T_e}{n} \nabla \cdot \left(\mathbf{b} j_\parallel \right) - 3 \nu_{e0} \mu \left(\frac{n}{T_e^{3/2}} \right) \left(T_e - \zeta T_i \right) \\ &- \frac{1}{n} \nabla \cdot \left(q_{\parallel e} \mathbf{b} \right) + \left(\frac{\eta_{\parallel 0}}{T_e^{3/2}} \right) \frac{j_\parallel^2}{n} + \frac{3}{2} \left(D_{T_e} \left(T_e \right) + S_{T_e} \right) \end{aligned} \tag{151}$$

$$\begin{aligned} \frac{3}{2} \left(\frac{\mathrm{d}}{\mathrm{d}t} + u_\parallel \nabla_\parallel \right) T_i =& T_i C(\phi) - \frac{T_i}{n} C(p_e) + \frac{5}{2} \zeta T_i C(T_i) - T_i \nabla \cdot \left(u_\parallel \mathbf{b} \right) + \frac{T_i}{n} \nabla \cdot \left(j_\parallel \mathbf{b} \right) \\ &- \frac{1}{n} \nabla \cdot \left(q_{\parallel i} \mathbf{b} \right) + 3 \nu_{e0} \mu \left(\frac{n}{T_e^{3/2}} \right) \left(\frac{1}{\zeta} T_e - T_i \right) \\ &+ \frac{1}{3 \eta_{i0}} \frac{1}{n T_i^{5/2}} G^2 + \frac{3}{2} \left(D_{T_i} \left(T_i \right) + S_{T_i} \right) \end{aligned} \tag{152}$$

$$\nabla_\perp^2 A_\parallel = -j_\parallel \tag{153}$$

$$\frac{\partial}{\partial t} N = \nabla \cdot \frac{D_N}{T_i} \nabla N T_i - k_{\mathrm{iz}} n N + k_{\mathrm{rec}} n^2 \tag{154}$$

The neoclassical extension of the ion viscosity G essentially adapts the Braginskii coefficient η_{i0} to $\tilde{\eta}_{i0}$ according to eq. (39) in Rozhansky *et al.*[102]. This follows the work of Hirshman and Sigmar from 1981[103], figure 1 therein shows in particular that this introduces an upper limit for the ion viscosity coefficient, while the Braginskii expression diverges as $T_i^{5/2}$, similarly to the (ion) heat conductivity. Neoclassical heat viscosity is not yet included. For the work here, we approximate the connection length as $L_c \approx q_{95} R_0$, and the inverse aspect ratio as $\epsilon \approx 0.3$, these are typical values for ASDEX Upgrade. Details on the physical effect of this extension will be published separately. We have to make the remark that all simulations presented in Chapter 5 contain a small mistake in the form of the neoclassical extension. The collisionality was implemented with a temperature dependency of $\nu_i \propto T_i^{5/2}$ instead of the correct dependency of T_i^2. Although small quantitative changes are possible, we do not expect a qualitative change in the results, especially as the same model (including the mistake) was used for all simulations. For the simulations presented in Chapter 6 this mistake was already corrected.

B Transformation of the Hammett-Perkins closure

To transform the Hammett-Perkins closure into configuration space we use a similar method as the one used for the Landau-fluid closure. The method is also a fast non-Fourier method [72]. The approximation of the exact function for the Hammett-Perkins heat flux also relies on Lorentz functions

$$q_{\parallel,k}^{\mathrm{HP}} = -A\frac{ik_\parallel}{|k_\parallel|}T_{\alpha,k} \approx -A\sum_{n=0}^{N-1}\frac{k_0\alpha^n\beta}{k_\parallel^2+(k_0\alpha^n)^2}ik_\parallel T_{\alpha,k}, \tag{155}$$

where in contrast to the Landau-fluid closure just three numerical constants are necessary. The value of $a = 5.0$, $b = 1.0275$ and $k_0 = 1.0$ are motivated by [46]. To illustrate how to represent different ranges of parallel wave numbers $k_\parallel$, we reproduce two figures from [46].

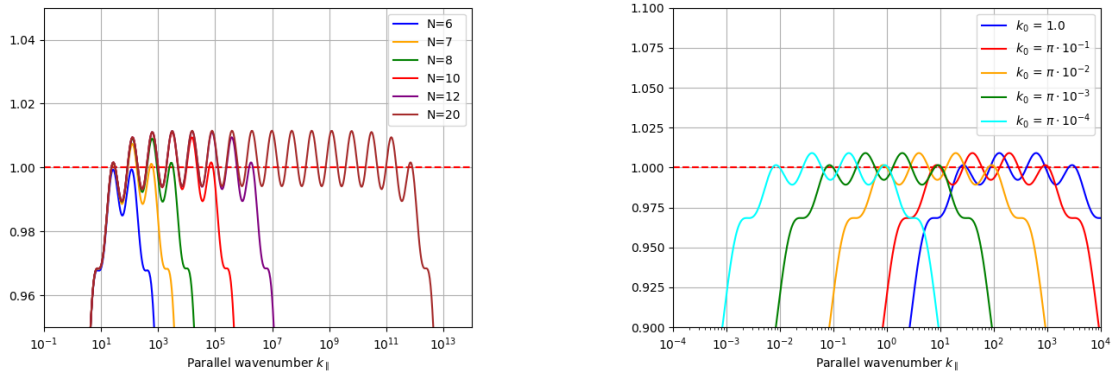

(a) Sums of Lorentz functions with different N (b) Sums of Lorentz functions with different k_0

Figure 64: Sums of Lorentz functions for the Hammett-Perkins closure with different values of N and k_0

In fig. 64 we observe that by increasing the number of Lorentz functions N, we can expand the range towards larger parallel wave numbers $k_\parallel$ and by decreasing the value of k_0, we can increase the range towards smaller $k_\parallel$. Similar to the Landau-fluid closure, each Lorentz function can be transformed into configuration space

$$\left[-\nabla_\parallel^2+(k_0\alpha^n)^2\right]q_{\parallel\alpha,n}^{\mathrm{HP}} = -Ak_0\alpha^n\beta\nabla_\parallel T_\alpha. \tag{156}$$

C Fit for Lorentz functions

The parameters α_n and β_n in table 1 for the Lorentz functions of the Landau-fluid model are taken from [46]. To verify these numerical parameters a fit was performed using the python module LMFIT [104], which was also employed in [46]. The resulting parameters are shown in table 5.

n	α_n	β_n
1	0.0046960	0.13975
2	0.51308	1.0047
3	5.3780	5.1124
4	34.7388	30.1791
5	216.7386	186.4066
6	1370.083	1165.395
7	14058.137	8687.863

Table 5: Values for the parameters α_n and β_n for the case of $N = 7$ Lorentz functions obtained with the python module LMFIT [104]

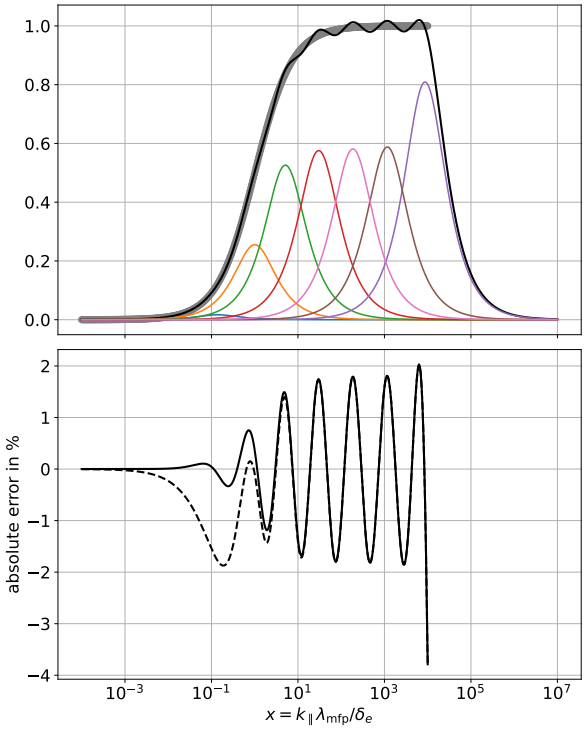

Figure 65: The 7 Lorentz functions corresponding to table 5 in colours, in black their sum and in grey the exact function. Below the error between the black and grey curve and the dashed line shows the error neglecting the first Lorentz function $n = 1$

The values for the numerical parameters are close to the ones provided in [46]. The region of interest in x, where the Lorentz functions are fitted to the analytical curve can still be fine-tuned to increase the agreement of the parameters. However, an exact reproduction is not the purpose of this section, but the fact that these fits can be performed quite easily. The Lorentz functions and their sum are shown in fig. 65. Furthermore, in the lower plot, we visualise the error between the analytical function in grey and the sum of Lorentz functions in black. The solid black line is the error for the complete sum, while the dashed line shows the error without the first Lorentz function $n = 1$.

The purpose of plotting the dashed curve is, that in some cases we could observe that the low-numbered Lorentz functions converge very slowly. A possible way to make this problem less severe would be to exclude here the lowest numbered Lorentz function. As we observe in the lower plot of fig. 65, the error for low values of x decreases, but stays still below 2%.

Acknowledgements

First of all, I would like to thank my supervisor Frank Jenko, without whom this work would not have been possible, as he was the one hiring me as a PhD. I learned something in every conversation we had, either about physics or how to run an institute. Especially I want to thank him for the first few months when COVID-19 forced the whole institute to work from home, he spent a lot of time to keep contact with me and introduced me to the field of plasma physics, which was completely new to me.

I want to say a huge thank you to my mentor Andreas Stegmeir. No matter how busy he was, he had always time for me, when I bothered him with smart and not-so-smart questions. Despite our different tastes in music, films, books, etc. it was always a lot of fun spending time with him. Especially in stressful periods, like writing our first paper, he was always motivating me and pushing me with the right amount of force (in his opinion). Most importantly, I want to thank him for being always very honest with me, often it felt more like two scientists working together instead of a PhD and his mentor. I truly couldn't think of a better mentor for my dissertation. If there is some kind of supervision award he should get one.

Many thanks to the whole GRILLIX team. Especially Wladimir and Tom, who welcomed me to the team in the beginning. And a special thank you to Wladimir for explaining to me a lot of physics questions and for many fascinating discussions, although often I didn't get everything. Furthermore tanks to the coolest PhD office, with Kaiyu, Konrad and Jan. It was always fun discussing physics, being puzzled by bugs or playing a game of Otrio in the office.

I want to thank also the whole GENE-X team, Philipp, Marion, Jordy and Sabine. The common GRILLIX/GENE-X workshops were always a highlight. And of course, also Carl and Baptiste, who joined the team later, but increased the fun factor significantly.

I'm grateful towards the whole TOK department, especially Tobias and Emmanuele, who helped me often with more or less intricate organisational questions, but also with physics questions from time to time.

Additionally, I want to thank Per Helander, whose lectures I followed with the most interest and with whom I enjoyed playing the piano four-handed at Schloss Ringberg. Thanks to Ben Zhu for discussions about the Landau fluid closure, with which he worked even before I started my PhD. I want to thank Tim Happel, Peter Manz and Manuel Herschel for discussions regarding everything around the I-mode regime. I enjoyed working with you on such an important topic very much.

Lastly, many thanks to Ingrid Kaufmann for recruiting me as a visitor guide. I always enjoyed giving tours at the IPP and ASDEX Upgrade. And I learned a lot by preparing for the tours and also from time to time I learned really interesting things from some of the visitors.

References

[1] E. Pernicka, J. Adam, G. Borg, G. Brügmann, J.-H. Bunnefeld, W. Kainz, M. Klamm, T. Koiki, H. Meller, R. Schwarz, *et al.*, "Why the Nebra Sky Disc Dates to the Early Bronze Age. An Overview of the Interdisciplinary Results," *Archaeologia Austriaca*, vol. 104, pp. 89–122, 2020.

[2] G. Kopp and J. L. Lean, "A new, lower value of total solar irradiance: Evidence and climate significance," *Geophysical Research Letters*, vol. 38, no. 1, 2011.

[3] NASA, "Current solar images." https://umbra.nascom.nasa.gov/images/latest.html, 2024. Accessed: 7th of June 2024.

[4] H. A. Bethe, "Energy production in stars," *Physical Review*, vol. 55, no. 5, p. 434, 1939.

[5] W. F. Bleam, *Soil and environmental chemistry*. Academic Press, 2016.

[6] J. Wesson and D. J. Campbell, *Tokamaks*, vol. 149. Oxford university press, 2011.

[7] J. A. Bittencourt, *Fundamentals of plasma physics*. Springer Science & Business Media, 2013.

[8] F. F. Chen *et al.*, *Introduction to plasma physics and controlled fusion*, vol. 1. Springer, 1984.

[9] B. Scott, "Low Frequency Fluid Drift Turbulence in Magnetised Plasmas," *Habilitation at Heinrich-Heine-Universität*, 2000.

[10] J. D. Lawson, "Some criteria for a power producing thermonuclear reactor," *Proceedings of the physical society. Section B*, vol. 70, no. 1, p. 6, 1957.

[11] T. Casper, Y. Gribov, A. Kavin, V. Lukash, R. Khayrutdinov, H. Fujieda, C. Kessel, I. D. Agencies, *et al.*, "Development of the ITER baseline inductive scenario," *Nuclear Fusion*, vol. 54, no. 1, p. 013005, 2013.

[12] "Commonwealth Fusion Systems." https://cfs.energy, 2024. Accessed: 4th of May 2024.

[13] "TAE Technologies." https://tae.com, 2024. Accessed: 4th of May 2024.

[14] "Type One Energy." https://typeoneenergy.com, 2024. Accessed: 4th of May 2024.

[15] F. Troyon, A. Roy, W. Cooper, F. Yasseen, and A. Turnbull, "Beta limit in tokamaks. Experimental and computational status," *Plasma Physics and Controlled Fusion*, vol. 30, no. 11, p. 1597, 1988.

[16] M. Greenwald, "Density limits in toroidal plasmas," *Plasma Physics and Controlled Fusion*, vol. 44, no. 8, p. R27, 2002.

[17] N. Mitchell, A. Devred, P. Libeyre, B. Lim, and F. Savary, "The ITER magnets: Design and construction status," *IEEE transactions on applied superconductivity*, vol. 22, no. 3, pp. 4200809–4200809, 2011.

[18] Z. S. Hartwig, R. F. Vieira, D. Dunn, T. Golfinopoulos, B. LaBombard, C. J. Lammi, P. C. Michael, S. Agabian, D. Arsenault, R. Barnett, *et al.*, "The SPARC toroidal field model coil program," *IEEE Transactions on Applied Superconductivity*, 2023.

[19] P. Rodriguez-Fernandez, A. Creely, M. Greenwald, D. Brunner, S. Ballinger, C. Chrobak, D. Garnier, R. Granetz, Z. Hartwig, N. Howard, *et al.*, "Overview of the sparc physics basis towards the exploration of burning-plasma regimes in high-field, compact tokamaks," *Nuclear Fusion*, vol. 62, no. 4, p. 042003, 2022.

[20] A. Stegmeir, D. Coster, A. Ross, O. Maj, K. Lackner, and E. Poli, "GRILLIX: a 3D turbulence code based on the flux-coordinate independent approach," *Plasma Physics and Controlled Fusion*, vol. 60, no. 3, p. 035005, 2018.

[21] C. S. Pitcher and P. Stangeby, "Experimental divertor physics," *Plasma Physics and Controlled Fusion*, vol. 39, no. 6, p. 779, 1997.

[22] R. A. Pitts, X. Bonnin, F. Escourbiac, H. Frerichs, J. Gunn, T. Hirai, A. Kukushkin, E. Kaveeva, M. Miller, D. Moulton, *et al.*, "Physics basis for the first ITER tungsten divertor," *Nuclear Materials and Energy*, vol. 20, p. 100696, 2019.

[23] ASDEX Team, "The H-Mode of ASDEX," *Nucl. Fusion*, vol. 29, no. 11, p. 1959, 1989.

[24] D. Whyte, A. Hubbard, J. Hughes, B. Lipschultz, J. Rice, E. Marmar, M. Greenwald, I. Cziegler, A. Dominguez, T. Golfinopoulos, *et al.*, "I-mode: an H-mode energy confinement regime with L-mode particle transport in Alcator C-Mod," *Nuclear Fusion*, vol. 50, no. 10, p. 105005, 2010.

[25] Faitsch, Michael and Eich, T and Harrer, GF and Wolfrum, Elisabeth and Brida, D and David, P and Griener, M and Stroth, U and ASDEX Upgrade Team and EUROfusion MST1 Team and others, "Broadening of the power fall-off length in a high density, high confinement H-mode regime in ASDEX Upgrade," *Nuclear Materials and Energy*, vol. 26, p. 100890, 2021.

[26] M. Bernert, F. Janky, B. Sieglin, A. Kallenbach, B. Lipschultz, F. Reimold, M. Wischmeier, M. Cavedon, P. David, M. Dunne, *et al.*, "X-point radiation, its control and an ELM suppressed radiating regime at the ASDEX Upgrade tokamak," *Nuclear Fusion*, vol. 61, no. 2, p. 024001, 2020.

[27] F. Wagner, "A quarter-century of H-mode studies," *Plasma Physics and Controlled Fusion*, vol. 49, no. 12B, p. B1, 2007.

[28] P. Manz, "The microscopic picture of plasma edge turbulence," *Habilitation at Technische Universität München*, 2018.

[29] H. Zohm, "The physics of edge localized modes (ELMs) and their role in power and particle exhaust," *Plasma Physics and Controlled Fusion*, vol. 38, no. 8, p. 1213, 1996.

[30] T. Eich and A.W. Leonard and R.A. Pitts and W. Fundamenski and R.J. Goldston and T.K. Gray and A. Herrmann and A. Kirk and A. Kallenbach and O. Kardaun and A.S. Kukushkin and B. LaBombard and R. Maingi and M.A. Makowski and A. Scarabosio and B. Sieglin and J. Terry and A. Thornton and ASDEX Upgrade Team and JET EFDA Contributors, "Scaling of the tokamak near the scrape-off layer H-mode power width and implications for ITER," *Nuclear Fusion*, vol. 53, p. 093031, aug 2013.

[31] C. S. Chang, S. Ku, A. Loarte, V. Parail, F. Koechl, M. Romanelli, R. Maingi, J.-W. Ahn, T. Gray, J. Hughes, *et al.*, "Gyrokinetic projection of the divertor heat-flux width from present tokamaks to ITER," *Nuclear Fusion*, vol. 57, no. 11, p. 116023, 2017.

[32] B. Dudson, M. Umansky, X. Xu, P. Snyder, and H. Wilson, "BOUT++: A framework for parallel plasma fluid simulations," *Comput. Phys. Commun.*, vol. 180, no. 9, pp. 1467–1480, 2009.

[33] B. Zhu, M. Francisquez, and B. N. Rogers, "GDB: A global 3D two-fluid model of plasma turbulence and transport in the tokamak edge," *Comput. Phys. Commun.*, vol. 232, pp. 46–58, 2018.

[34] M. Giacomin, P. Ricci, A. Coroado, G. Fourestey, D. Galassi, E. Lanti, D. Mancini, N. Richart, L. Stenger, and N. Varini, "The GBS code for the self-consistent simulation of plasma turbulence and kinetic neutral dynamics in the tokamak boundary," *J. Comput. Phys.*, vol. 463, p. 111294, 2022.

[35] H. Bufferand, J. Bucalossi, G. Ciraolo, G. Falchetto, A. Gallo, P. Ghendrih, N. Rivals, P. Tamain, H. Yang, G. Giorgiani, F. Schwander, M. S. d'Abusco, E. Serre, Y. Marandet, M. Raghunathan, WEST Team, and the JET Team, "Progress in edge plasma turbulence modelling—hierarchy of models from 2D transport application to 3D fluid simulations in realistic tokamak geometry," *Nucl. Fusion*, vol. 61, p. 116052, 2021.

[36] M. Wiesenberger and M. Held, "Effects of plasma resistivity in feltor simulations of three-dimensional full-f gyro-fluid turbulence," *Plasma Physics and Controlled Fusion*, vol. 66, no. 6, p. 065003, 2024.

[37] A. Stegmeir, A. Ross, T. Body, M. Francisquez, W. Zholobenko, D. Coster, O. Maj, P. Manz, F. Jenko, B. N. Rogers, and K. S. Kang, "Global turbulence simulations of the tokamak edge region with GRILLIX," *Phys. Plasmas*, vol. 26, p. 052517, 2019.

[38] F. Jenko, W. Dorland, M. Kotschenreuther, and B. Rogers, "Electron temperature gradient driven turbulence," *Physics of plasmas*, vol. 7, no. 5, pp. 1904–1910, 2000.

[39] Michels, Dominik and Ulbl, Philipp and Zholobenko, Wladimir and Body, Thomas and Stegmeir, Andreas and Eich, Thomas and Griener, Michael and Conway, Garrard D and Jenko, Frank and ASDEX Upgrade Team and others, "Full-f electromagnetic gyrokinetic turbulence simulations of the edge and scrape-off layer of ASDEX Upgrade with GENE-X," *Physics of Plasmas*, vol. 29, no. 3, 2022.

[40] W. Zholobenko and A. Stegmeir and M. Griener and G.D. Conway and T. Body and D. Coster and F. Jenko and the ASDEX Upgrade Team, "The role of neutral gas in validated global edge turbulence simulations," *Nucl. Fusion*, vol. 61, p. 116015, 2021.

[41] B. Zhu, M. Francisquez, and B. N. Rogers, "Global 3D two-fluid simulations of the tokamak edge region: Turbulence, transport, profile evolution, and spontaneous E× B rotation," *Phys. Plasmas*, vol. 24, no. 5, p. 055903, 2017.

[42] B. J. Frei, R. Jorge, and P. Ricci, "A gyrokinetic model for the plasma periphery of tokamak devices," *Journal of Plasma Physics*, vol. 86, no. 2, p. 905860205, 2020.

[43] S. I. Braginskii and M. A. Leontovich, "Transport processes in plasmas," *Rev. plasma phys.*, vol. 205, 1965.

[44] M. Umansky, A. Dimits, I. Joseph, J. Omotani, and T. Rognlien, "Modeling of tokamak divertor plasma for weakly collisional parallel electron transport," *J. Nucl. Mater.*, vol. 463, pp. 506–509, 2015.

[45] G. W. Hammett and F. W. Perkins, "Fluid moment models for Landau damping with application to the ion-temperature-gradient instability," *Phys. Rev. Lett.*, vol. 64, p. 3019, 1990.

[46] X. X. J.G. Chen and Y. Lei, "Extension of Landau-fluid closure to weakly collisional plasma regime," *Comput. Phys. Commun.*, vol. 236, pp. 128–134, 2019.

[47] M. Ottaviani, "An alternative approach to field-aligned coordinates for plasma turbulence simulations," *Phys. lett., A*, vol. 375, no. 15, pp. 1677–1685, 2011.

[48] A. Stegmeir, D. Coster, O. Maj, K. Hallatschek, and K. Lackner, "The field line map approach for simulations of magnetically confined plasmas," *Comput. Phys. Commun.*, vol. 198, pp. 139–153, 2016.

[49] B. Zhu, H. Seto, X.-q. Xu, and M. Yagi, "Drift reduced Landau fluid model for magnetized plasma turbulence simulations in BOUT++ framework," *Comput. Phys. Commun.*, vol. 267, p. 108079, 2021.

[50] K. Zhang, W. Zholobenko, A. Stegmeir, K. Eder, and F. Jenko, "Magnetic flutter effect on validated edge turbulence simulations," *Nuclear Fusion*, vol. 64, no. 3, p. 036016, 2024.

[51] Zholobenko, Wladimir and Zhang, Kaiyu and Stegmeir, Andreas and Pfennig, Jan and Eder, Konrad and Pitzal, Christoph and Ulbl, Philipp and Griener, Michael and Radovanovic, Lidija and Plank, Ulrike and the ASDEX Upgrade Team, "Tokamak

H-mode edge-SOL global turbulence simulations with an electromagnetic, transcollisional drift-fluid model," *Submitter to Nuclear Fusion*, 2024.

[52] T Happel and P Manz and F Ryter and M Bernert and M Dunne and P Hennequin and A Hetzenecker and U Stroth and G D Conway and L Guimarais and C Honoré and E Viezzer and the ASDEX Upgrade Team, "The I-mode confinement regime at ASDEX Upgrade: global properties and characterization of strongly intermittent density fluctuations," *Plasma Phys. Control. Fusion*, vol. 59, no. 1, p. 014004, 2016.

[53] D. Silvagni, T. Eich, T. Happel, G. Harrer, M. Griener, M. Dunne, M. Cavedon, M. Faitsch, L. Gil, D. Nille, *et al.*, "I-mode pedestal relaxation events at ASDEX Upgrade," *Nuclear Fusion*, vol. 60, no. 12, p. 126028, 2020.

[54] P. L. Bhatnagar, E. P. Gross, and M. Krook, "A model for collision processes in gases. I. Small amplitude processes in charged and neutral one-component systems," *Physical review*, vol. 94, no. 3, p. 511, 1954.

[55] P. Helander and D. Sigmar, *Collisional Transport in Magnetized Plasmas*. Cambridge Monographs on Plasma Physics, Cambridge University Press, 2005.

[56] M. Raeth, K. Hallatschek, and K. Kormann, "Simulation of ion temperature gradient driven modes with 6D kinetic Vlasov code," *arXiv preprint arXiv:2402.06605*, 2024.

[57] A. J. Brizard and T. S. Hahm, "Foundations of nonlinear gyrokinetic theory," *Reviews of modern physics*, vol. 79, no. 2, p. 421, 2007.

[58] T. Goerler, X. Lapillonne, S. Brunner, T. Dannert, F. Jenko, F. Merz, and D. Told, "The global version of the gyrokinetic turbulence code GENE," *Journal of Computational Physics*, vol. 230, no. 18, pp. 7053–7071, 2011.

[59] S. Ku, C.-S. Chang, and P. H. Diamond, "Full-f gyrokinetic particle simulation of centrally heated global ITG turbulence from magnetic axis to edge pedestal top in a realistic tokamak geometry," *Nuclear Fusion*, vol. 49, no. 11, p. 115021, 2009.

[60] S. Chapman and T. Cowling, *The Mathematical Theory of Non-uniform Gases: Notes Added in 1951*. Cambridge University Press, 1953.

[61] A. Richardson, *2019 NRL plasma formulary*. Naval Research Laboratory Washington, DC, 2019.

[62] H. Zohm, *Magnetohydrodynamic stability of tokamaks*. John Wiley & Sons, 2015.

[63] P. C. Stangeby *et al.*, *The plasma boundary of magnetic fusion devices*, vol. 224. Institute of Physics Pub. Philadelphia, Pennsylvania, 2000.

[64] W. Fundamenski, "Parallel heat flux limits in the tokamak scrape-off layer," *Plasma Phys. Control. Fusion*, vol. 47, no. 11, p. R163, 2005.

[65] T. Y. Xia and X. Q. Xu, "Nonlinear fluid simulation of particle and heat fluxes during burst of ELMs on DIII-D with BOUT++code," *Nucl. Fusion*, vol. 55, no. 11, p. 113030, 2015.

[66] L. Landau, "On the Vibrations of the Electronic Plasma," in *Collected Papers of L.D. Landau*, pp. 445–460, Pergamon, 1965.

[67] A. J. Wootton, B. A. Carreras, H. Matsumoto, K. McGuire, W. A. Peebles, C. P. Ritz, P. W. Terry, and S. J. Zweben, "Fluctuations and anomalous transport in tokamaks," *Physics of Fluids B: Plasma Physics*, vol. 2, pp. 2879–2903, 12 1990.

[68] Freethy, S. J. and Görler, T. and Creely, A. J. and Conway, G. D. and Denk, S. S. and Happel, T. and Koenen, C. and Hennequin, P. and White, A. E. and ASDEX Upgrade Team, "Validation of gyrokinetic simulations with measurements of electron temperature fluctuations and density-temperature phase angles on ASDEX Upgrade," *Physics of Plasmas*, vol. 25, p. 055903, 03 2018.

[69] P. B. Snyder, G. W. Hammett, and W. Dorland, "Landau fluid models of collisionless magnetohydrodynamics," *Phys. Plasmas*, vol. 4, no. 11, pp. 3974–3985, 1997.

[70] M. A. Beer and G. W. Hammett, "Toroidal gyrofluid equations for simulations of tokamak turbulence," *Phys. Plasmas*, vol. 3, no. 11, pp. 4046–4064, 1996.

[71] L. Wang, X. Q. Xu, B. Zhu, C. Ma, and Y.-a. Lei, "Deep learning surrogate model for kinetic Landau-fluid closure with collision," *AIP Adv.*, vol. 10, no. 7, p. 075108, 2020.

[72] A. M. Dimits, I. Joseph, and M. V. Umansky, "A fast non-Fourier method for Landau-fluid operators," *Phys. Plasmas*, vol. 21, no. 5, p. 055907, 2014.

[73] A. Zeiler, "Tokamak Edge Turbulence," *Habilitation at Universität Ulm*, 1999.

[74] B. Scott, *Turbulence and Instabilities in Magnetised Plasmas, Volume 1: Fluid drift turbulence*. IOP Publishing, 2021.

[75] A. Meister, *Numerik linearer Gleichungssysteme*, vol. 4. Springer, 2011.

[76] S. D. Conte and C. De Boor, *Elementary numerical analysis: an algorithmic approach*. SIAM, 2017.

[77] F. Hariri and M. Ottaviani, "A flux-coordinate independent field-aligned approach to plasma turbulence simulations," *Comput. Phys. Commun.*, vol. 184, no. 11, pp. 2419–2429, 2013.

[78] M. Shashkov and S. Steinberg, "Support-operator finite-difference algorithms for general elliptic problems," *Journal of Computational Physics*, vol. 118, no. 1, pp. 131–151, 1995.

[79] R. D. da Cunha and T. Hopkins, "The Parallel Iterative Methods (PIM) package for the solution of systems of linear equations on parallel computers," *Appl. Numer. Math.*, vol. 19, no. 1, pp. 33–50, 1995. Special Issue on Massively Parallel Computing and Applications.

[80] A. Stegmeir, T. Body, and W. Zholobenko, "Analysis of locally-aligned and non-aligned discretisation schemes for reactor-scale tokamak edge turbulence simulations," *Comput. Phys. Commun.*, vol. 290, p. 108801, 2023.

[81] Y. Saad and M. H. Schultz, "GMRES: A generalized minimal residual algorithm for solving nonsymmetric linear systems," *SIAM Journal on scientific and statistical computing*, vol. 7, no. 3, pp. 856–869, 1986.

[82] M. R. Hestenes, E. Stiefel, *et al.*, *Methods of conjugate gradients for solving linear systems*, vol. 49. NBS Washington, DC, 1952.

[83] K. Salari and P. Knupp, "Code Verification by the Method of Manufactured Solutions," 2000.

[84] W Zholobenko and T Body and P Manz and A Stegmeir and B Zhu and M Griener and G D Conway and D Coster and F Jenko and the ASDEX Upgrade Team, "Electric field and turbulence in global Braginskii simulations across the ASDEX Upgrade edge and scrape-off layer," *Plasma Phys. Control. Fusion*, vol. 63, no. 3, p. 034001, 2021.

[85] J. T. Omotani and B. D. Dudson, "Non-local approach to kinetic effects on parallel transport in fluid models of the scrape-off layer," *Plasma Phys. Control. Fusion*, vol. 55, p. 055009, apr 2013.

[86] J. P. Brodrick, R. J. Kingham, M. M. Marinak, M. V. Patel, A. V. Chankin, J. T. Omotani, M. V. Umansky, D. Del Sorbo, B. Dudson, J. T. Parker, G. D. Kerbel, M. Sherlock, and C. P. Ridgers, "Testing nonlocal models of electron thermal conduction for magnetic and inertial confinement fusion applications," *Phys. Plasmas*, vol. 24, no. 9, 2017. 092309.

[87] R. D. Falgout and U. M. Yang, "hypre: A Library of High Performance Preconditioners," in *International Conference on computational science*, pp. 632–641, Springer, 2002.

[88] Manz, P and Happel, T and Stroth, U and Eich, T and Silvagni, D and ASDEX Upgrade Team and others, "Physical mechanism behind and access to the I-mode confinement regime in tokamaks," *Nuclear Fusion*, vol. 60, no. 9, p. 096011, 2020.

[89] F. Wagner, G. Fussmann, and e. a. Grave, "Development of an Edge Transport Barrier at the H-Mode Transition of ASDEX," *Phys. Rev. Lett.*, vol. 53, pp. 1453–1456, 1984.

[90] A. Marinoni, J. Rost, M. Porkolab, A. Hubbard, T. Osborne, A. White, D. Whyte, T. Rhodes, E. Davis, D. Ernst, *et al.*, "Characterization of density fluctuations during the search for an I-mode regime on the DIII-D tokamak," *Nuclear Fusion*, vol. 55, no. 9, p. 093019, 2015.

[91] M. Reinke, D. Brunner, T. Golfinopoulos, A. Hubbard, J. Hughes, A. Kuang, B. LaBombard, E. Marmar, R. Mumgaard, J. Terry, *et al.*, "Radiative heat exhaust in Alcator C-Mod I-mode plasmas," *Nuclear Fusion*, vol. 59, no. 4, p. 046018, 2019.

[92] D. Silvagni, J. L. Terry, W. McCarthy, A. E. Hubbard, T. Eich, M. Faitsch, L. Gil, T. Golfinopoulos, G. Grenfell, M. Griener, *et al.*, "I-mode pedestal relaxation events in the Alcator C-Mod and ASDEX Upgrade tokamaks," *Nuclear Fusion*, vol. 62, no. 3, p. 036004, 2022.

[93] P. Manz, P. Lauber, V. Nikolaeva, T. Happel, F. Ryter, G. Birkenmeier, A. Bogomolov, G. Conway, M. Manso, M. Maraschek, *et al.*, "Geodesic oscillations and the weakly coherent mode in the I-mode of ASDEX Upgrade," *Nuclear Fusion*, vol. 55, no. 8, p. 083004, 2015.

[94] Manz, P and Silvagni, D and Grover, O and Happel, T and Eich, T and Griener, M and ASDEX Upgrade Team and others, "Gyrofluid simulation of an I-mode pedestal relaxation event," *Physics of Plasmas*, vol. 28, no. 10, 2021.

[95] H. Doerk, F. Jenko, T. Görler, D. Told, M. Pueschel, and D. Hatch, "Gyrokinetic prediction of microtearing turbulence in standard tokamaks," *Physics of Plasmas*, vol. 19, no. 5, 2012.

[96] D. Hatch, M. Kotschenreuther, S. Mahajan, M. Pueschel, C. Michoski, G. Merlo, E. Hassan, A. Field, L. Frassinetti, C. Giroud, *et al.*, "Microtearing modes as the source of magnetic fluctuations in the JET pedestal," *Nuclear Fusion*, vol. 61, no. 3, p. 036015, 2021.

[97] R. D. Hazeltine, D. Dobrott, and T. S. Wang, "Kinetic theory of tearing instability," *The Physics of Fluids*, vol. 18, pp. 1778–1786, 12 1975.

[98] M. Kotschenreuther, X. Liu, D. Hatch, S. Mahajan, L. Zheng, A. Diallo, R. Groebner, J. Hillesheim, C. Maggi, C. Giroud, *et al.*, "Gyrokinetic analysis and simulation of pedestals to identify the culprits for energy losses using 'fingerprints'," *Nuclear Fusion*, vol. 59, no. 9, p. 096001, 2019.

[99] D. Hatch, M. Kotschenreuther, S. Mahajan, P. Valanju, F. Jenko, D. Told, T. Görler, and S. Saarelma, "Microtearing turbulence limiting the JET-ILW pedestal," *Nuclear Fusion*, vol. 56, no. 10, p. 104003, 2016.

[100] C. Pitzal, A. Stegmeir, W. Zholobenko, K. Zhang, and F. Jenko, "Landau-fluid simulations of edge-SOL turbulence with GRILLIX," *Physics of Plasmas*, vol. 30, no. 12, 2023.

[101] D. Michels, A. Stegmeir, P. Ulbl, D. Jarema, and F. Jenko, "GENE-X: A full-f gyrokinetic turbulence code based on the flux-coordinate independent approach," *Comput. Phys. Commun.*, vol. 264, p. 107986, 2021.

[102] V. Rozhansky, E. Kaveeva, P. Molchanov, I. Veselova, S. Voskoboynikov, D. Coster, G. Counsell, A. Kirk, S. Lisgo, and and, "New B2SOLPS5.2 transport code for H-mode regimes in tokamaks," *Nucl. Fusion*, vol. 49, no. 2, p. 025007, 2009.

[103] S. Hirshman and D. Sigmar, "Neoclassical transport of impurities in tokamak plasmas," *Nucl. Fusion*, vol. 21, no. 9, pp. 1079–1201, 1981.

[104] M. Newville, T. Stensitzki, D. B. Allen, M. Rawlik, A. Ingargiola, and A. Nelson, "Lmfit: Non-linear least-square minimization and curve-fitting for python," *Astrophysics Source Code Library*, pp. ascl–1606, 2016.